České vysoké učení technické v Praze
Fakulta jaderná a fyzikálně inženýrská

Katedra fyziky
Obor: Experimentální jaderná a částicová fyzika

Půvabné mezony v jaderných srážkách

VÝZKUMNÝ ÚKOL

Vypracoval: Bc. Robert Líčeník
Vedoucí práce: Mgr. Jaroslav Bielčík, Ph.D.
Konzultant: Ing. Lukáš Kramárik
Rok: 2018

Czech Technical University in Prague
Faculty of Nuclear Sciences and Physical Engineering

Department of Physics
Specialization : Experimental Nuclear and Particle Physics

Charmed mesons in heavy ion collisions

RESEARCH PROJECT

Author: Bc. Robert Líčeník
Supervisor: Mgr. Jaroslav Bielčík, Ph.D.
Consultant: Ing. Lukáš Kramárik
Year: 2018

Před svázáním místo téhle stránky $\boxed{\text{vložíte zadání práce}}$ s podpisem děkana (bude to jediný oboustranný list ve Vaší práci) !!!!

Prohlášení

Prohlašuji, že jsem svůj výzkumný úkol vypracoval samostatně a použil jsem pouze podklady (literaturu, projekty, SW atd.) uvedené v přiloženém seznamu.

Nemám závažný důvod proti použití tohoto školního díla ve smyslu § 60 Zákona č. 121/2000 Sb., o právech souvisejících s právem autorským a o změně některých zákonů (autorský zákon).

V Praze dne ....

....
Bc. Robert Líčeník

Acknowledgments

I would like to thank the supervisor of my thesis, Dr. Jaroslav Bielčík, for his guidance throughout the course of this work. I would also like to thank Lukáš Kramárik, Jakub Kvapil and Miroslav Šimko for their time, valuable consultations and advices which made the completion of this thesis possible.

Bc. Robert Líčeník

Název práce:
Půvabné mezony v jaderných srážkách

Autor: Bc. Robert Líčeník

Obor: Experimentální jaderná a částicová fyzika

Druh práce: Výzkumný úkol

Vedoucí práce: Mgr. Jaroslav Bielčík, Ph.D.
Katedra fyziky,
Fakulta jaderná a fyzikálně inženýrská,
České vysoké učení technické v Praze

Konzultant: Ing. Lukáš Kramárik
Katedra fyziky,
Fakulta jaderná a fyzikálně inženýrská,
České vysoké učení technické v Praze

Abstrakt: Hlavním cílem této práce je studium produkce půvabných mezonů. Půvabné mezony slouží jako vynikající sonda v silně interagujícím prostředí, jenž vzniká během srážek těžkých iontů. Toto prostředí, jež je velmi zajímavé kvůli své souvislosti s rannými stadii našeho vesmíru, se nazývá kvark-gluonové plazma. Půvabné mezony, jako například $D^{\pm}$, jsou vytvářeny během fáze tvrdého rozptylu po srážce, a tudíž projdou celým vývojem systému. Zveřejnění nových výsledků potvrzujích závěry předchozích měření, například potlačení produkce půvabných mezonů v centrálních jádro-jaderných srážkách, bylo umožněno použitím nově instalovaného detektoru HFT v rámci experimentu STAR. Tento detektor umožňuje dosud nevídanou přesnost při rekonstrukci sekundárních vertexů, které vznikly rozpadem půvabných mezonů na dceřinné částice. Přesná rekonstrukce sekundárních vertexů dovoluje zvýšit efektivitu měření výtěžku půvabných mezonů ve srážkách těžkých iontů.

Klíčová slova: půvabné mezony, srážky těžkých iontů, kvark-gluonové plazma, experiment STAR

Title:
Charmed mesons in heavy ion collisions

Author: Bc. Robert Líčeník

Specialization: Experimental Nuclear and Particle Physics

Sort of Thesis: Research Project

Supervisor: Mgr. Jaroslav Bielčík, Ph.D.
Department of Physics,
Faculty of Nuclear Sciences and Physical Engineering,
Czech Technical University in Prague

Consultant: Ing. Lukáš Kramárik
Katedra fyziky,
Fakulta jaderná a fyzikálně inženýrská,
České vysoké učení technické v Praze

Abstract: The main objective of this thesis is to study the charmed meson production. Charmed mesons serve as an excellent probe in the strongly interacting medium created during heavy ion collisions. This medium is called the quark-gluon plasma and it is an object of great interest due to its connection to the early stages of the Universe. The charmed mesons, such as the $D^{\pm}$*, are created during the hard scattering part of the collision and therefore experience the entire evolution of the system. The presentation of new results which confirm the conclusions of earlier measurements, for example the suppression of charmed mesons production in central nucleus-nucleus collisions, were made possible using the newly installed Heavy Flavor Tracker at the STAR experiment. This detector enables unprecedented accuracy in the reconstruction of secondary vertices, that occur as a result of charmed meson decay into daughter particles. Precise reconstruction of secondary vertices allows for higher efficiency of the charmed meson yield measurements in heavy ion collisions.*

Key words: charmed mesons, heavy ion collisions, quark-gluon plasma, STAR experiment

Contents

List of Figures

Introduction

At the very beginning of the Universe, about one microsecond after the Big Bang, the Universe was extremely hot, dense and rapidly expanding. It could be described as a "soup" of free quarks and gluons - the quark-gluon plasma (QGP). The Universe is, however, much cooler today and therefore, if we want to simulate these extreme conditions, we have to find a way to fill a tiny space with large energy and thus to achieve similar energy density. For this purpose, heavy atomic nuclei are accelerated to large kinetic energies (100 GeV per nucleon at RHIC and 2.51 TeV per nucleon at LHC) and then collided in heavy ion collision. There are hundreds of particles and antiparticles created during each collision. Often we are interested in particular rare physical processes. However, in general we would like to measure as many particles as possible. In order to detect them, we use complex particle detectors, such as the STAR experiment which has a great ability to distinguish between different types of particles and to trace them back to the point of their origin. One type of the most interesting particles are charmed mesons. Charmed mesons, created during the first moments after ultrarelativistic heavy ion collisions, serve as a probe of such exotic states of matter as the QGP. Because they are formed during the hard part of the collision (before the QGP forms), they experience the entire evolution of the system and provide us with valuable information about the QGP. There are many charmed mesons, but the most frequent are the neutral D^0, the charged $D^{\pm}$ and the strange $D_s^{\pm}$. The production of $D^{\pm}$ is the main subject of this work. It is the second lightest particle containing the c quark and therefore can decay only via the weak interaction which results in a relatively high mean lifetime ($\tau \simeq 1.040 \cdot 10^{-12}$ s) with corresponding mean decay length $\lambda = c\tau = 311.8$ μm. The most interesting decay channel is the $D^{\pm} \rightarrow K^{\mp}\pi^{\pm}\pi^{\pm}$. With a branching ratio of (8.98±0.28) % (values taken from PDG [1]), it is the most probable hadronic decay and therefore provides the best statistics. The first chapter of this work contains a brief theoretical introduction to the physics of heavy ion collisions. The second chapter provides an overview of recent results in the charmed mesons research, achieved by the Large Hadron Collider (LHC) in the European Organization for Nuclear Research (CERN) complex near Geneva and the Relativistic Heavy Ion Collider (RHIC) located near Upton, NY in the Brookhaven National Laboratory (BNL). The following chapter focuses on the RHIC accelerator complex and the STAR (Solenoidal Tracker At RHIC) experiment and its subdetectors. The main practical objective of this work is the reconstruction of the $D^{\pm}$ meson in Au-Au collisions at center-of-mass energy $\sqrt{s_{NN}} = 200$ GeV in a dataset collected by the STAR experiment during the year 2014. This run was significant because it was the first run which used the Heavy Flavor Tracker (HFT), a silicon detector that can achieve much higher spatial resolution than ever before, designed specifically for the detection of charmed mesons. This analysis follows the work started by Jakub Kvapil [2], [3] and the main motivation is to improve the signal significance, to complete the study of systematic errors and to publish the results. The current state of the analysis is described in chapter 4.

Chapter 1

Physics of Heavy Ion Collisions

Heavy ion collisions are interactions between two heavy atomic nuclei accelerated to high velocities, close to the speed of light in vacuum ($c = 299792458$ ms^{-1}). Collided nuclei are chosen based on their properties such as their shape, nucleon density and the number of nucleons. Currently collided are gold nuclei at RHIC and lead nuclei at the LHC. Uranium and copper nuclei were also collided recently at RHIC. To describe the physics of a heavy ion collision, several variables are introduced (sec. 1.1). Every heavy ion collision is characterized by its centrality (sec. 1.2). Centrality is responsible for initial conditions and therefore for the evolution of the system (sec. 1.3), the formation of the QGP (sec. 1.4) and the significance of the difference between an A-A and a p-p collision is affected. The ultimate objectives of the heavy-ion collision studies are to learn about the conditions during the early Universe and to obtain a QCD matter phase diagram (sec. 1.5).

1.1 Variables in Heavy Ion Collisions

1.1.1 Coordinates

Because of the geometry of the detector, which is usually cylindrical, the common practice is to use cylindrical coordinates to describe position during HIC. The z axis is running through the middle of the beam pipe and the origin $z = 0$ is placed at the interaction point which is the spot, where the nuclei collide. The x and y axes can be chosen arbitrarily as long as they are both perpendicular to the z axis and to each other, therefore defining a plane perpendicular to the z axis (for example, x can be horizontal and y vertical with respect to the ground). This is allowed because all physical phenomena are expected to be uniform in the azimuthal angle ϕ. Therefore most vector variables are projected into the z axis (referred to as longitudinal projection) and the plane perpendicular to this axis (transverse). For example, momentum $\vec{p}$ is usually handled as longitudinal momentum p_z and transverse momentum p_T. The polar angle, usually called θ, can be used to measure in which direction the products of the collision move away from the origin with respect to the z axis. However, rapidity y and pseudorapidity η are used more often since they feature some Lorentz-invariant properties.

1.1.2 Transverse Momentum

Transverse momentum p_T is a projection of the particle momentum into the perpendicular plane (to the z axis). It is defined by the relation

$$p_T = \sqrt{p_x^2 + p_y^2} \tag{1.1}$$

and is independent of the choice of the x and y axes (see subsec. 1.1.1). p_T is Lorentz-invariant during longitudinal boosts and therefore very useful in describing particles during HIC where products are traced back to their vertices.

1.1.3 Rapidity

Rapidity in HIC is defined by the relation

$$y = \frac{1}{2} \ln \frac{E + p_z}{E - p_z}. \tag{1.2}$$

During longitudinal boosts rapidity changes only by an additive constant. Since rapidity incorporates the p_z component, it can be used together with p_T to describe the particle momentum. The regions of detector with high $|y|$ are referred to as forward sector and the regions with low $|y|$ as mid-rapidity sector.

1.1.4 Pseudorapidity

Pseudorapidity η is often used instead of the polar angle θ because - same as with rapidity - the differences in pseudorapidity are Lorentz-invariant during longitudinal boosts. It is defined in the following equation:

$$\eta = -\ln \tan \frac{\theta}{2} \tag{1.3}$$

and in the ultrarelativistic limit ($m \to 0$) converges to rapidity. Pseudorapidity is used more often than rapidity since the only unknown that needs to be measured is the polar angle.

1.2 Collision Centrality

During heavy ion collisions the nuclei rarely collide "head-on". Instead, they overlap by a generally random portion. Nucleons, that are in the overlapping region are referred to as participants, the remaining are called spectators and do not participate in the collision. The overlapping part of the two nuclei can be characterized by an impact

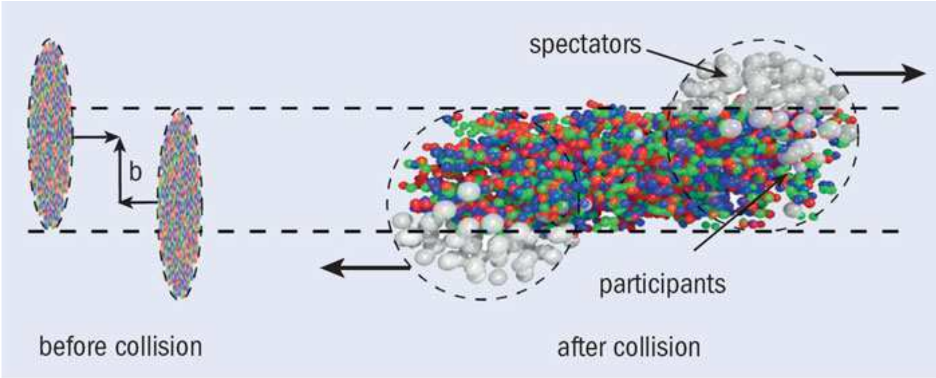

Figure 1.1: Illustration of a nucleus-nucleus collision. Participants, spectators and the impact parameter b is shown. Taken from Ref. [4].

parameter b. The impact parameter is defined as the minimum distance between the centers of both nuclei (Fig. 1.1).

Depending on b, the collision can be classified as either central ($b \simeq 0$), peripheral ($R_A + R_B > b > 0$), where R_A and R_B are the radii of the two nuclei, and ultra-peripheral ($b > R_A + R_B$). The impact parameter cannot be measured directly, but one way to estimate b is to introduce multiplicity. Multiplicity is the amount of tracks created during the event. More central collisions should create more tracks in the Time Projection Chamber (TPC). Then for example the 10 % of the events with the highest multiplicity are defined as events within centrality range $0 - 10\%$. An example of an ALICE multiplicity measurement can be seen in Fig. 1.2.

One of the theoretical models describing the collision centrality and the relation to the impact parameter is the Glauber model [6]. However, its details are not discussed this work.

1.3 Collision Evolution

During the HIC it can be assumed, that the nucleons participating in the collision collide "one-on-one" - binary collisions. The participants scatter and a system of hot dense matter - called fireball - is formed. Provided the energy density is high enough, new particle - antiparticle pairs are being created from the vacuum. This period is called the hard scattering and the system is not in a thermal equilibrium. This is the stage during which all the c and b quarks are created - their number is conserved throughout the entire process. If the temperature of the system rises above a certain threshold, called the critical temperature T_c, the deconfinement sets in. The quarks and gluons cease to be bounded inside hadrons and the medium is called the Quark Gluon Plasma (QGP). When a thermal equilibrium is reached, the system is following hydrodynamic laws similarly to a superfluid that cools down and expands in time and space. After the temperature has decreased below T_c, the system enters a new phase - the hadronization. The system further cools down and expands during this stage, but the quarks cannot be free anymore and are confined in baryons and mesons,

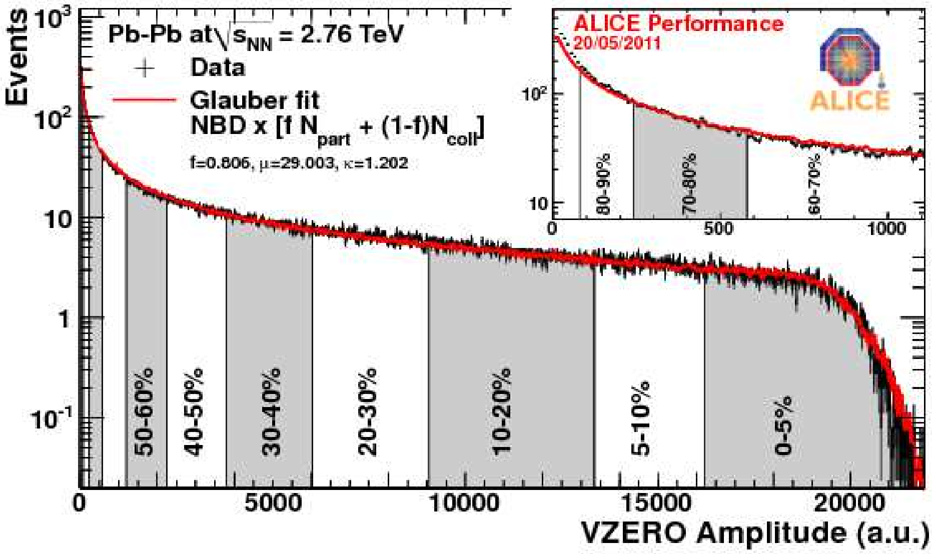

Figure 1.2: ALICE 2.76 TeV measurements of multiplicity in Pb-Pb collisions. Particle count is plotted against the ALICE V0 detector signal strength, proportional to deposited energy. Data are fitted by a Glauber model calculation. Taken from Ref. [5].

held together by gluon fields. The hadronization period can be further divided into two stages. During the first stage, new particles can still be created, but when the temperature decreases below a certain threshold, a chemical freeze-out occurs. During the second stage, remaining hadrons still elastically collide among themselves, as the temperature decreases further, until the interactions stop entirely. The point in space-time where the hadrons do not interact anymore is called the kinetic freeze-out. The final products (leptons, pions, kaons, protons and photons) are then captured in the detector. This entire evolution is illustrated in Fig. 1.3.

The space-time evolution of a high-energy heavy-ion collision is illustrated in Fig. 1.4

1.4 Quark-gluon Plasma

Quark-gluon plasma (QGP) is a recently discovered (2004, at RHIC [9], [10], [11], [12], [13]) state of matter, where quarks and gluons are free, unlike hadronic matter (and antimatter) where they are confined inside hadrons by the strong force. The QGP is an interesting medium to study, since the early Universe is thought to be in this state between the end of the inflation period and hadronization, $t \sim 10^{-6}$ s. As far as we know, the QGP is not observable anywhere in the present Universe, except for brief time periods after nucleus-nucleus (A-A) collisions in particle accelerators and perhaps in the very centers of neutron stars. The QGP is known to be extremely hot, dense and moving with low viscosity, therefore its behavior can be compared to the behavior of ideal fluids.

The physics of the QGP is governed by the strong interaction between color charged

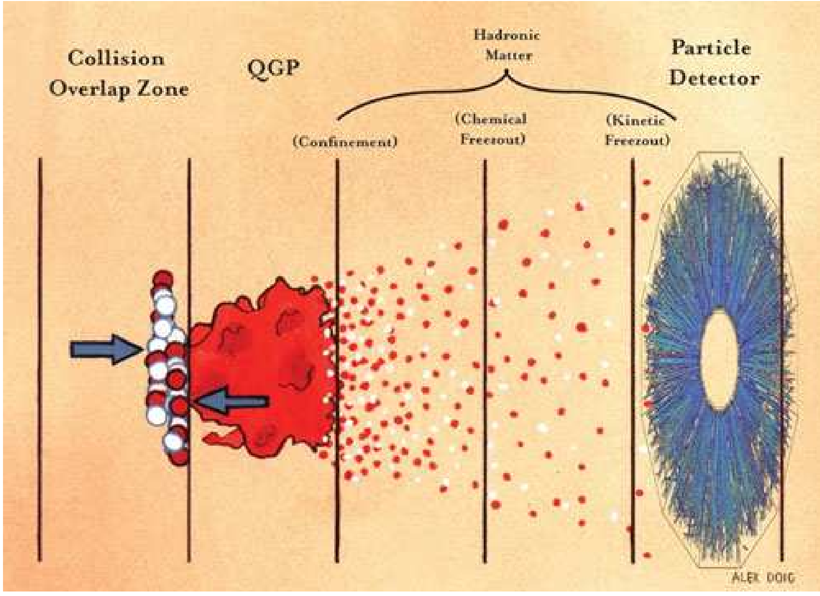

Figure 1.3: An image showing the time evolution of the stages in a heavy ion collision. The hadronization period is further divided into two smaller time intervals, before and after chemical freeze-out. Taken from Ref. [7].

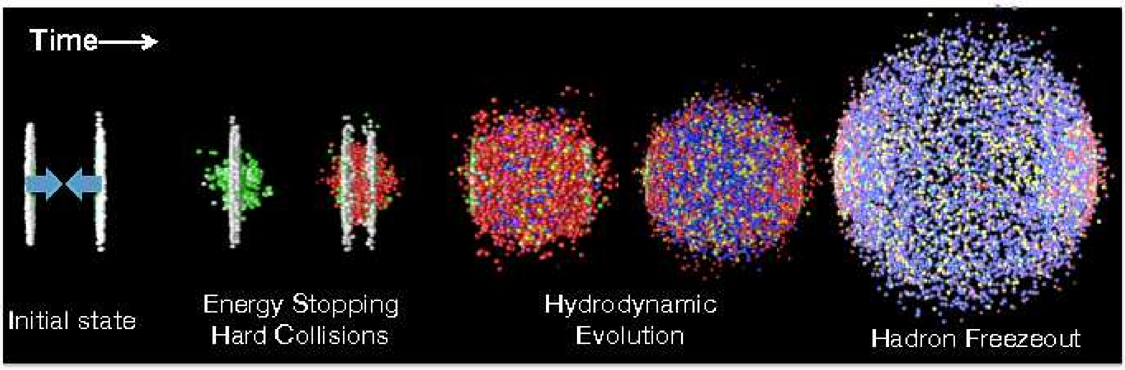

Figure 1.4: Time-space high-energy heavy-ion collision evolution illustration. QGP is present in the third stage. Taken from Ref. [8].

partons (quarks and gluons). The widely spread theoretical model describing strong interaction is the quantum chromodynamics (QCD). Color charge is a quantum number similar to the electric charge, but unlike it, there are 6 possible color states (red, green, blue and corresponding anticolors antired, antigreen and antiblue), instead of just 2 electric charges (+, -). Quarks carry one color, while gluons carry a combination of one color and one anticolor and bind quarks together to form hadrons. This is a major difference from the electromagnetic force, because the EM force gauge bosons (photons) are not charged and cannot interact with each other, while gluons often do interact among themselves. As the law of conservation of color charge states, all hadrons must be color-neutral/colorless. This means that baryons have to be composed of 3 quarks, one of each color (antibaryons are composed of 3 antiquarks, one of each anticolor), while mesons are composed of a colored quark and an antiquark of the corresponding anticolor. The characteristic time of the strong interaction is $\tau \sim 10^{-23}$ s. The strong force is parametrized by a strong interaction coupling constant,

$$\alpha_s(Q) = \frac{12\pi}{(33 - 2N_f)\ln \frac{Q^2}{\lambda_{QCD}}}, \tag{1.4}$$

where N_f is the number of quark flavors, Q^2 is the four momentum transfer and $\lambda_{QCD} \simeq 0.2$ GeV is the typical QCD scale, obtained experimentally [14]. The main characteristic of the strong interaction coupling constant is that it does depend on the energy of the system, its temperature and distance over which the interaction acts. The dependence on momentum (therefore on energy and temperature as well) can be seen in Fig. 1.5.

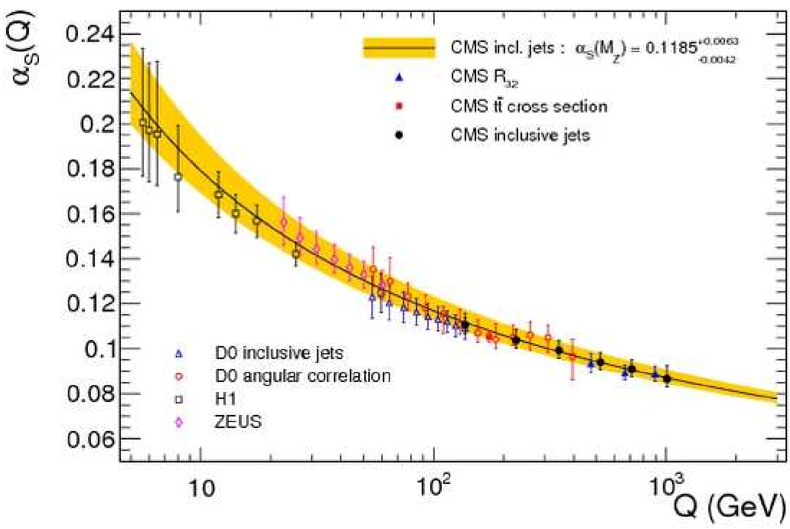

Figure 1.5: CMS measurement of the strong interaction coupling constant α_s dependence on momentum. Data compared to QCD calculation and other experiments (D0, H1 and Zeus). $\alpha_s(M_Z)$ is the value at Z^0 mass, world average. Taken from Ref. [15].

This property of the strong coupling constant has an interesting implication. When the system has a sufficient energy, the strong interaction cannot hold the quarks and gluons together and allows them to move freely. This system of free quarks and gluons is then called the QGP. The parameter characterizing this sufficient energy is the critical temperature ($T_c = 140 - 200$ MeV, depending on calculation, [16, 17, 18]). Two phenomena, called confinement and asymptotic freedom, arise from the dependence of the coupling constant on separation between the two partons. The relation is inversely proportional, meaning that when the two partons move apart, α_s increases to the point, where it is more energetically favorable to create a new quark-antiquark pair from vacuum rather than to continue the separation. This can be illustrated by an example with a string. Suppose we have a string and pull the ends apart, at some point, the string will snap, creating two shorter strings and reducing the tension. On the other hand, at short distances ($r < r_c \sim 0.5$ fm), the partons are allowed to move freely (the string is very loose).

When a parton interacts with the QGP, it will lose energy via mechanism known as the parton energy loss (see 1.4.1), this has direct effect on the yield of particles that we observe in A-A collisions. The modification of the yield is parametrized by a variable called a nuclear modification factor, which is introduced in subsection 1.4.2. Since it is impossible to observe and study the QGP directly because of its very short lifetime and rather extreme nature. The only way to obtain desired variables of the QGP, such as its temperature, density and viscosity, is using probes. Hard probes - such as charmed quarks - are created before the QGP and therefore experience the entire evolution of the system, while the number of these quarks is conserved. Some other hard processes frequently used as probes are jet quenching and quarkonium production suppression, which are discussed briefly in subsections 1.4.3 and 1.4.4. Soft probes, such as the flow of the system (subsection 1.4.5), do not rely on highly energetic particles, but rather utilize the collective behavior of the system after the QGP has formed.

1.4.1 Parton Energy Loss

When a parton moves through a strongly-interacting medium such as the QGP, it will interact with the free color charges in the medium and will lose energy. Similar situation occurs in everyday situations, for example: electron traveling through a material will interact with the atoms via the electromagnetic force and lose energy. The more energetic the electron is, the further it will travel through the material until it stops. The EM energy losses for heavy particles follow the well-known Bethe-Bloch formula:

$$-\left\langle \frac{\mathrm{d}E}{\mathrm{d}x} \right\rangle = 4\pi N_A r_e^2 m_e c^2 \frac{Z}{A}\frac{1}{\beta^2}\left[\frac{1}{2}\ln\frac{2m_e c^2\beta^2\gamma^2 T_{max}}{I^2} - \beta^2 - \frac{\delta(\beta\gamma)}{2}\right], \tag{1.5}$$

where N_A is the Avogadro number, r_e and m_e are the electron classical radius and mass respectively, Z and A are proton and atomic numbers of the material, $\beta = \frac{v}{c}$, $\gamma = \frac{1}{\sqrt{1-\beta^2}}$, T_{max} is the maximum energy transfer of one interaction, I is the mean excitation energy and $\delta(\beta\gamma)$ is the density correction term. An example of the formula for muon passing through copper can be seen plotted in Fig. 1.6.

The difference between energy losses in a bulk of copper and the QGP is that the QGP is much denser and that even the mediators of the strong interaction - gluons - are charged and therefore the energy loss is much more intense to the point that even ultrarelativistic particles will not travel very far. There are two principal means of energy loss - elastic collisions and radiative losses. Collisions dominate at low energies while radiation (of gluons) dominates at high energies. For the energy loss of a heavy quark (with a mass M and energy E) via elastic collisions while traversing a distance l in medium of temperature T, the following formula

$$-\frac{\mathrm{d}E}{\mathrm{d}l} = \frac{1}{4}C_R\alpha_s(ET)m_D^2\ln\left(\frac{ET}{m_D^2}\right) - \frac{2}{9}C_R\pi T^2[\alpha_s(M^2)\alpha_s(ET)\ln\left(\frac{ET}{M^2}\right)], \tag{1.6}$$

where $C_R = 4/3$ is the color charge of the quark and $m_D^2 \simeq 4\pi\alpha_s T^2(1 + N_f/6)$ is the Debye mass squared, holds [19]. The radiative losses are achieved via "gluonstrahlung"

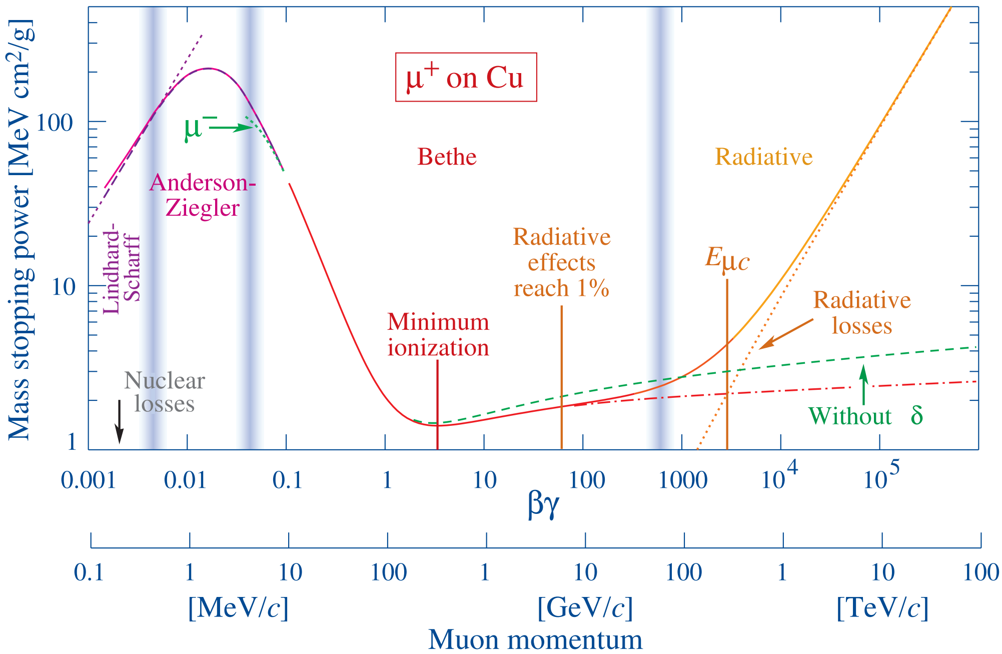

Figure 1.6: The mean energy loss dependence on momentum for muon passing through copper. For lower energies, the behavior is described by the Bethe-Bloch formula (eq. 1.5, while at higher energies the radiation dominates. Taken from Ref. [1].

- the emission of gluons. They can be calculated in two limiting cases, based on the thickness L of the medium compared to the radiation length λ. For the thin medium case ($L << \lambda$), the energy loss can be calculated via eq. 1.7.

$$\Delta E_{rad} \approx \alpha_s C_R \hat{q} L^2 \ln(\frac{E}{m_D^2 L}), \tag{1.7}$$

where $\hat{q}$ is the transport coefficient of the medium. In the thick medium case ($L >> \lambda$) we have to further differentiate between the soft and hard gluon emissions. These cases are based on the characteristic gluon energy $\omega_c = \frac{1}{2}\hat{q}L^2$. The equations for the energy loss are then:

$$\Delta E_{rad} \approx \alpha_s C_R \begin{cases} \hat{q}L^2, & \omega < \omega_c \\ \hat{q}L^2 \ln(E/(\hat{q}L^2)), & \omega > \omega_c. \end{cases} \tag{1.8}$$

More details about the ways partons lose energy in strongly interacting medium can be found in Ref. [19] and [20].

1.4.2 Nuclear Modification Factor

Because of the parton energy loss mechanisms described in 1.4.1 and because of the Cold Nuclear Matter (CNM) effects, such as shadowing or anti-shadowing, the Cronin effect, nuclear absorption and others, the charmed meson yield from A-A collisions will be different than the yield from p-p collisions, even though A-A collisions can be treated as separate binary collisions. To measure the effect that the medium has on the production, it is common to introduce a variable called the nuclear modification factor R_{AA}. It is the ratio of the measured A-A yield and the measured p-p yield multiplied by the mean number of binary collisions:

$$R_{AA} = \frac{\frac{\mathrm{d}^2 N_{AA}}{\mathrm{d}p_T \mathrm{d}y}}{\langle N_{coll} \rangle \times \frac{\mathrm{d}^2 N_{pp}}{\mathrm{d}p_T \mathrm{d}y}} \tag{1.9}$$

This factor then includes all effects of the nuclear matter. Additional measurements are required to separate effects caused by the QGP from the CNM effects. To determine these effects, caused by the presence of a nucleus, results from p/d-A collisions (characterized by a factor R_{pA}/R_{dA}, defined similarly as R_{AA}, 1.9) are studied. In these systems, the above-mentioned effects are present, but - as far as it is known - there is no significant QGP created.

The effect a strongly interacting medium has on the particles can be seen in Fig. 1.7. At high p_T all particles are suppressed with the exception of direct photons (orange, they are unaffected by the medium, because they carry no color charge). The protons (purple) appear enhanced at $p_T \simeq 2$ GeV/c as a result of the Cronin effect [21] and the baryon anomaly [22]. The electrons in question (grey) come from heavy flavor (b, c) decays and are suppressed as a result of HF suppression, while directly produced electrons would be unaffected by the medium the same way as the direct photons.

Results from charmed meson production measurements - which usually include the measurement of R_{AA} - are summarized in chapter 2.

1.4.3 Jet Quenching

A jet is defined as a narrow collimated bunch of particles with large transverse momentum. It is the final product of fragmentation and hadronization of a hard parton. When this hard parton moves, it radiates gluons which can create new particles and these products then move in the general direction of the original parton. Jets are usually present in high energy events and are observed as back to back dijets. The most interesting dijets are those, which form on the edge of the fireball. One of these jets will go straight to the vacuum while the other jet will traverse the medium created after the collision. This jet will then lose energy in the QGP (via mechanisms described in the previous subsection) and will be "quenched" - no jet will be detected, while the jet that traveled through vacuum only will be clearly visible. Observations of single jets, with no observed jet on the other side are now interpreted as a proof of a QGP formation. This situation can be seen in Fig. 1.8, where a peak at 0 deg is an indication that a dijet has formed, while the peak at 180 deg is observable only in p-p and d-Au collisions. The difference between the height of the peaks at 180 deg is due to Cold Nuclear Matter (CNM) effects. It is important to note that this phenomenon is only visible for high-p_T particles. The requirement for the trigger particle was $p_T > 4$ GeV/c and for the associated particle $p_T > 2$ GeV/c.

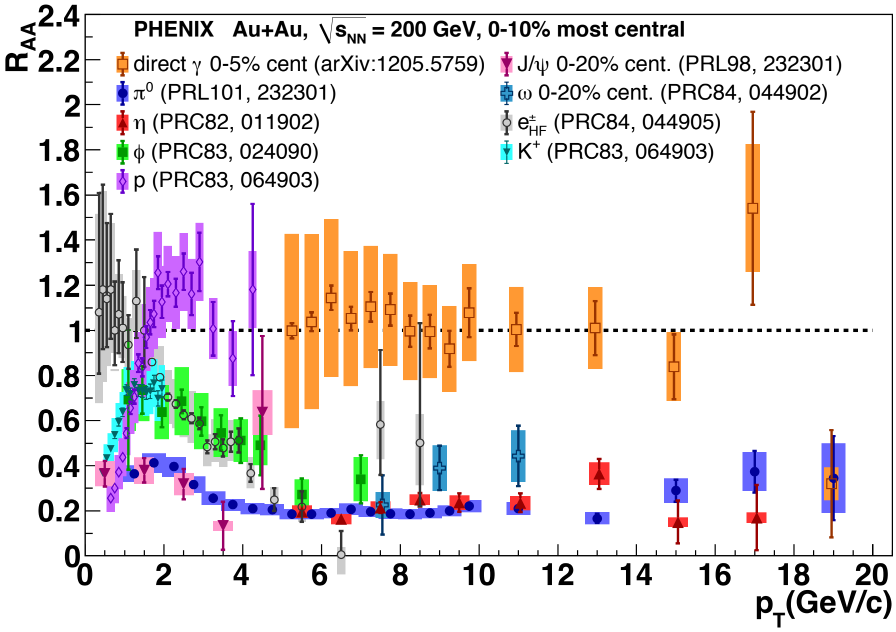

Figure 1.7: The PHENIX collaboration results of R_{AA} measurements for several identified particles in 0-10 % most central Au-Au collisions at $\sqrt{s_{nn}} = 200$ GeV. Taken from Ref. [20] + references in the figure.

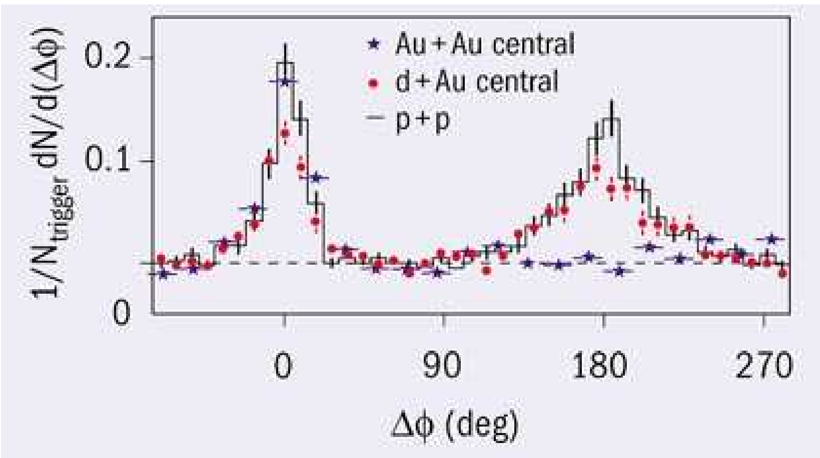

Figure 1.8: STAR measurement of hadron count distribution in azimuthal angle. The peak at 0 deg for high-p_T particles, indicating the formation of a dijet is observed in all types of collisions. The second peak (at 180 deg) is not observable in central Au-Au collisions, implying that the jet was quenched in the medium. In p-p and d-Au collisions, the second peak is clearly observable. Taken from Ref. [9].

Since jet quenching is not the main focus of this thesis, only this brief summary is included. For further details on jets and jet quenching see Ref. [19] or [23].

1.4.4 Quarkonia Production Suppression

The suppression observed in quarkonia production, first introduced by Matsui and Satz in 1986 [24], is a strong indication of QGP formation. Quarkonia (such as J/ψ or Υ) are bound states of heavy quark-antiquark pairs and therefore are created exclusively during the hard part of the collision, before the QGP has formed. The suppression of their production is caused by a phenomenon called the Debye screening. The presence of free color charges in the QGP causes the Debye radius - the distance over which the two quarks can still "feel" each others' presence - to decrease below the actual radius of the quarkonium, causing the quarkonium to dissolve. Quarkonium production shows high level of suppression in A-A collisions, as seen in Fig. 1.9. The J/ψ production in U-U collisions is consistent with the results from Au-Au collisions for all three energies.

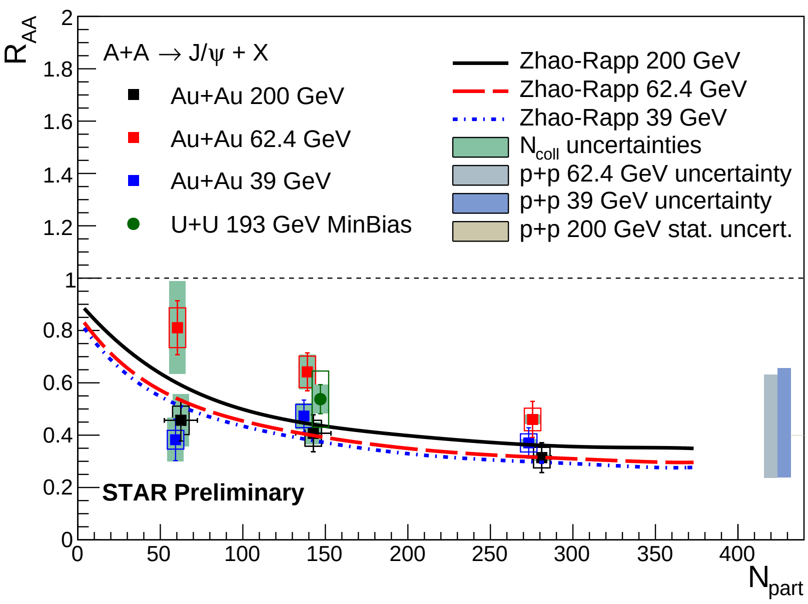

Figure 1.9: Preliminary STAR results illustrating the J/ψ production suppression in Au-Au ($\sqrt{s_{NN}}$ = 200, 62.4 and 39 GeV) collisions and U-U ($\sqrt{s_{NN}}$ = 193 GeV) collisions. Plotted is the nuclear modification factor R_{AA} against the number of participants N_{part} along with theoretical predictions. The suppression is due to the formation of the QGP. Taken from Ref. [25].

Because different quarkonia dissolve at different temperature, one can determine the approximate temperature of the system by studying which quarkonium states "survive" in the QGP. However, quarkonia production suppression is not a main focus of this work, so only this brief introduction is presented. For more details about quarkonia see Ref. [26] or [18].

1.4.5 Flow

Flow is a result of an initial anisotropy in the system. Because most of the heavy ion collisions are not head-on (see sec. 1.2), the participant distribution is not uniform. As a result, there is a pressure gradient, which in turn leads to a flow of the hot medium (which follows collective behavior), as illustrated in Fig. 1.10.

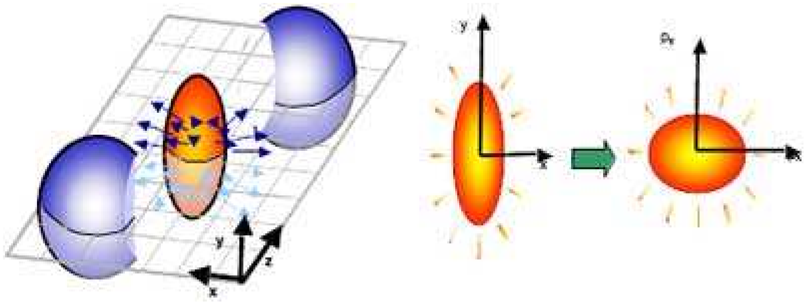

Figure 1.10: Left: The active collision zone between two nuclei. Right: The initial anisotropy (typical almond shape) of the collision zone and its evolution into the final-state elliptic flow. Taken from Ref. [27].

Flow is characterized by flow coefficients $v_n = \langle \cos[n(\phi - \Psi_{RP})] \rangle$, where Ψ_{RP} is the reaction plane angle, defined by the beam line and the line connecting the centers of both nuclei. These coefficients are present in the Fourier series expansion of the particle momentum distribution function (see Ref. [28] or [29] for details):

$$E\frac{\mathrm{d}^3N}{\mathrm{d}^3p} = \frac{1}{2\pi}\frac{\mathrm{d}^2N}{p_T\mathrm{d}p_T\mathrm{d}y}\left(1 + 2\sum_{n=1}^{\infty} v_n \cos[n(\phi - \Psi_{RP})]\right), \tag{1.10}$$

where E is the energy. The most important flow coefficients are the v_1, v_2 and v_3, describing direct, elliptic and triangular flow, although even higher harmonics were measured [29]. The v_2 is expected to be non-zero for a strongly coupled medium that follows collective behavior. This was experimentally confirmed by RHIC elliptic flow measurements and one such measurement (for D^0 mesons) is shown in Fig. 1.11), along with several theoretical models. None of these models is however able to predict the entire spectrum. Even after correcting for non-flow effects, there is still significant flow remaining, which implies that the medium is flowing with low viscosity and therefore can be treated as a near-perfect liquid.

The third flow coefficient v_3 represents triangular flow. This flow arises from event-by-event fluctuations of the nucleon distributions of the colliding nuclei. Because the nuclei cannot be treated as balls (or pancakes), the overlapping portions of the two nuclei do not always form an almond shape which gives rise to another type of anisotropy.

Although a significant observable in heavy-ion collisions, flow is not a main focus of this thesis. Therefore, only this brief introduction is shown.

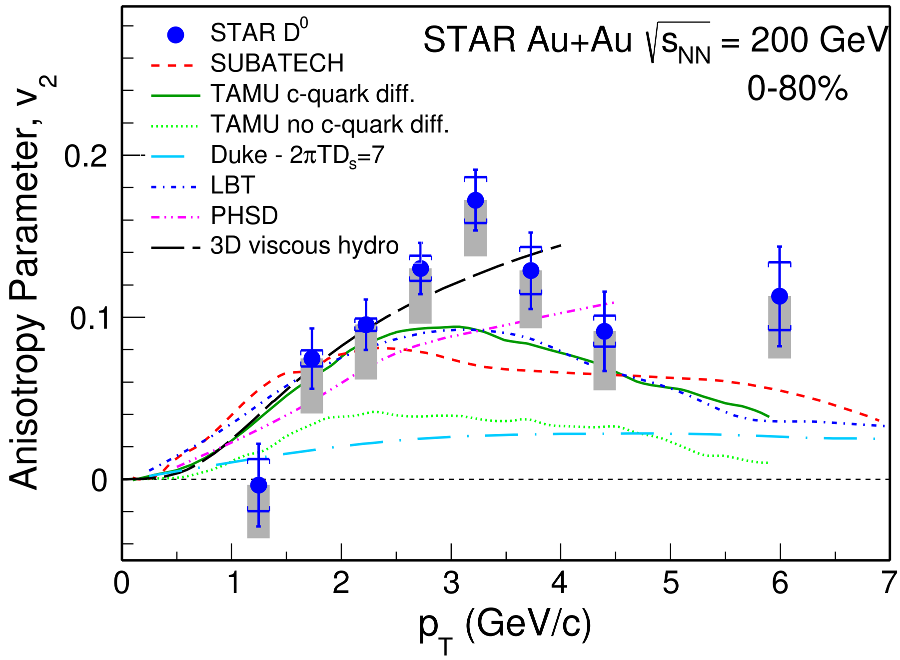

Figure 1.11: STAR results from D^0 v_2 flow coefficient dependence on p_T in Au-Au collisions at $\sqrt{s_{NN}} = 200$ GeV. The minimum-bias data are compared to several theoretical models. There is significant elliptic flow even after taking in account non-flow effects which indicates QGP formation. Taken from Ref. [30].

1.5 QCD Phase Diagram

The completion of phase diagram of the strongly interacting matter is one of the main objectives of today's experiments. It is known that QCD matter can exist in several phases. These phases are distinguished by the temperature T and the baryon chemical potential μ at which they occur. At "normal" conditions (low T and μ) the quarks and gluons are confined inside hadrons - phase known as the hadronic gas. At high temperature the system undergoes a phase transition and becomes the QGP. A neutron star - system observable in the present day Universe - has a near-zero temperature (on the MeV scale) and a large μ. At even higher values of μ the system is expected to undergo a phase transition into an exotic phase called a color superconductor. Another interesting feature of the phase diagram is the critical point. At this point, the phase transition should be of second order instead of the usual first order (before the critical point) and mixed order (beyond the CP) phase transition. Finding the location of the critical point in the QCD phase diagram and thus proving its existence is an ongoing task, although some significant progress has been made ([32], [33]). A major project aimed at improving our knowledge of the QCD phase diagram has been conducted at STAR (RHIC Beam Energy Scan - Phase I, see sec. 3.1, [34]) with the second part of this project set to be conducted in near future. The QCD phase diagram is illustrated in Fig. 1.12, including the critical point position, the phase transition lines and the BES-I.

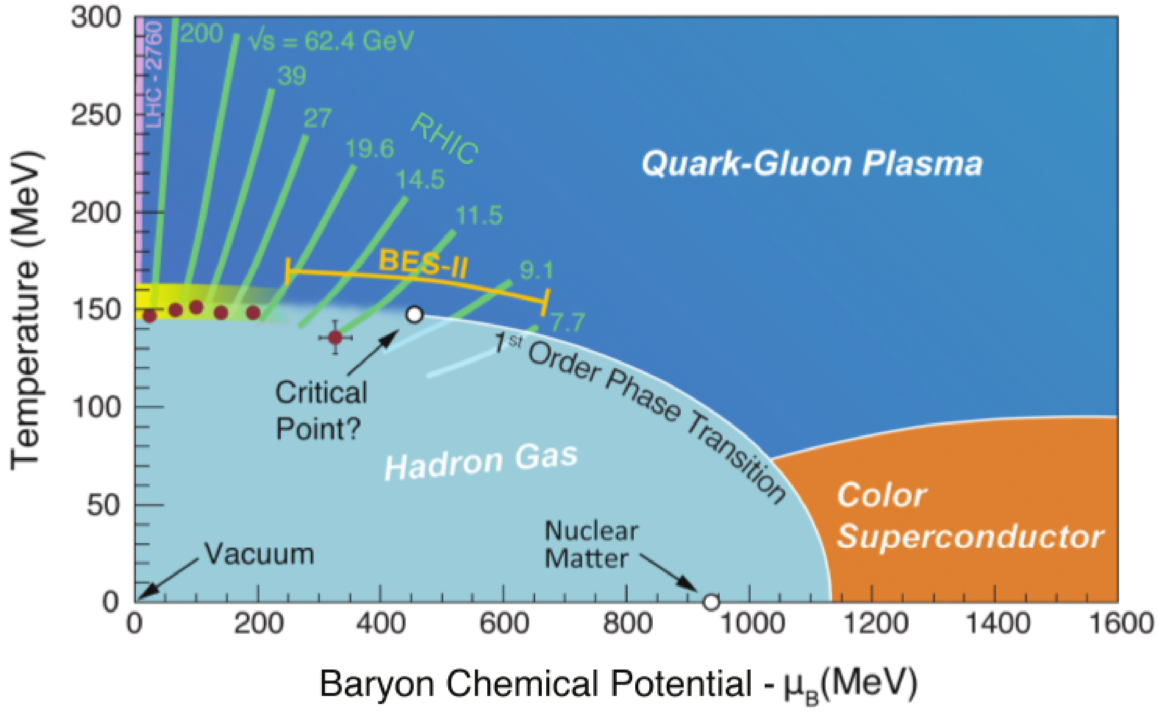

Figure 1.12: An illustration of the QCD phase diagram. The phase transition and freeze-out lines, as well as the critical point, different states of matter and position of the RHIC Beam Energy Scan measurements can be seen. Taken from Ref. [31].

Probes that are used to determine the thermodynamical variables (especially T) essential for the completion of the QCD phase diagram, were discussed in sec. 1.4.

Chapter 2

RHIC and LHC Results

The main motivation behind the $D^{\pm}$ measurements is to confirm the results obtained from the D^0 measurements that - at high p_T - there is a significant suppression in D meson production as a direct consequence of the QGP formation. The $D^{\pm}$ results in A-A collisions are usually compared to the results from p-p collisions (to see the difference between the two types of collision - this includes the QGP effects) and to previous D^0 results, since the behavior is expected to be the same for all types of D mesons. The $D^{\pm}$ meson production is currently measured by four experiments at two particle accelerators. The STAR experiment is located at the Relativistic Heavy Ion Collider (RHIC) in Brookhaven National Laboratory (BNL) in the USA and the ALICE, ATLAS and LHCb experiments are currently operating at the Large Hadron Collider (LHC) operated by the European Organization for Nuclear Research (CERN) under the Swiss/French border. The results from these experiments are summarized in this chapter. The $D^{\pm}$ is usually reconstructed from the three-body decay channel $D^{\pm} \rightarrow K^{\mp}+\pi^{\pm}+\pi^{\pm}$ as this is the hadronic channel with the highest branching ratio BR = 8.98 ± 0.28 % [1]. The value of the c quark fragmentation function, effectively the probability that the c quark will form a charged D meson, is $f(c \rightarrow D^{+}) = 0.246 \pm 0.020$ [1].

2.1 STAR

The installation of the HFT in the STAR detector allowed for precise reconstruction of the $D^{\pm}$ signal in $\sqrt{s_{NN}} = 200$ GeV Au-Au collisions, thanks to its unprecedented spatial resolution. The first preliminary results were presented by Jakub Kvapil at the 2017 Quark Matter [2] as a result of his analysis [3]. These results include the invariant yield measurement of $D^{\pm}$ in the 0-10 % centrality bin, as can be seen in Fig. 2.1 along with comparison to previous STAR D^0 results. The results (scaled by the c quark fragmentation ratio) show good agreement with each other. In figure 2.2 the nuclear modification factor R_{AuAu} dependence on p_T can be seen. Although there are no data points for low p_T, for higher p_T the points appear to be consistent with the STAR D^0 results and ALICE results (Fig. 2.6), showing increasing suppression towards higher p_T in the measured range.

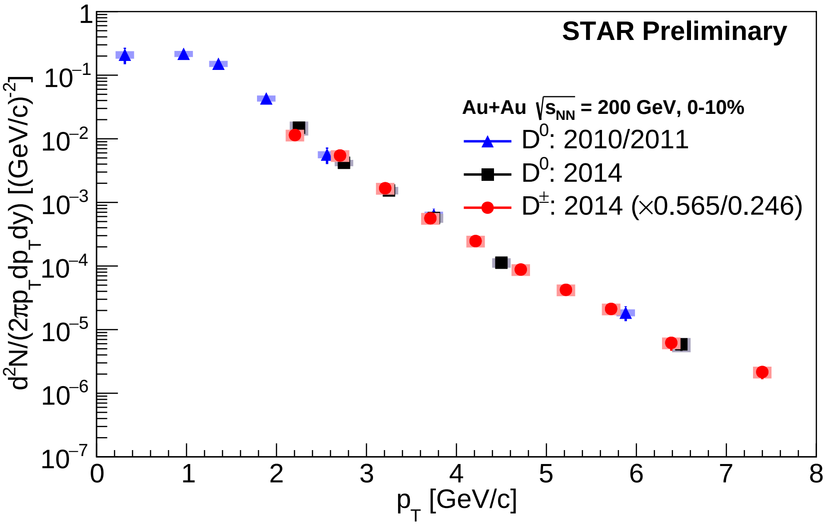

Figure 2.1: Preliminary results of the $D^\pm$ invariant yield in 2014 Au-Au collisions at $\sqrt{s_{NN}} = 200$ GeV for centralities 0-10 % (circles) along with the points from D^0 2010/2011 (triangles) and 2014 (squares) measurements from the STAR collaboration. Taken from Ref. [3].

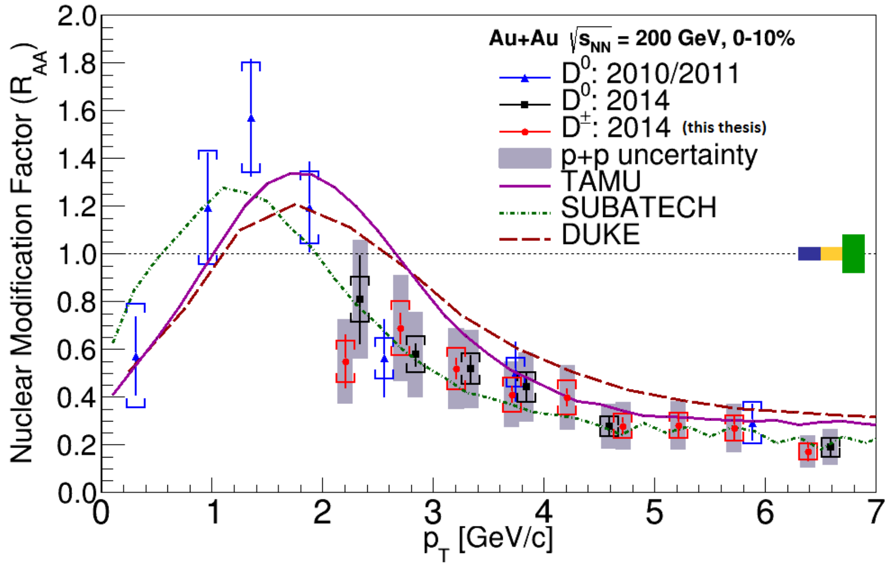

Figure 2.2: Preliminary results of $D^\pm$ R_{AuAu} in 2014 Au-Au collisions at $\sqrt{s_{NN}} = 200$ GeV for centralities 0-10 % along with the results from D^0 measurements conducted by the STAR collaboration and several theoretical models. Taken from Ref. [3].

2.2 ALICE

The ALICE collaboration published their results of D^+ cross-section from p-p collisions at $\sqrt{s} = 7$ TeV in the 2017 paper [35]. The cross-section dependence on transverse momentum for central rapidity in the $1 < p_T < 24$ GeV/c range can be seen in Fig. 2.3 and shows behavior consistent with the FONLL prediction and with the results of other LHC experiments - theory slightly underestimating the data.

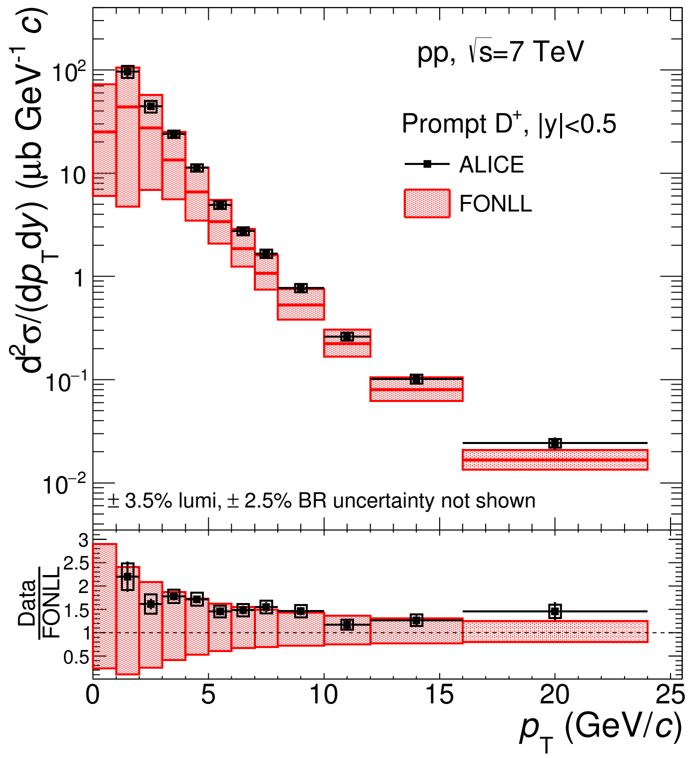

Figure 2.3: Results of prompt D^+ cross-section dependence on p_T in mid rapidity in p-p collisions at $\sqrt{s} = 7$ TeV as measured by the ALICE experiment. Data are compared to the FONLL prediction. Taken from Ref. [35].

The ALICE results from Pb-Pb collisions at $\sqrt{s_{NN}} = 2.76$ TeV published in 2015 [36] include the measurement of the D meson invariant yield dependence on p_T as seen in Fig. 2.4 for centralities 0-10 % and in Fig. 2.5 for centralities 30-50 %.

The ALICE results of R_{PbPb} as seen in Fig. 2.6 and Fig. 2.7 indicate strong D meson production suppression in both central (R_{PbPb} reaching as low as 0.2) and semi-peripheral (R_{PbPb} as low as 0.4) collisions at $\sqrt{s_{NN}} = 2.76$ TeV. Both minima occur at approximately $p_T = 10$ GeV/c.

2.3 ATLAS

The ATLAS collaboration published results of their measurement of the $D^\pm$ production cross-section in p-p collisions at $\sqrt{s} = 7$ TeV in 2016 [37]. The $D^\pm$ cross-section measurement as a function of transverse momentum in the $3.5 < p_T < 100$ GeV/c range in central rapidity is shown in Fig. 2.8. The results are consistent with theory and, similarly to ALICE and LHCb, the data points lie near the upper bounds of the predictions.

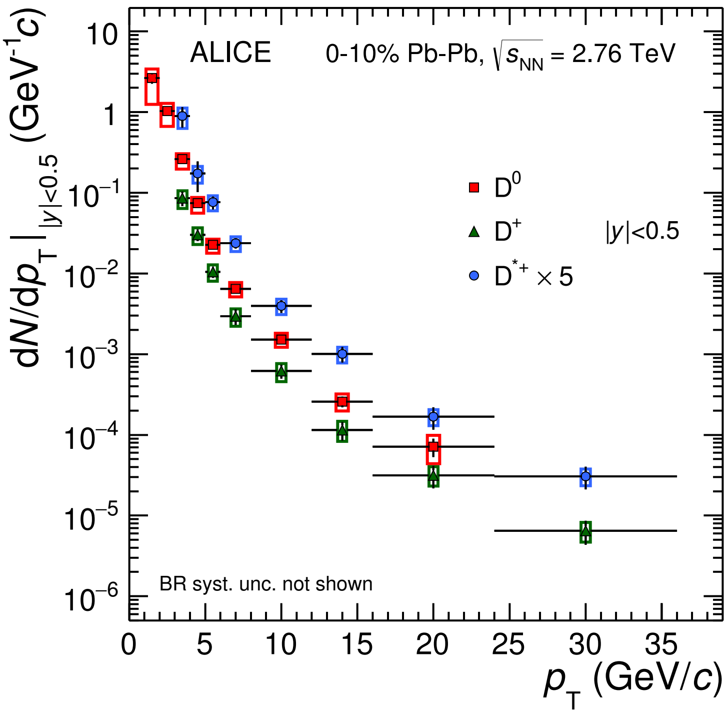

Figure 2.4: ALICE results of D meson (D^+ marked as triangles) invariant yield measurements in Pb-Pb collisions at $\sqrt{s_{NN}} = 2.76$ TeV for centrality bin 0-10 %. Taken from Ref. [36].

2.4 LHCb

The LHCb collaboration published their results of charm mesons production cross-sections in p-p collisions at $\sqrt{s} = 13$ TeV in 2015 [38]. The $D^{\pm}$ cross-section measurement as a function of transverse momentum in forward rapidity in the $0 < p_T < 14$ GeV/c range is shown in Fig. 2.9. The results are in agreement with theory, usually lying near the upper bound of the predictions as is the case with the ALICE and ATLAS results.

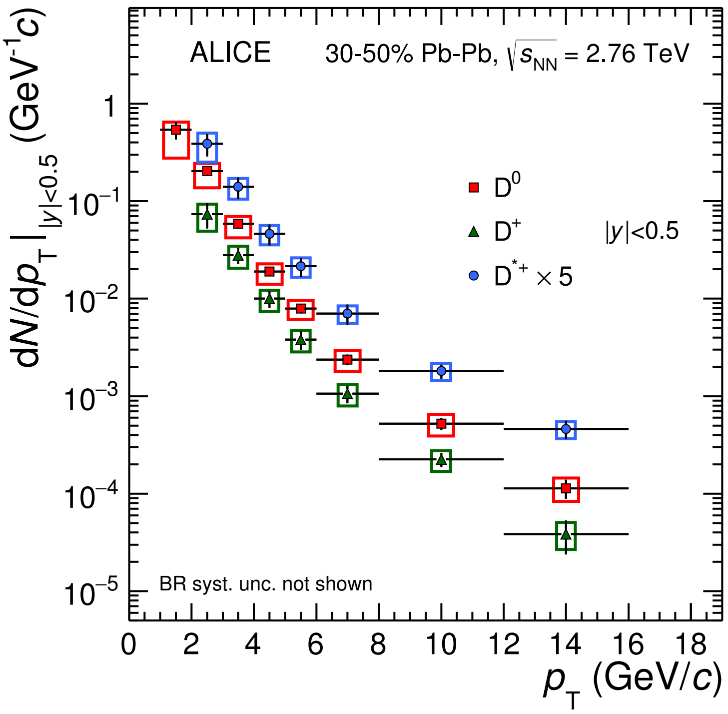

Figure 2.5: ALICE results of D meson (D^+ marked as triangles) invariant yield measurements in Pb-Pb collisions at $\sqrt{s_{NN}} = 2.76$ TeV for centrality bin 30-50 %. Taken from Ref. [36].

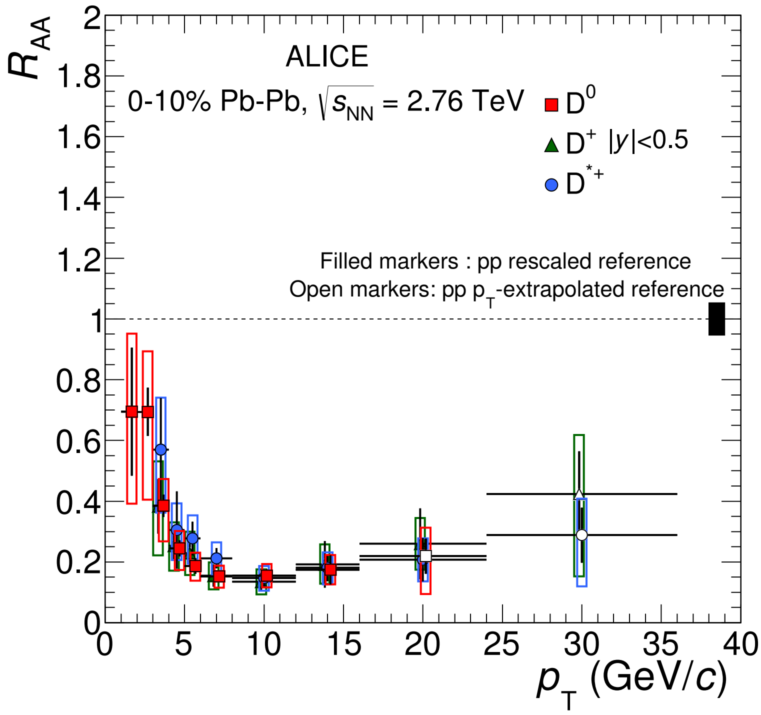

Figure 2.6: The ALICE experiment results of R_{PbPb} for centralities 0-10 % in 2.76 TeV collisions. D^+ are marked as triangles. Taken from Ref. [36].

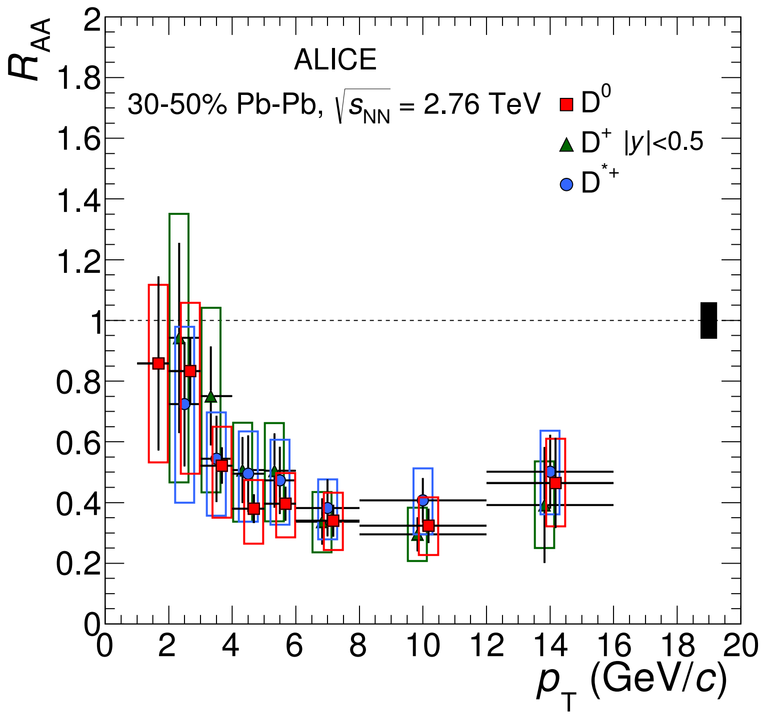

Figure 2.7: The ALICE experiment results of R_{PbPb} for centralities 30-50 % in 2.76 TeV collisions. D^+ are marked as triangles. Taken from Ref. [36].

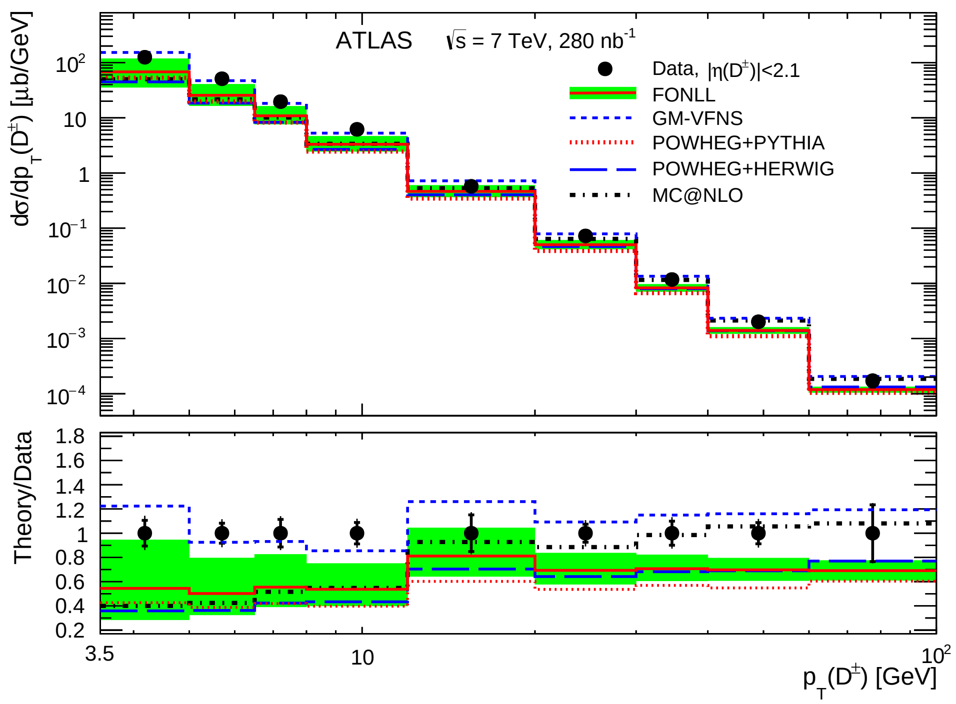

Figure 2.8: The ATLAS collaboration results of $D^{\pm}$ production cross section as a function of p_T in central rapidity and $3.5 < p_T < 100$ GeV/c range. Several theoretical predictions are shown, generally underestimating the data. Taken from Ref. [37].

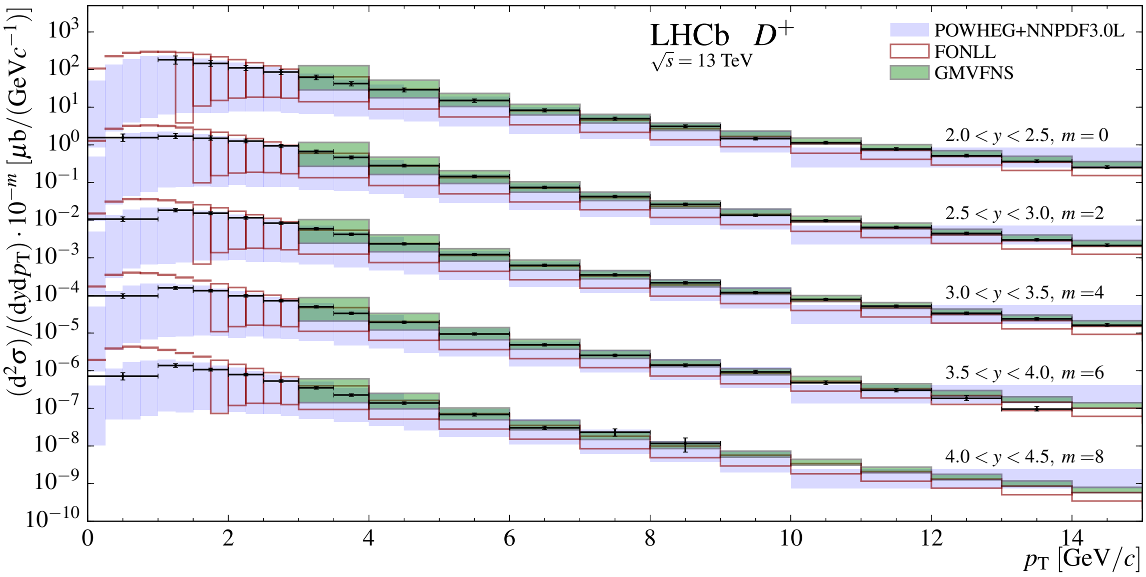

Figure 2.9: LHCb experiment results for the D^+ meson production cross-section as a function of p_T in forward rapidity in the $0 < p_T < 14$ GeV/c range. The results are further divided into different rapidity ranges (scaled by a factor of 10^{-m} for visibility). Taken from Ref. [38].

Chapter 3

STAR Experiment

As far as it is known, there is no way to study the QGP in the Universe other than when it is created in the collisions of ultrarelativistic heavy atomic nuclei. Only these collisions create sufficient energy density comparable to the early stages of the Universe. For this purpose, gold (and other) nuclei are accelerated at the Relativistic Heavy Ion Collider (RHIC, 3.1), which is located at the Brookhaven National Laboratory (BNL) in Upton, New York. Since there are hundreds of particles produced in each event, a complex particle detector is needed to detect all the tracks at the same time, to identify them and to trace them back to the point of their origin. The only currently operating experiment at RHIC is the STAR experiment, which consists of many subsystems described in sec. 3.2.

3.1 RHIC

The Relativistic Heavy Ion Collider (RHIC) located at BNL is the only currently operating accelerator designed specifically to produce heavy ion collisions at various energies. Furthermore, it is the only major accelerator capable of colliding polarized protons and therefore allowing measurements crucial to help our understanding of the proton spin. It consists of two hexagonal storage rings, each of them used for acceleration in the opposite direction. Superconductive dipole magnets are used to curve the track of the particles along the beampipe and (also superconductive) quadrupole magnets are used for focusing the beam to achieve maximum luminosity (up to $\sim 10^{27}$ $\mathrm{cm}^{-2}\mathrm{s}^{-1}$ for Au-Au collisions at $\sqrt{s_{NN}} = 200$ GeV [39]). The accelerator complex consists of the Electron Beam Ion Source, the Booster, the Alternating Gradient Synchrotron and RHIC. The entire complex is shown in Fig. 3.1. For more information about RHIC see [40], [41].

The basic technical design specifications of RHIC are summarized in Tab. 3.1.

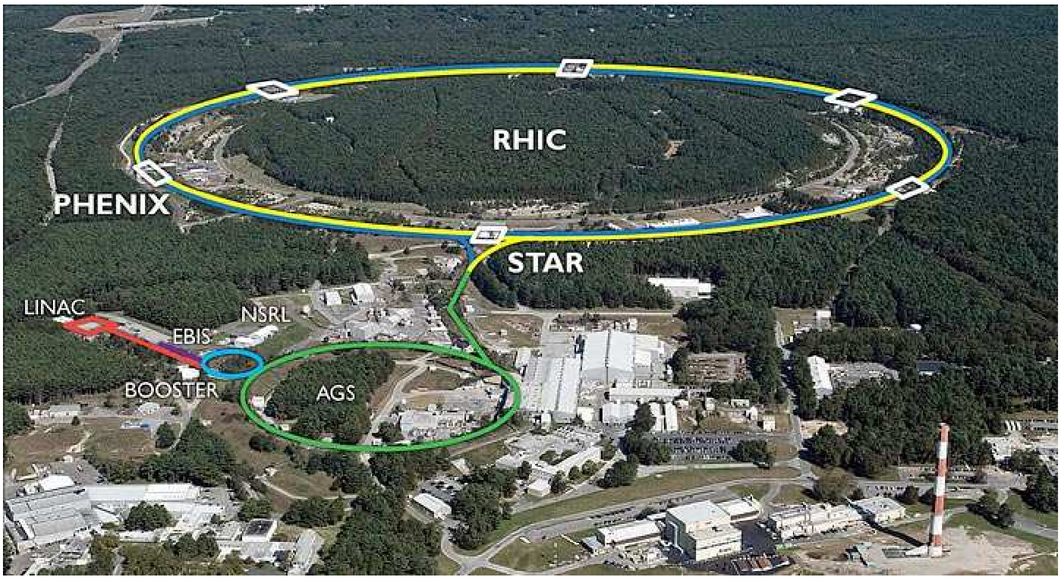

Figure 3.1: The BNL accelerator complex consisting of the Electron Beam Ion Source, multiple pre-accelerators and RHIC as the main accelerator. The position of STAR and PHENIX experiments shown as well. Taken from Ref. [42]

Circumference	3834 m
No. of dipole magnets	2×396
No. of quadrupole magnets	2×492
Operating magnetic field	3.5 T
Operating current	5.1 kA
Maximum beam energy	protons 250 GeV
	gold ions 100 GeV/N
No. of interaction points	6
Operating lifetime	10 h

Table 3.1: Basic RHIC technical design specifications. Taken from Ref. [41].

3.1.1 RHIC Future Plans

Short-term future plans for RHIC include isobaric nuclei collisions (Ru-Ru and Zr-Zr) and the second phase of the Beam Energy Scan (see [34]), which should lead to the confirmation of the critical point. This BES-II will include runs at lower energies ($\sqrt{s_{NN}}$ = 5 - 19.6 GeV) and fixed-target experiments (to cover the low-T, high μ_B region of the QCD phase diagram). Long-term plans include a rebuild of the current RHIC into eRHIC, the world's first electron-ion collider ([43]). This would open the door to all-new data and physics regarding the structure of nuclei.

3.2 STAR

The Solenoidal Tracker At RHIC (STAR) experiment is located at the 6 o'clock RHIC interaction point. It is a complex, multi-purpose particle detector consisting of many subdetectors such as the Time Projection Chamber (TPC, subsection 3.2.1), which is used to identify particles by measuring their ionization energy losses, the Time-of-Flight detector, which helps identifying the particles by measuring their velocity, the Barrel Electromagnetic Calorimeter (BEMC, 3.2.3), which measures the deposited energy, the Vertex Position Detector (VPD, 3.2.4) used for precise location of the primary vertex and the recently-installed Heavy Flavor Tracker (HFT, 3.2.5), which offers unprecedented accuracy in determination of secondary vertices. Another important part of the experiment is a 0.5 T magnet. The experiment has cylindrical geometry and is designed primarily for conducting measurements in the mid-rapidity region. The entire STAR experiment can be seen in Fig. 3.2 with key subdetectors highlighted.

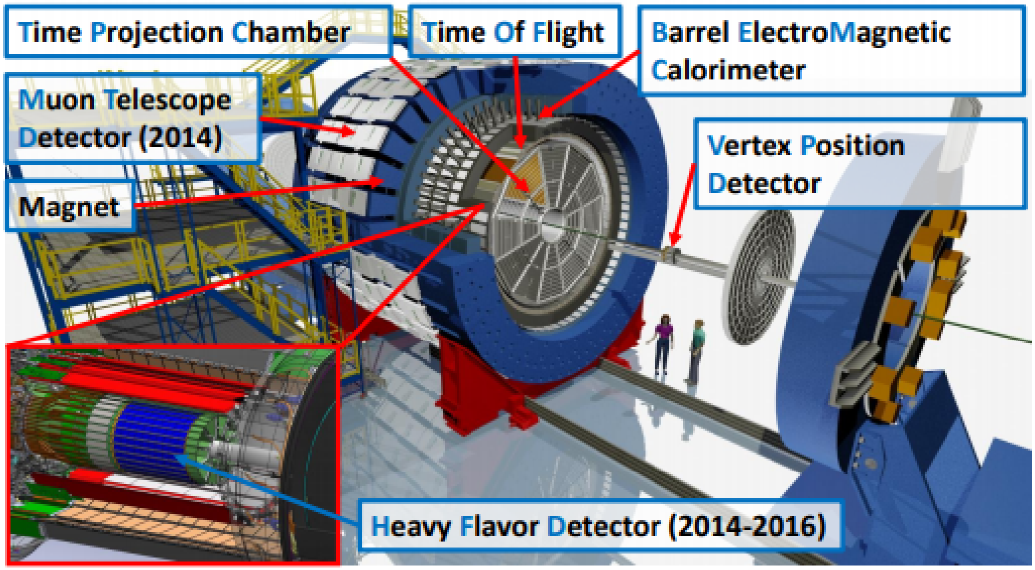

Figure 3.2: The STAR experiment scheme. Main parts, including magnet, TPC, TOF, BEMC, VPD and HFT (described as Heavy Flavor Detector) are highlighted. Taken from Ref. [2].

3.2.1 TPC

The Time Projection Chamber of the STAR detector is its most important part as it allows tracking and identification of charged particles via their ionization energy losses ($\frac{\mathrm{d}E}{\mathrm{d}x}$). The TPC is a cylinder 4.2 m long and 4 m in diameter. It has full azimuthal coverage and covers a pseudorapidity range of $\eta < |1.8|$. The fill gas used is the P10 gas mixture (90 % argon - for ionization, 10 % methane - for quenching) and the entire chamber is in uniform electric field E = 135 V.cm^{-1} [45] created by a conductive membrane which splits the TPC into two halves. The charged particle passing through the TPC interacts with the gas, creates electron-ion pairs and loses energy. The electrons then move towards the end caps. They are divided into 12 sectors further divided into inner and outer sector, each containing a Multi-Wire Proportional Chamber-based read-out system. There, the electrons are amplified by a factor of 1000-3000 to create detectable signal and their drift time is measured.

The TPC can measure the particle momentum in 100 MeV/c to 30 GeV/c range [45] with momentum resolution of $\sim 2\%$. The STAR TPC scheme can be seen in Fig. 3.3.

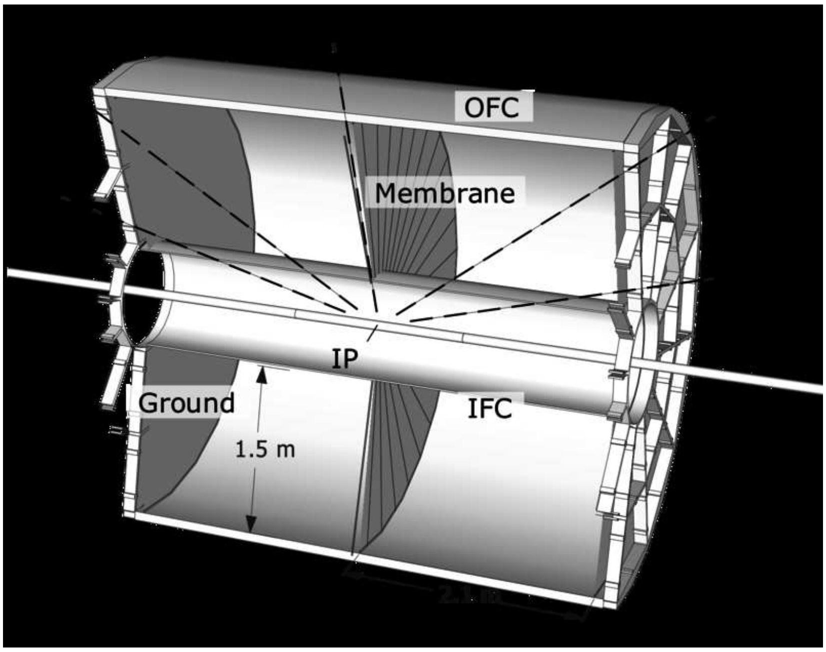

Figure 3.3: The STAR Time Projection Chamber scheme with main features highlighted, including IP - Intersection Point, IFC - Inner Field Cage and OFC - Outer Field Cage. Taken from Ref. [44].

3.2.2 TOF

The STAR Time-of-Flight detector helps with particle identification (PID) by measuring particle (inverse) velocities (the initial time t_0 is given by the VPD and the path Δs and momentum p of the particle is given by the TPC). The particle mass can then be calculated using

$$m = \frac{p}{c}\sqrt{\left(\frac{1}{\beta}\right)^2 - 1}, \tag{3.1}$$

where

$$\frac{1}{\beta} = c\frac{t - t_0}{\Delta s}, \tag{3.2}$$

where t is time detected by TOF, measured with resolution $\sim$ 80 ps. The detector, consisting of 120 Multi-gap Resistive Plate Chambers, is located just outside the TPC, inside the BEMC. It covers a full azimuthal angle and $\eta < |1|$ pseudorapidity range [46]. TOF serves as a complementary detector to the TPC, because it is effective in the low-momentum range.

3.2.3 BEMC

The Barrel Electromagnetic Calorimeter is located on the outside of the TOF detector, with inner radius of 2.2 m and outer radius o 2.6 m. The main detection module of the BEMC is a tower, composed of 20 lead and 21 scintillator layers. There are 4800 towers overall [47]. The BEMC covers full azimuthal angle and pseudorapidity range of $\eta < |1|$. The BEMC is used to measure the energy of charged particles and especially jets and is able to achieve energy resolution of about 2 %. The BEMC scheme can is shown in Fig. 3.4.

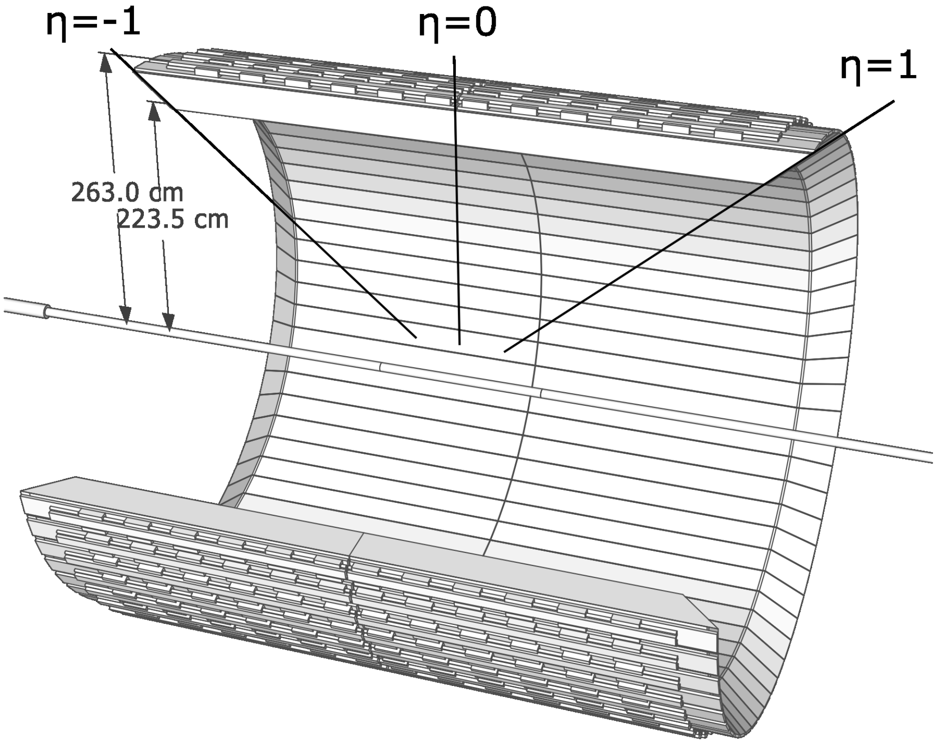

Figure 3.4: The Barrel Electromagnetic Calorimeter scheme. Taken from Ref. [44].

3.2.4 VPD

The Vertex Position Detector is located on both sides of the experiment, 5.6 m from the inteaction point along the beampipe. The VPD is used to determine the precise position of the primary vertex by measuring the difference between trigger times at both parts of the detector. The VPD also serves as a minimum-bias trigger in Au-Au collisions and the time information is used by other detectors such as the TOF, where it provides the initial time for particle inverse velocity calculation. For further details on the VPD see [48].

3.2.5 HFT

The Heavy Flavor Tracker si a silicon detector system located very close to the interaction point. The detector is composed of 4 layers in total, the two innermost layers are made from silicon pixel detector (PXL), the third layer (Intermediate Silicon Tracker - IST) is made of hybrid sensors and the outermost layer consists of silicon strip detectors (SSD). The detector is capable of tracking with resolution of about 20 μm for daughter particles with $p > 2$ GeV/c (see Fig. 3.5), which is crucial if we want to detect the secondary vertices created by decays of short-living heavy particles such as $D^{\pm}$ mesons, which have a mean decay length of $c\tau = 312$ μm. The HFT enables selecting triplets that come from the same secondary vertex and these triplets can then be classified as $D^{\pm}$ meson candidates. Without the HFT, the combinatorial background would be too high to obtain any significant signal from the data. Therefore, the HFT installation enables first measurement of $D^{\pm}$ production at RHIC. The HFT scheme is illustrated in Fig. 3.6, more on HFT can be seen in [50].

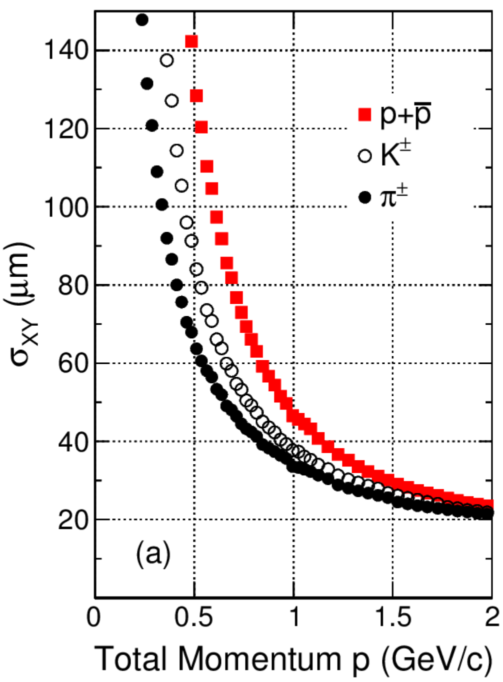

Figure 3.5: The HFT resolution for pions (full circles), kaons (empty circles) and protons (squares) as a function of momentum. Taken from Ref. [30].

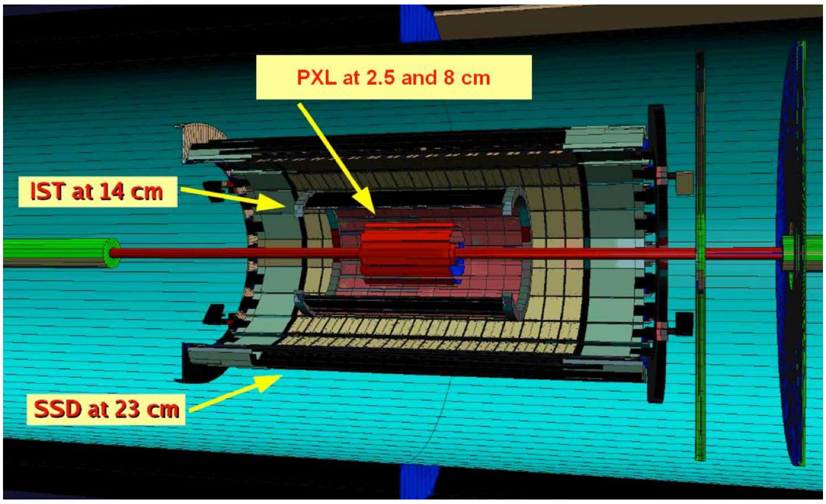

Figure 3.6: The Heavy Flavor Tracker at STAR scheme. The four detector layers are depicted. Taken from Ref. [49].

3.2.6 Recent and Planned Upgrades

The STAR experiment is continuously upgraded with new technologies in order to achieve maximum precision in its measurements. The recently installed detector systems are the Muon Telescope Detector (2012-14 [51]), which allows for the detection of muons and therefore opens new decay channels to be used (for example in quarkonia measurements), the HFT described in subsec. 3.2.5 and the Event Plane Detector (2017-18 [52]) which will allow to measure the event plane and centrality in the forward region. The future plans include the installation of a forward calorimeter, which would be helpful during the planned fixed target program [53].

Chapter 4

Reconstruction of Charmed Mesons in Heavy Ion Collisions

The main motivation for the $D^{\pm}$ signal and p_T spectrum reconstruction presented in this chapter is to improve the significance of the yields and to correct the systematic errors of results published in [3]. The dataset used for this analysis is described in sec. 4.1. Since the D^{+} and D^{-} mesons are antiparticles that are always created in pairs, they can be reconstructed together to achieve better statistics as their yield in each collision should be the same. The reconstruction was done using the $D^{\pm} \rightarrow K^{\mp} + \pi^{\pm} + \pi^{\pm}$ decay channel, as is usual for the $D^{\pm}$ analysis, since this is the decay channel with the highest branching ratio (8.98 ± 0.28 %) of all $D^{\pm}$ hadronic decays. Some key properties of the $D^{\pm}$ meson are shown in Tab. 4.1. Several cuts (selection criteria) were applied to obtain correct $D^{\pm}$ yields. Cuts can be classified into 4 categories: event selection, track selection, particle identification (PID) and topological cuts. The cuts were applied in two waves - during the candidate selection (sec. 4.2) and during the raw yield extraction (sec. 4.3). The raw yield was then corrected to produce so-called invariant yield independent on the number of events analyzed (sec. 4.4). The systematic errors are also discussed in this section.

Quark content	$c\bar{d}$, $\bar{c}d$
Mass [MeV]	1869.5 ± 0.4
Mean lifetime [ps]	1.040 ± 0.007
Mean path ($c\tau$) [μm]	312 ± 2
Decay channel	$D^{\pm} \rightarrow K^{\mp}\pi^{\pm}\pi^{\pm}$
Branching ratio [%]	8.98 ± 0.28

Table 4.1: Table of several basic $D^{\pm}$ meson properties. Taken from [1].

4.1 Dataset

The dataset used for this thesis were minimum-bias data from RHIC 2014 run with Au-Au collisions at center-of-mass energy per nucleon $\sqrt{s_{NN}} = 200$ GeV, production

P16id with library SL16d. Triggers used were: 450050, 450060, 450005, 450015 and 450025. The data used were stored in picoDst files which are produced during the third stage of data pre-analyzing from the MuDst data which are in turn produced from the raw data detected during the process of data taking. In total, 1.33 billion events were used for this analysis.

4.2 Candidate Selection

The candidate selection consisted mainly of event selection cuts, PID and track selection. As for event selection, the maximum distance of the primary vertex from the interaction point along the beampipe obtained from the TPC was set to $|V_z| < 6$ cm and the maximum distance from the center given by the Vertex Position Detector was set to $|V_{zVPD}| < 3$. About 900 million events passed the cuts, however, since the HFT efficiency was low for runs before day ∼108, those runs were discarded and the number of events was reduced to about 800 million. Out of that number, about 20 million events did not have proper centrality defined and therefore were neglected. 781 020 736 minimum-bias events were accepted in the end.

For the track to be accepted, it was required to have hits in all 3 active HFT layers (2 PXL layers and the IST layer) in use and a minimum of 15 hits in the TPC.

The PID was done using so-called hybrid TOF approach. When the track could be detected by the TOF detector, both TPC and TOF information was used, otherwise only the TPC information was used to identify the particle. In the TPC, the particles are identified by their ionization energy loss. Here the important value is

$$n_\sigma = \frac{\ln \frac{\mathrm{d}E/\mathrm{d}x}{\langle \mathrm{d}E/\mathrm{d}x \rangle}}{R_{\mathrm{d}E/\mathrm{d}x}}, \tag{4.1}$$

where $\mathrm{d}E/\mathrm{d}x$ is an energy loss measured by the TPC, $R_{\mathrm{d}E/\mathrm{d}x}$ is the TPC resolution and $\langle \mathrm{d}E/\mathrm{d}x \rangle$ is a mean energy loss given by the Bichsel function for this particle (Fig. 4.1).

This value corresponds to the number of standard deviations from the theoretical energy loss we are still willing to tolerate for a given particle. Originally, these cuts were set to $|n_\sigma| < 3$ for both pions and kaons as this cut assures that almost no particles will be lost but the contamination by different kind of particles is not prominent. Cuts for distance of closest approach (DCA) between $K\pi$ and $\pi\pi$ pairs was set to be lower than 90 μm and the distance between the primary and secondary vertices - equal to the D meson decay length - was set to lie between 30 and 2000 μm. Tracks were combined into $K\pi\pi$ triplets and subsequently flagged according to the charges of the daughter particles. There are 8 possible charge combinations. Two of them could be corresponding to decaying D^+ ($K^-\pi^+\pi^+$) or D^- ($K^+\pi^-\pi^-$) mesons. These are referred to as correct-sign combinations while the others ($K^+\pi^+\pi^-$, $K^+\pi^-\pi^+$, $K^+\pi^+\pi^+$, $K^-\pi^+\pi^-$, $K^-\pi^-\pi^+$ and $K^-\pi^-\pi^-$) are called wrong-sign combinations or background. This would lead to the background being approximately three times higher than the signal. The invariant

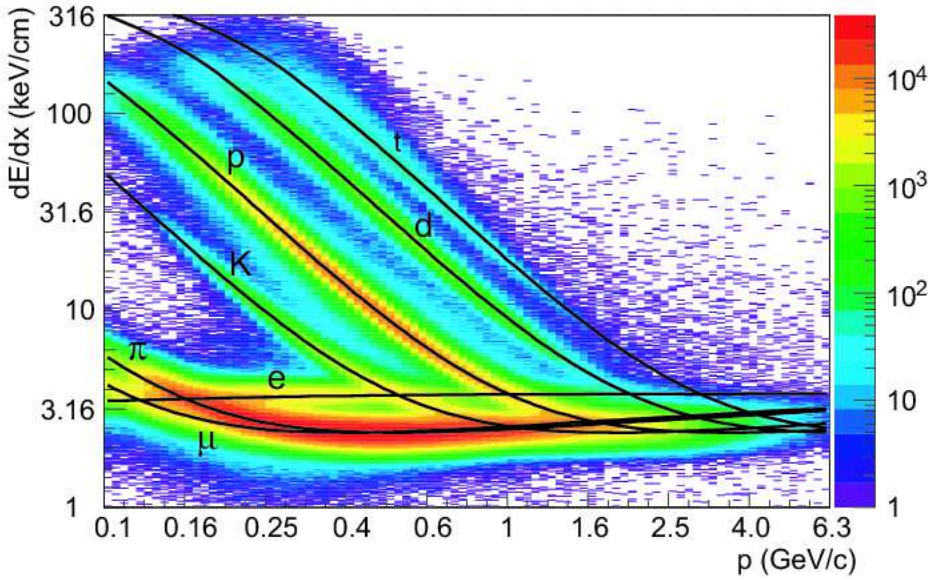

Figure 4.1: Plot of energy loss for common charged particles. The Bichsel functions (corresponding to mean energy loss) are shown as the black lines. In this thesis, the important ones are pions and kaons. Taken from Ref. [54].

mass of these triplets was calculated using the formula $mc^2 = \sqrt{E^2 - |\overrightarrow{p}|^2c^2}$ and restricted to $1.7 < mc^2 < 2.1$, around the expected $D^{\pm}$ mass. Some of these cuts were then tightened during the following yield extraction phase. The last applied cut in this stage was the pointing angle cut. The pointing angle is the angular difference between the reconstructed combined momentum vector direction and the line connecting primary and secondary vertices). The angle should be equal to zero to satisfy the law of conservation of momentum, however, that is not the case in real data. Here, the cut was set as follows: $\cos\theta < 0.997$. It is up for discussion, whether this cut is too restrictive or not. All triplets that passed these cuts are from now on referred to as candidates.

4.3 Raw Yield Extraction

To further distinguish between some 29.44 million triplets that passed through the candidate selection process, a second wave of cuts was applied. This wave consisted mainly (but not exclusively) of topological cuts and tightening of some previous cuts to make the raw yield extraction from the candidates possible. The tightened cuts were the number of TPC hits ($15 \to 20$), kaon n_σ ($3 \to 2$) and the maximum of DCA between any two tracks ($90 \to 80$ μm). Among the newly applied cuts, the inverse velocity difference between theoretically calculated value and the value measured by the TOF detector was set to $|\frac{1}{\beta} - \frac{1}{\beta_{th}}| < 0.03$ for both pions and kaons when available . The pseudorapidity cut was set to $|\eta| < 1$ because of the TOF coverage. To assure that the daughter particles originate from the secondary vertex and not the primary, daughters DCA to the primary vertex was required to be at least 100 μm for pions and 80 μm for kaons. For the daughters the transverse momentum cut was set to

$p_T > 0.5$ GeV/c, while the D mesons needed $p_T > 1$ GeV/c. The last applied cut was $\Delta_{max} < 200$ μm, where Δ_{max} is the longest side of a triangle formed by the three reconstructed vertices - each from one pair ($K\pi_1$, $K\pi_2$ or $\pi_1\pi_2$) - to be certain, that the secondary vertex was reconstructed with sufficient precision. The topology of the $D^{\pm} \rightarrow K^{\mp}\pi^{\pm}\pi^{\pm}$ decay is illustrated in Fig. 4.2

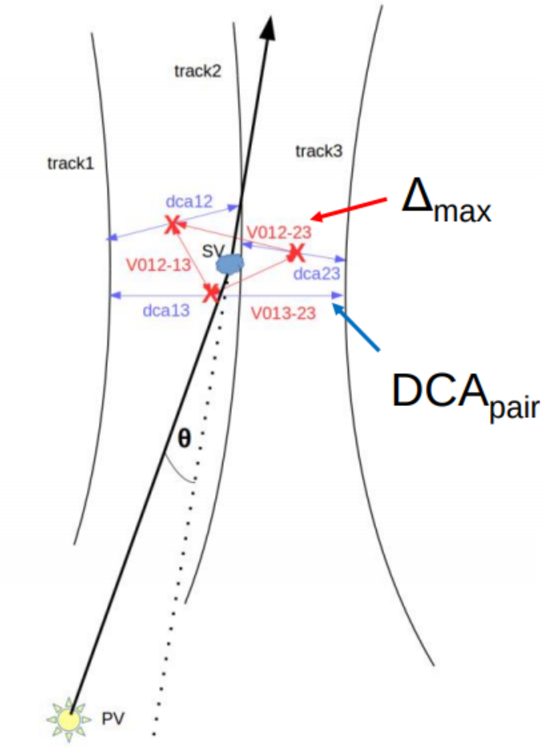

Figure 4.2: An illustration of the $D^{\pm} \rightarrow K^{\mp}\pi^{\pm}\pi^{\pm}$ decay with important topological features highlighted. PV - primary vertex, SV - secondary vertex and θ - pointing angle, DCA_{pair} - distance of closest approach between two tracks. Δ_{max} - longest side of the vertex triangle. Taken from [2].

All final cuts are summarized in table 4.2.

After all cuts were applied, some 660 000 correct-sign combinations and about 1.9 million wrong-sign combinations remained. These were then divided into 13 p_T and 3 centrality bins. The next step consisted of scaling the background. For this purpose, the correct-sign histograms were fitted with Gaussian + first order polynomial function, the sigma of the Gaussian was calculated and all correct-sign and wrong-sign histograms were integrated outside of the 3σ range. The background histograms were then scaled by the correct-sign-to-background ratio and, finally, the background was subtracted from the correct-sign histogram to obtain the signal histogram. An example of this task for two centrality and p_T bins can be seen in Fig. 4.11 for the $2.5 < p_T < 3.0$ GeV/c bin and in Fig. 4.12 for the $5.5 < p_T < 6.0$ GeV/c bin, both for the 10 % most central collisions. Invariant mass distributions for all other available bins are shown in A.

Type	Cut	Value(s)
Event Selection	Distance from primary vertex	$\lvert V_z \rvert < 6$ cm
	VPD distance from PV	$\lvert V_{zVPD} \rvert < 3$
Track Selection	TPC Hits	$N_{TPC} > 20$
	HFT Hits	All 3 layers
	Pseudorapidity	$\lvert \eta \rvert < 1$
PID	Daughter transverse momentum	$p_T > 0.5$ GeV/c
	D meson transverse momentum	$p_T > 1$ GeV/c
	Daughter TOF inverse velocity	$\lvert \frac{1}{\beta} - \frac{1}{\beta_{th}} \rvert < 0.03$
	TPC energy loss deviation - pions	$\lvert n_\sigma \rvert < 3$
	TPC energy loss deviation - kaons	$\lvert n_\sigma \rvert < 2$
Topological Cuts	Daughter pairs DCA	$DCA_{pair} < 80$ μm
	D meson decay length	$30 < c\tau < 2000$ μm
	Vertex triangle side length	$\Delta_{max} < 200$ μm
	Pointing angle	$\cos\theta < 0.997$
	Pion DCA to primary vertex	$DCA_\pi > 100$ μm
	Kaon DCA to primary vertex	$DCA_K > 80$ μm

Table 4.2: Table summarizing the cuts used to obtain the raw yield. Cuts are further described in the text. Related distributions are shown in 4.3, 4.4, 4.5, 4.6, 4.7, 4.8, 4.9 and 4.10.

To obtain the raw yield and significance, this signal histogram was then fitted with a Gaussian and integrated inside the 3σ range. Raw yield Y is then equal to the value of the integral while significance S was calculated from:

$$S = \frac{Y}{\sqrt{C+B}}, \tag{4.2}$$

where C is the value of the integral of correct-sign histograms inside the 3σ range and B is the integral of scaled background in the same range. The denominator of eq. 4.2 is also equal to the raw yield statistical error.The significance itself stands for the confidence level (expressed in standard deviations) that the observed peak is not a result from random fluctuations, but rather is originating from a $\mathrm{D}^\pm$ meson decay. Raw yields calculated for various p_T bins between $p_T = 1$ GeV/c and $p_T = 14$ GeV/c and for 4 centrality bins can be seen in Tab. 4.3 along with the corresponding significance of the peak. Yields with $S < 3$ were dismissed as insignificant.

The mean of the Gaussian used to fit the signal histogram should then be equal to the mass of the $\mathrm{D}^\pm$ meson (1869.59 MeV/c^2 [1]) and the σ of the Gaussian corresponds to the $\mathrm{D}^\pm$ mass resolution. The values of measured $\mathrm{D}^\pm$ mass m_D and σ for all available centrality and transverse momentum bins can be seen in Fig. 4.13 and Fig. 4.14 and are summarized in Tab. 4.4.

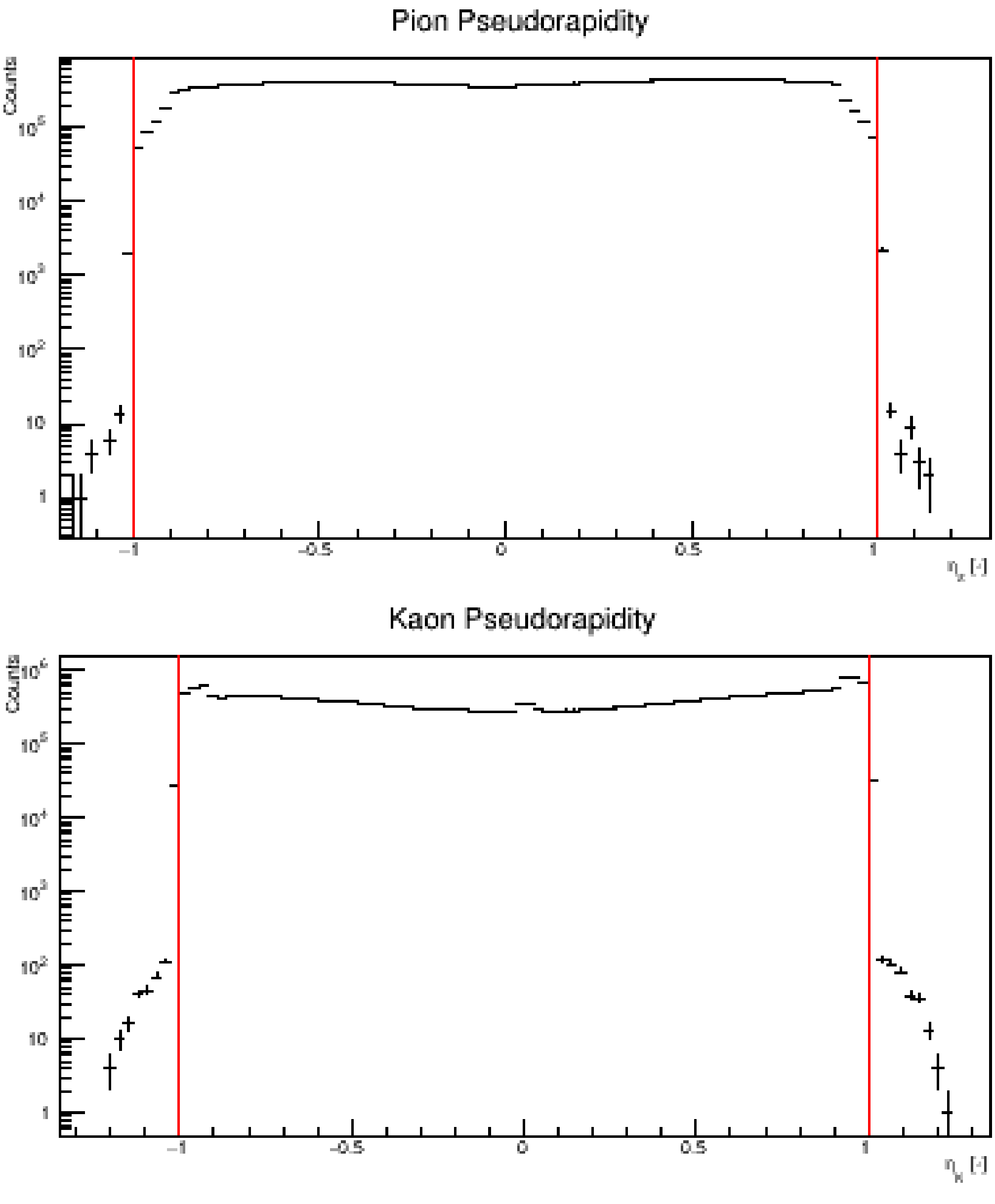

Figure 4.3: Pseudorapidity distribution of pions (top) and kaons (bottom) with red lines drawn to show the cut. Values within these lines were accepted.

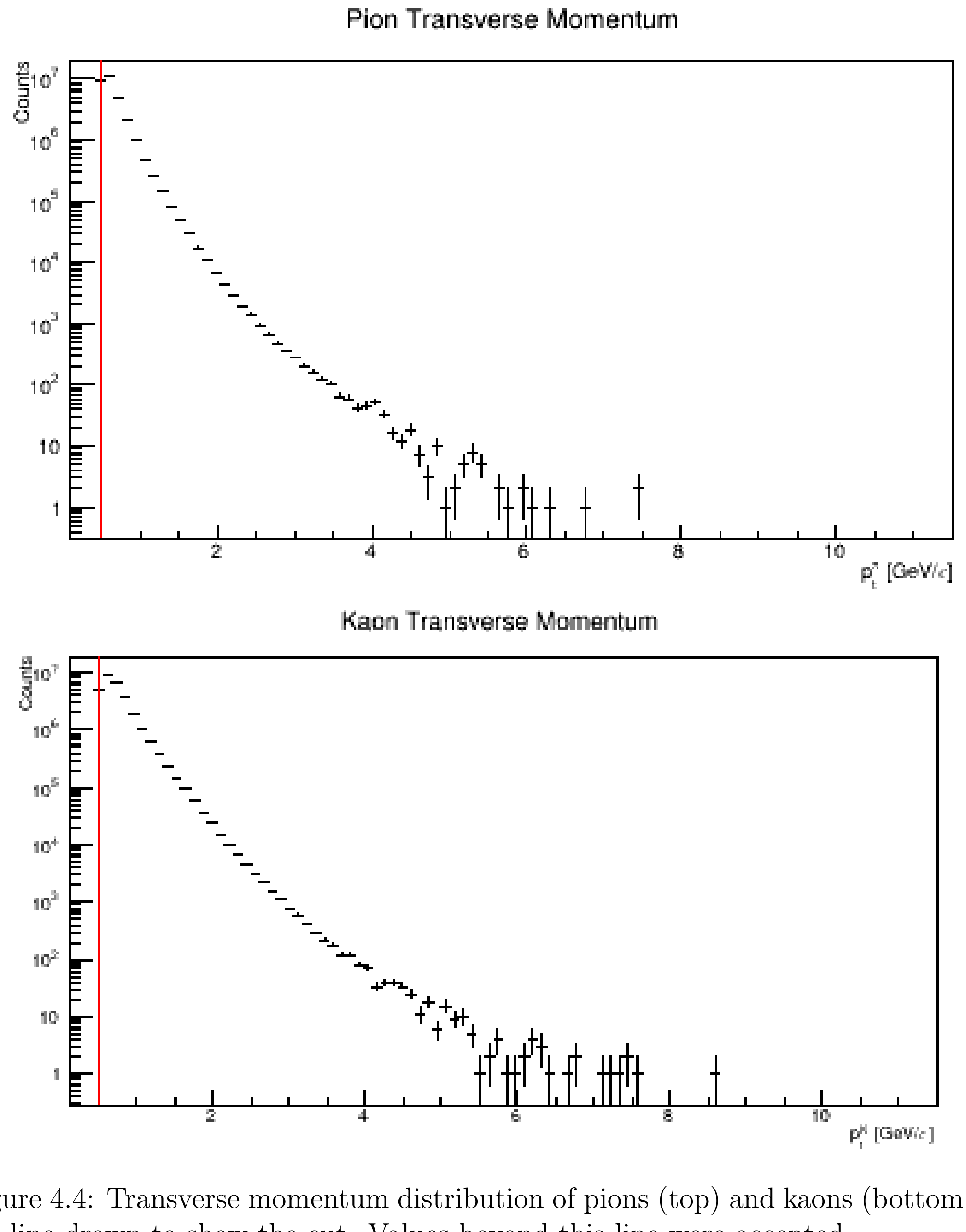

Figure 4.4: Transverse momentum distribution of pions (top) and kaons (bottom) with red line drawn to show the cut. Values beyond this line were accepted.

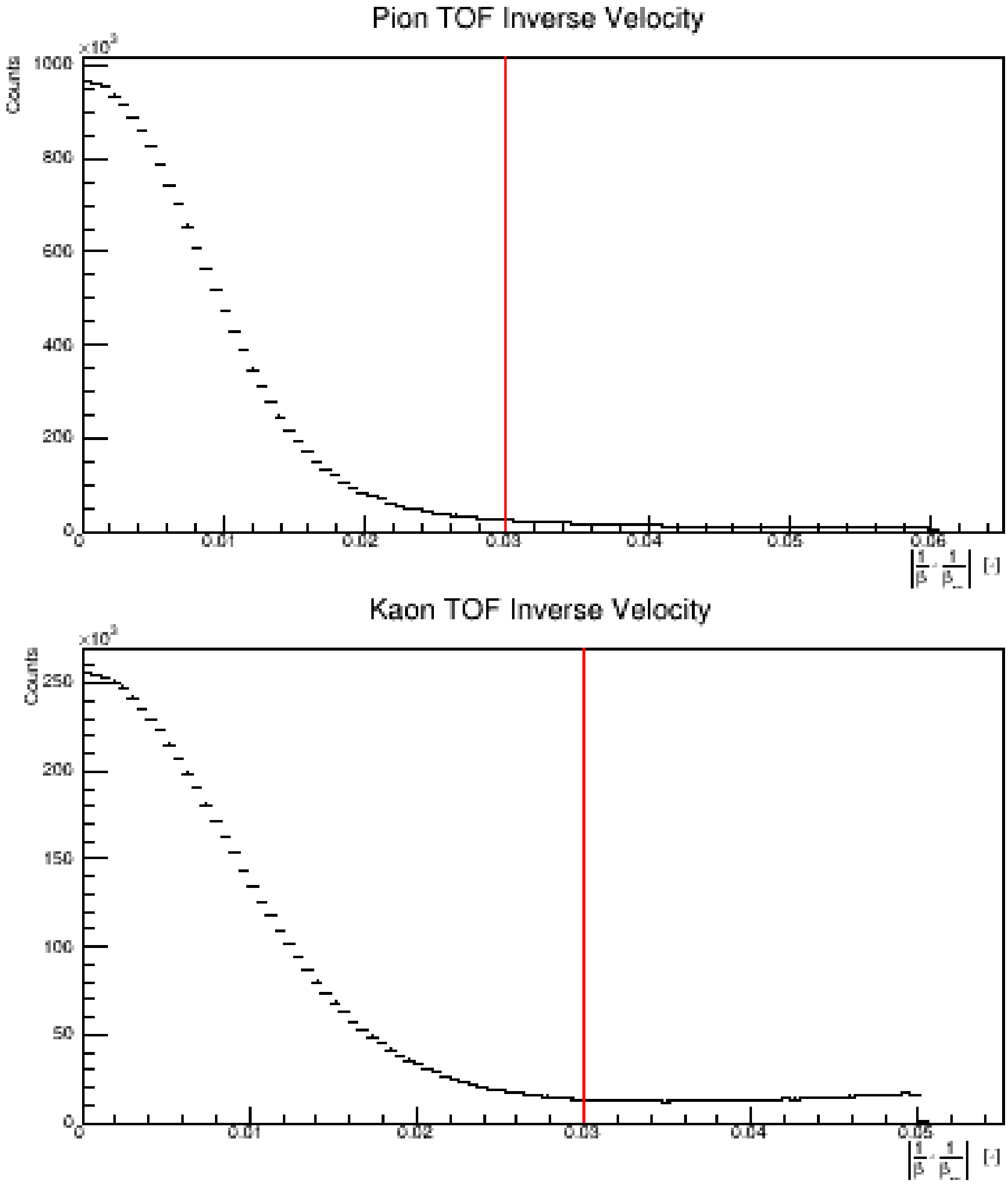

Figure 4.5: Inverse velocity deviation distribution of pions (top) and kaons (bottom) as measured by the ToF detector. Values before the red line were accepted

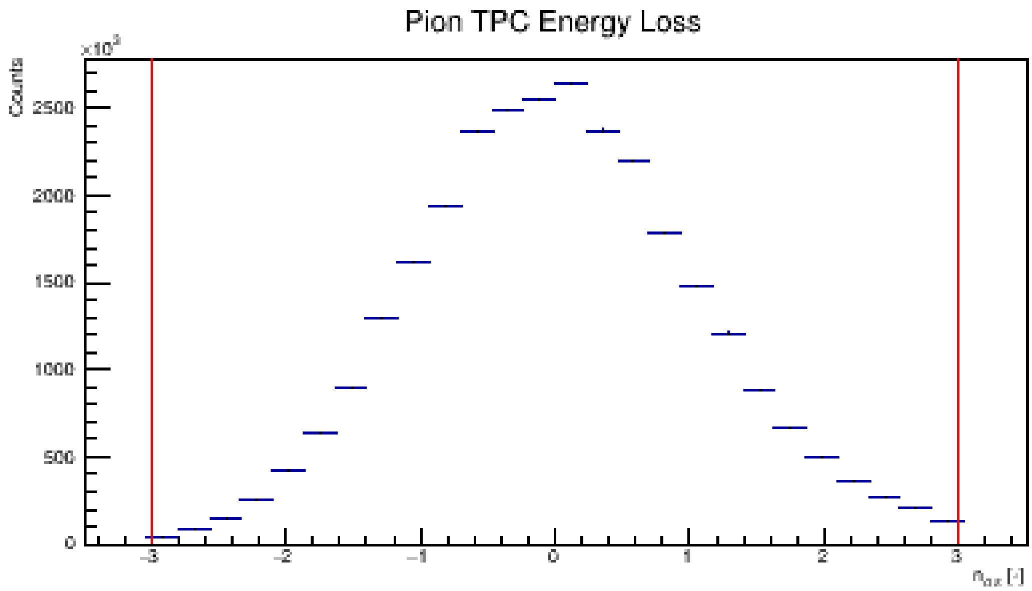

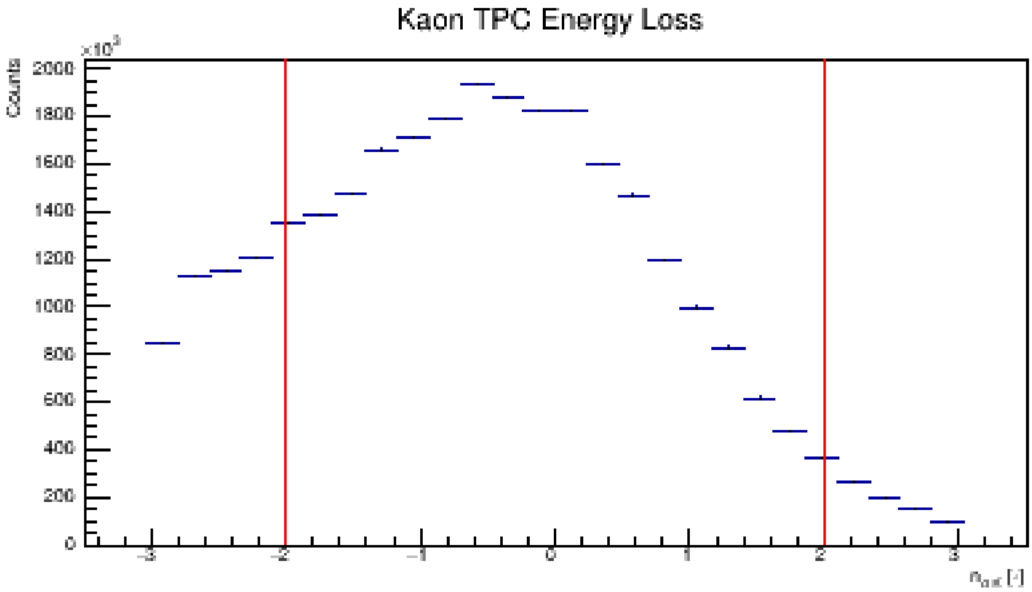

Figure 4.6: Energy loss deviation distribution of pions (top) and kaons (bottom) as measured by the TPC, with red lines drawn to show the cut. Values within these lines were accepted.

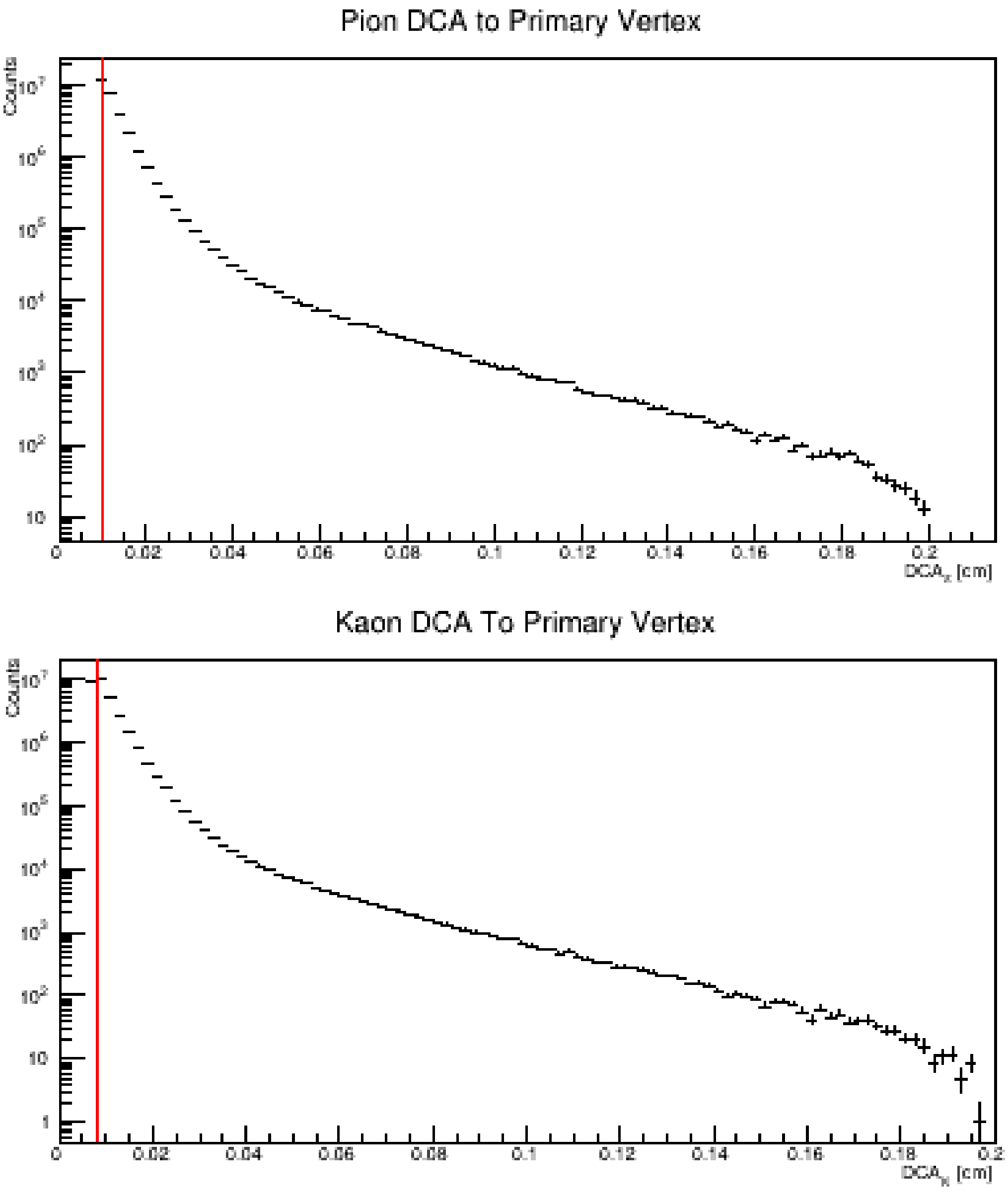

Figure 4.7: DCA to the primary vertex distribution of pions (top) and kaons (bottom) with red line drawn to show the cut. Values beyond this line were accepted.

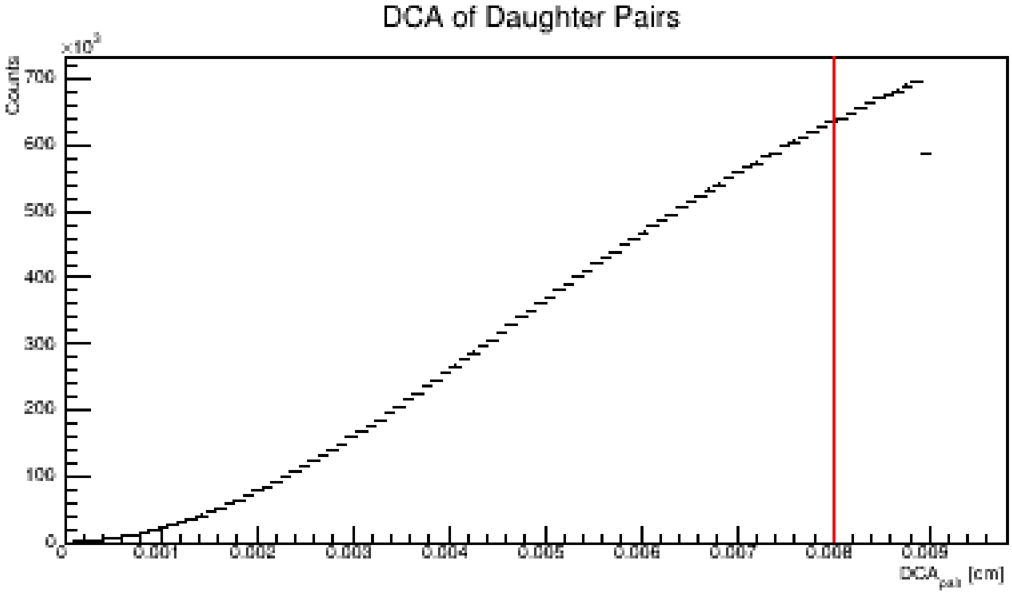

Figure 4.8: Distribution of the DCA of daughter pairs. Values to the left of the red line were accepted.

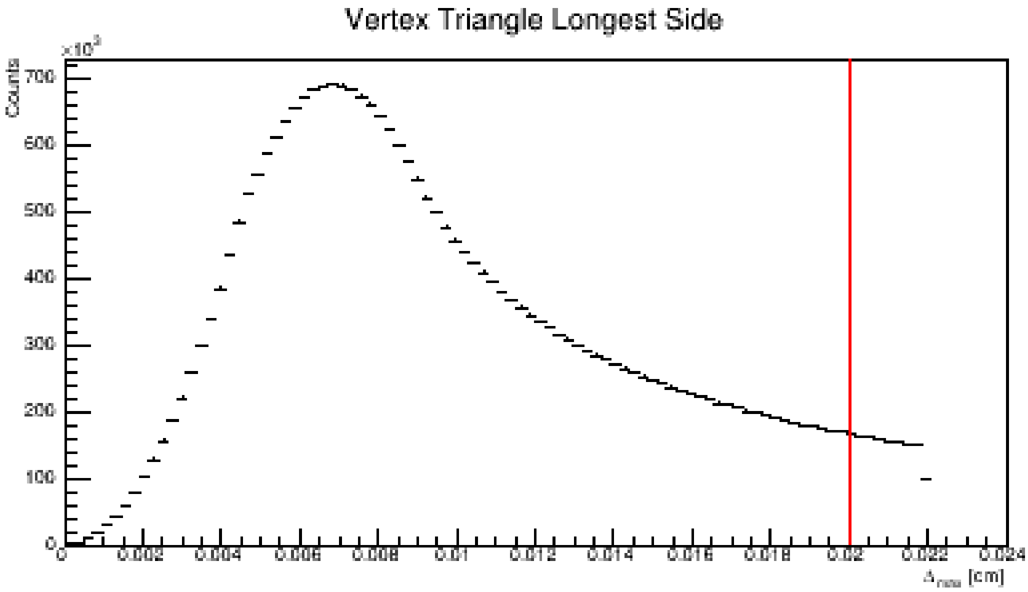

Figure 4.9: Vertex triangle longest side distribution with cut shown as the red line. Values to the left of this line were accepted.

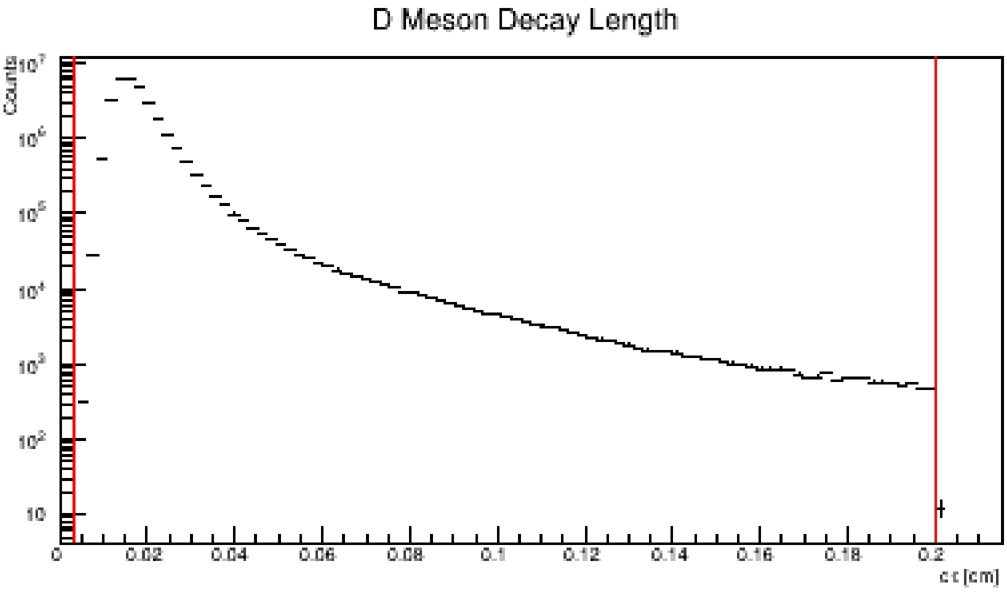

Figure 4.10: Distribution of the decay length of the $D^{\pm}$ meson. Values within the red lines were accepted.

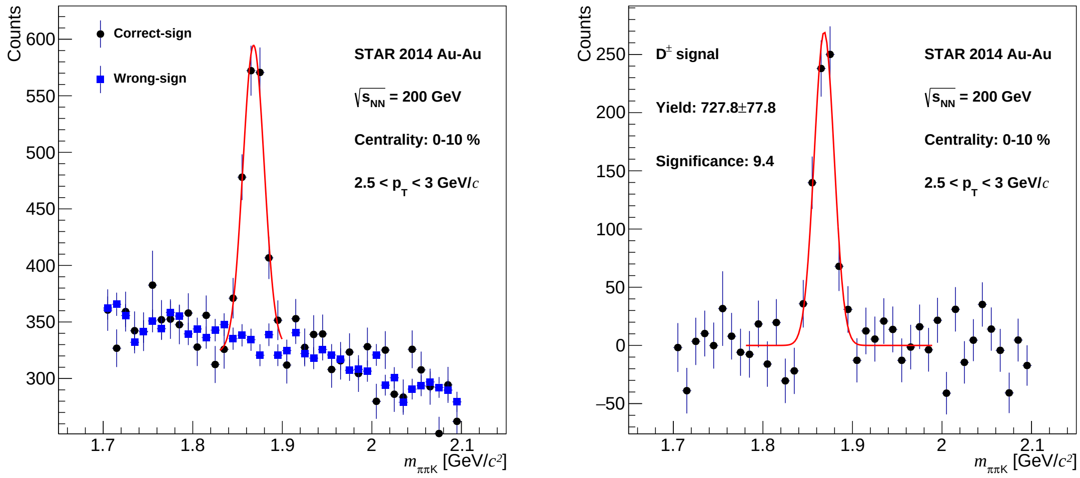

Figure 4.11: Left: invariant mass distribution of correct-sign and scaled wrong-sign $K\pi\pi$ triplets with clearly visible peak fitted by a Gaussian + linear function. Right: Plot of $K\pi\pi$ invariant mass after the subtraction of scaled background, with a clearly observable peak around the expected $D^{\pm}$ mass, fitted by a Gaussian function. Calculated raw yield and significance is also shown. Both plots are made for the 10 % most central collisions in the $2.5 < p_T < 3.0$ GeV/c bin.

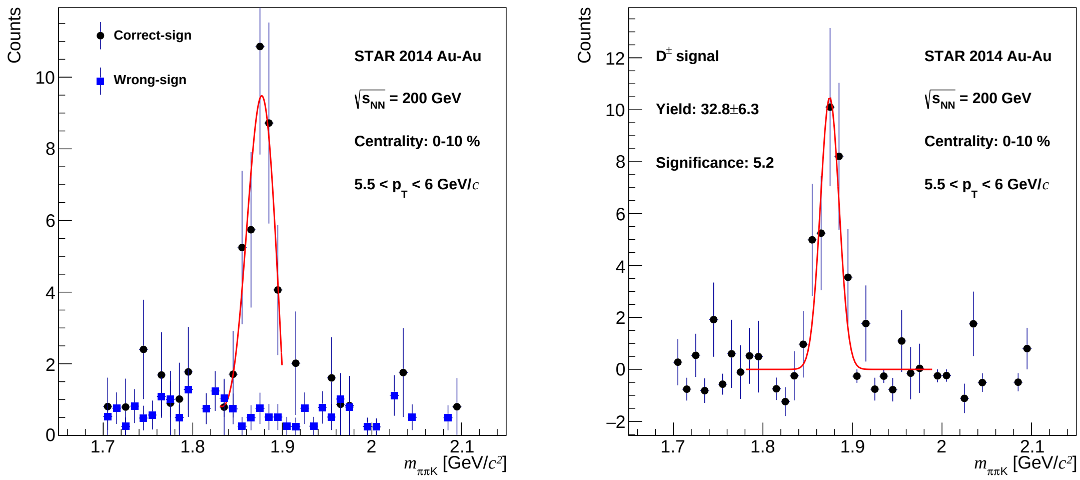

Figure 4.12: Left: invariant mass distribution of correct-sign and scaled wrong-sign $K\pi\pi$ triplets with clearly visible peak fitted by a Gaussian + linear function. Right: Plot of $K\pi\pi$ invariant mass after the subtraction of scaled background, with a clearly observable peak around the expected $D^{\pm}$ mass, fitted by a Gaussian function. Calculated raw yield and significance is also shown. Both plots are made for the 10 % most central collisions in the $5.5 < p_T < 6.0$ GeV/c bin.

p_T [GeV/c]	0-10 %		10-40 %		40-80 %		0-80 %	
	Yield [-]	Sig. [-]	Yield [-]	Sig. [-]	Yield [-]	Sig. [-]	Yield [-]	Sig. [-]
1.0-2.0	425±234	1.8	1221±258	4.7	384±46	8.3	2073 ± 406	5.1
2.0-2.5	485±142	3.4	1700±119	14.3	447±28	16.1	2638 ± 188	14.1
2.5-3.0	728±78	9.4	2683±72	23.2	482±24	19.8	2895 ± 109	26.5
3.0-3.5	471±43	10.9	1221±47	26.1	393±21	18.9	2081 ± 66	31.6
3.5-4.0	278±26	10.9	806±34	23.9	264±17	15.2	1344 ± 45	29.6
4.0-4.5	167±18	9.2	461±25	18.8	163±14	12.0	798±34	23.8
4.5-5.0	78±12	6.8	288±19	15.1	96±12	8.3	466 ±25	18.4
5.0-5.5	56±10	5.7	177±15	11.6	54±8	6.7	294±20	14.7
5.5-6.0	33±6	5.2	97±11	8.5	31±6	4.8	162±15	11.1
6.0-7.0	24±6	3.7	97±11	8.6	29±6	4.8	150±14	10.5
7.0-8.0	9±3	3.0	28±7	3.9	9±3	2.6	46±9	5.3
8.0-10.0	3±3	1.2	14±5	2.7	9±3	2.9	23±7	3.3
10.0-14.0	-	-	5±3	1.7	-	-	4±3	1.2

Table 4.3: Table of raw yields of $D^{\pm}$ meson for various p_T and centrality ranges along with corresponding peak significances. Yields with significance lower that 2.6 were dismissed.

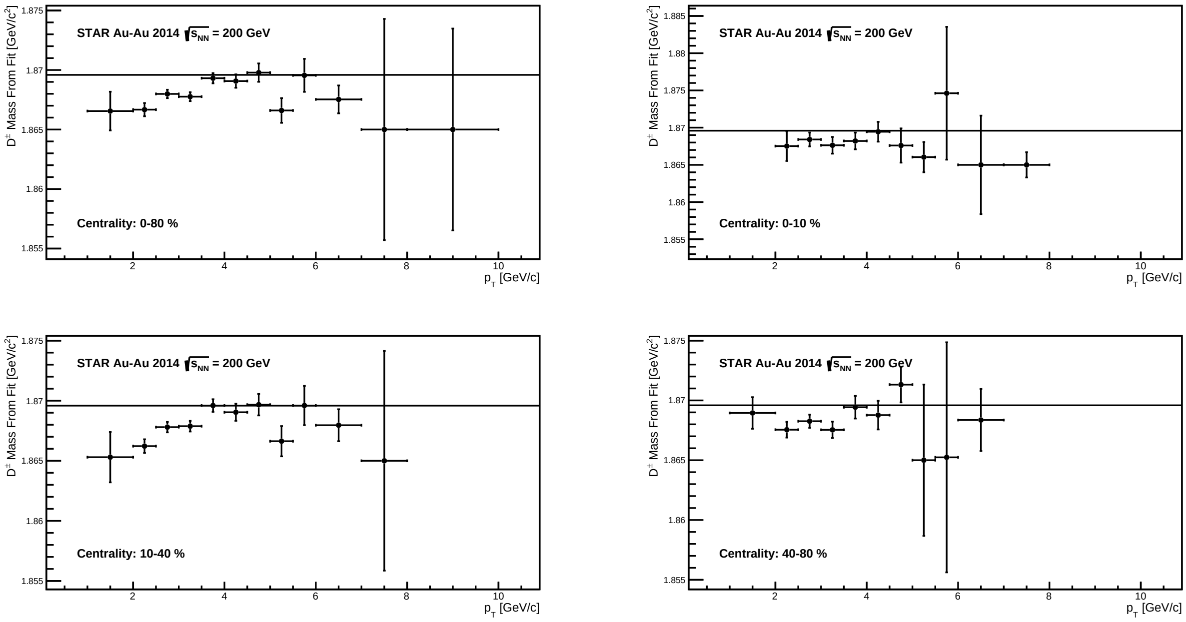

Figure 4.13: D$^{\pm}$ mass obtained from fit of signal histogram for centralities 0-80 % (top, left), 0-10 % (top, right, note different scale), 10-40 % (bottom, left) and 40-80 % (bottom, right) for all available transverse momentum bins. The solid black line at 1.86959 GeV/c^2 indicates the D$^{\pm}$ mass presented in [1].

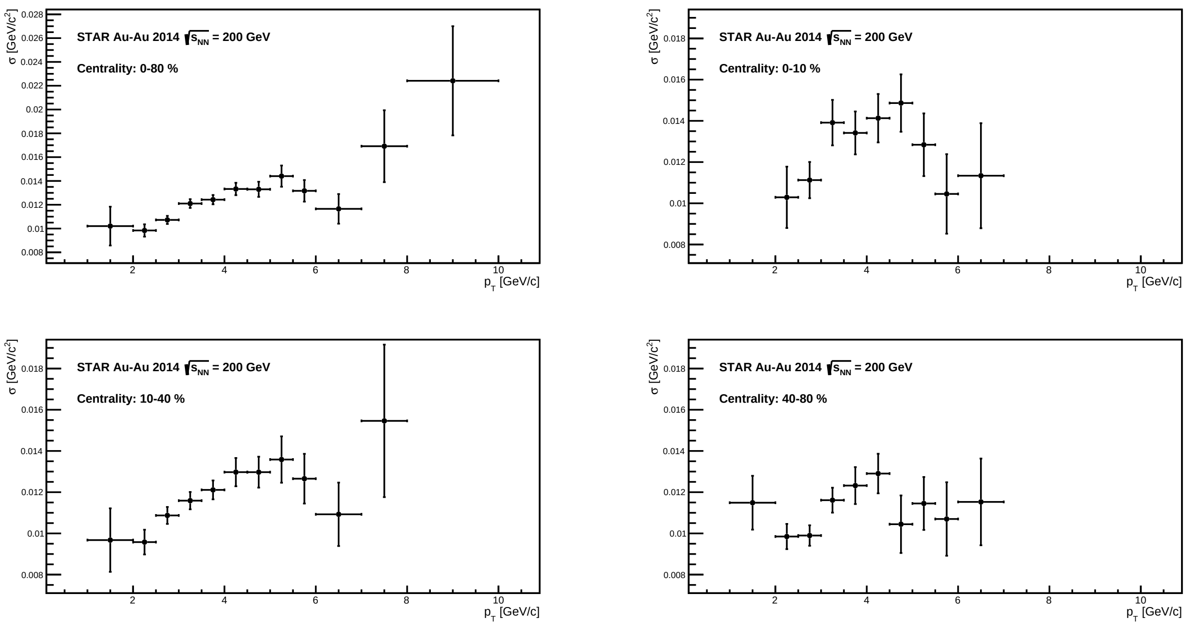

Figure 4.14: D$^{\pm}$ mass resolution obtained from the fit of signal histogram for centralities 0-80 % (top, left, note different scale), 0-10 % (top, right), 10-40 % (bottom, left) and 40-80 % (bottom, right) for all available transverse momentum bins.

p_T [GeV/c]	0-10 %		10-40 %		40-80 %		0-80 %	
	m_D [GeV/c^2]	σ [GeV/c^2]	m_D [GeV/c^2]	σ [GeV/c^2]	m_D [GeV/c^2]	σ [GeV/c^2]	m_D [GeV/c^2]	σ [GeV/c^2]
1.0-2.0	-	-	1.865±0.002	0.097±0.002	1.869±0.001	0.011±0.001	1.867±0.002	0.010±0.002
2.0-2.5	1.868±0.002	0.010±0.001	1.8662±0.0006	0.0096±0.0006	1.8676±0.0007	0.0 98±0.0006	1.8667±0.0006	0.0098±0.0005
2.5-3.0	1.8684±0.0009	0.0111±0.0009	1.8678±0.0004	0.0109±0.0004	1.8683±0.0006	0.0099±0.0005	1.8680±0.0004	0.0107±0.0003
3.0-3.5	1.867±0.001	0.014±0.001	1.879±0.0004	0.0116±0.0004	1.8675±0.0007	0.0116±0.0006	1.8678±0.0004	0.0121±0.0004
3.5-4.0	1.868±0.001	0.013±0.001	1.8696±0.0005	0.0121±0.0005	1.8694±0.0009	0.0123±0.0009	1.8693±0.0004	0.0124±0.0004
4.0-4.5	1.869±0.001	0.014±0.001	1.8690±0.0007	0.0130±0.0007	1.869±0.001	0.0129±0.0010	1.8691±0.0006	0.0133±0.0005
4.5-5.0	1.868±0.002	0.015±0.001	1.8697±0.0009	0.0130±0.0007	1.871±0.001	0.010±0.001	1.8698±0.0008	0.0133±0.0006
5.0-5.5	1.866±0.002	0.013±0.002	1.866±0.001	0.014±0.001	1.865±0.006	0.011±0.001	1.866±0.001	0.0144±0.0009
5.5-6.0	1.875±0.009	0.010±0.002	1.870±0.002	0.013±0.001	1.865±0.010	0.011±0.002	1.870±0.001	0.0132±0.0009
6.0-7.0	1.865±0.007	0.011±0.003	1.868±0.001	0.011±0.002	1.868±0.003	0.012±0.002	1.868±0.001	0.012±0.001
7.0-8.0	1.865±0.002	0.0060±0.0009	1.865±0.009	0.015±0.004	-	-	1.865±0.009	0.017±0.003
8.0-10.0	-	-	-	-	-	-	1.865±0.008	0.022±0.005

Table 4.4: $D^{\pm}$ meson mass m_D obtained from fit and the mass resolution σ for various transverse momentum and centrality ranges. The values are also shown in Fig. 4.13 and Fig. 4.14.

4.4 Yield Correction & Systematic Errors

Because the raw yield is always dependent on the number of collisions, it would be difficult to compare it to results from any dataset other than the one used for this analysis. Therefore, a normalized version of the raw yield - called the invariant yield - is often calculated. The normalization is done by applying the formula

$$\frac{\mathrm{d}^2 N}{\mathrm{d}p_T \mathrm{d}y} \frac{1}{2\pi p_T} = \frac{Y_{raw}}{2\pi N_{ch} \cdot N_{events} \cdot BR \cdot p_T \cdot \Delta p_T \cdot \Delta y \cdot Eff(p_T)}, \tag{4.3}$$

where Y_{raw} is the raw yield, $N_{ch} = 2$ is the number of different meson charges, N_{events} is the number of events analyzed (see Tab. 4.5), $BR = 8.98 \pm 0.28$ % is the $D^{\pm} \to K^{\mp} + \pi^{\pm} + \pi^{\pm}$ decay branching ratio, p_T is the mean p_T of the bin (which is a subject to correction in 4.4.1), Δp_T is the p_T bin length, $\Delta y = 2$ is the rapidity interval size and $Eff(p_T)$ is the STAR detector's acceptance×efficiency (see 4.4.2).

Centrality [%]	$N_{events} \cdot 10^6$ [-]
0-10	124.7
10-40	304.8
40-80	351.6
0-80	781.0

Table 4.5: Number of events analyzed for each centrality bin.

4.4.1 Transverse Momentum Correction

Since the invariant yield is required to be independent of the transverse momentum. Therefore, the raw yield is to be divided by the average p_T of the corresponding bin. Unfortunately, the correct p_T value is not a trivial mean value, but rather a weighted average dependent on the shape of the p_T spectrum inside the bin. An iterative correction method is used to obtain the correct p_T points. First, the invariant yield is calculated for each p_T bin using the $p_T = \frac{p_{Tmin}+p_{Tmax}}{2}$ approximation, where p_{Tmin} and p_{Tmax} are the end points of the bin. The invariant yield spectrum is then fitted using the Levy function

$$f(p_T) = \frac{a}{2\pi} \cdot \frac{(c-1)(c-2)}{((bc+m)(m(c-1)+bc))} \cdot \left(\frac{bc + \sqrt{p_T^2 + m^2}}{bc+m} \right)^{-c}, \tag{4.4}$$

where $m = 1.870$ GeV/c^2 is the - theoretical - mass of D$^{\pm}$ meson and a, b and c are real parameters determined from the fit. From this, the function value of the new point is calculated using the relation

$$f(p_{T0}) = \frac{\int_{p_{Tmin}}^{p_{Tmax}} f(p_T) \mathrm{d}p_T}{\Delta p_T}, \tag{4.5}$$

and then it is possible to finally obtain the new p_{T0} point. This process will, however, naturally change the invariant yield (4.3), so it is necessary to re-calculate it with the new p_T values. Since the fit would be slightly different this time, this calculation will in turn change the correct position of the p_T points, so this is an iterative process and 3 iterations were required. The spectrum does not change within accuracy of 10^{-5} after the third iteration. This process will naturally have larger impact on wider bins, as can be seen (for the 0-80 % centrality bin) in Fig. 4.15. The result of this p_T point correction is summarized in Tab. for all centralities.

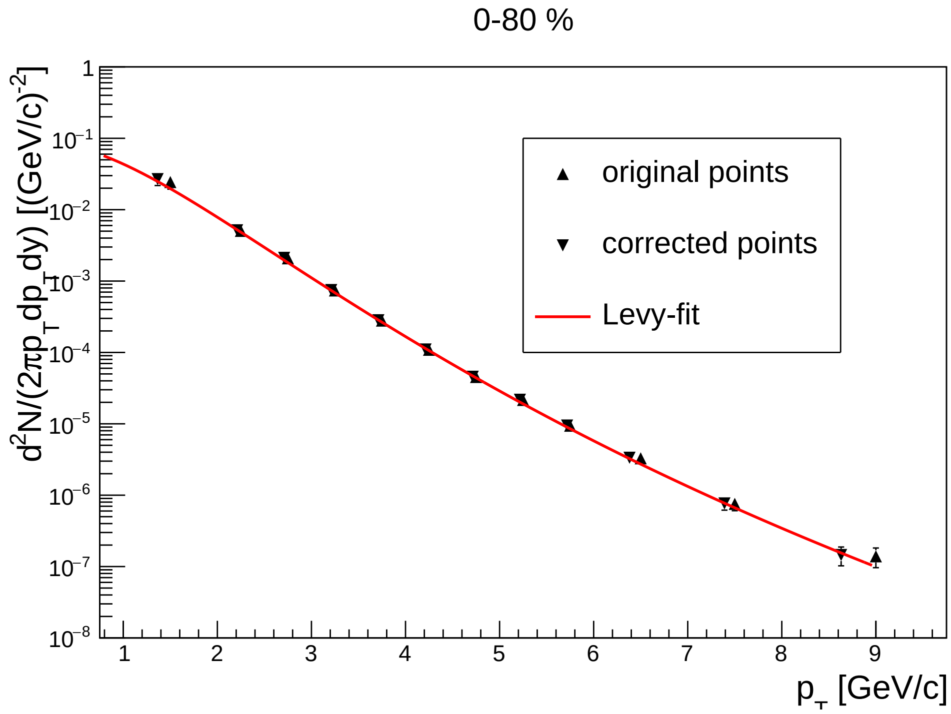

Figure 4.15: The correction in p_T point position as a result of the spectrum shape inside the bins for the 0-80 % centrality region. The points are fitted with the Levy function (4.4). The errorbars include both statistical and systematic errors (see 4.4.3).

4.4.2 Detector Acceptance×Efficiency

The $Eff(p_T)$ value contains information about the STAR detector's geometrical acceptance and the efficiency of each detector subsystem that was used in this analysis (HFT, TPC, TOF - when available). A simulation done by Jakub Kvapil [3], which uses a data-driven fast simulator with an overall systematic error of 5 %, was used to determine the value of $Eff(p_T)$ for each p_T and centrality bin. The points were then fitted by a non-physical function (4.6)to smoothen the shape and reduce the binning effect.

$$Eff(p_T) = Ae^{-(\frac{B}{p_T})^C} e^{-(\frac{p_T - D}{E})^2}, \tag{4.6}$$

where A, B, C, D and E are real parameters of the fit. The values of these parameters can be seen in Tab. 4.7 and the fitted points are shown in Fig. 4.16 along with the

p_T range [GeV/c]	Original p_T bin center [GeV/c]	Corrected p_T bin center[GeV/c]			
		0-10 %	10-40 %	40-80 %	0-80 %
1.0-2.0	1.50	-	1.36	1.38	1.36
2.0-2.5	2.25	2.21	2.21	2.21	2.21
2.5-3.0	2.75	2.71	2.71	2.71	2.71
3.0-3.5	3.25	3.21	3.21	3.21	3.21
3.5-4.0	3.75	3.71	3.71	3.71	3.71
4.0-4.5	4.25	4.21	4.21	4.21	4.21
4.5-5.0	4.75	4.71	4.71	4.72	4.72
5.0-5.5	5.25	5.22	5.22	5.22	5.22
5.5-6.0	5.75	5.72	5.72	5.72	5.72
6.0-7.0	6.50	6.38	6.38	6.38	6.38
7.0-8.0	7.50	7.39	7.39	-	7.39
8.0-10.0	9.00	-	-	-	8.63

Table 4.6: Table of original and corrected p_T points for all 4 centrality bins. Calculated by fitting the data by the Levy function (4.4).

corresponding data/fit ratio. It can be seen that the fit function does not describe the simulated points correctly in the lowest part of the spectrum and therefore needs to be improved for future analysis.

Centrality	A	B	C	D	E
0-10 %	3.3±0.3	12.1±0.4	0.94±0.02	-99±1	50.4±0.4
10-40 %	8±1	14.2±0.9	0.88±0.02	-100±20	50.1±0.9
40-80 %	3±2	14±2	0.88±0.07	-93±7	53±3
0-80 %	7±9	15±4	0.87±0.08	-100±100	49±4

Table 4.7: Table of (rounded) fit paremeters for the detector $Eff(p_T)$ simulation.

4.4.3 Yield Systematic Errors

The total error of the measurement can be determined from the efficiency×acceptance simulation systematic error ($\sigma_{sys_{sim}} = 5$ %), the branching ratio uncertainty ($\sigma_{sys_{BR}} = 3.1$ %) and both systematic and statistic uncertainty of the raw yield using the relation $\sigma_{tot} = \sqrt{\sigma^2_{sys_Y} + \sigma^2_{sys_{BR}} + \sigma^2_{sys_{sim}} + \sigma^2_{stat_Y}}$. The raw yield systematic error determination is done by observing the changes of the yield, that were caused by the variations of some variables the yield is independent of (and therefore should in theory stay the same). This task will be done in the near future after this thesis. These variations will consist of changing several cuts, the binning and the fitting range, always one at a time and then calculating the raw yield. These planned variations are shown in Tab. 4.8, with planned variations being 10 %, with the exception of the last 3. The magnitude of all variations is, however, still a subject of discussion. Another planned task is to investigate the correlations between the systematic uncertainties as this should reduce the overall measurement uncertainty.

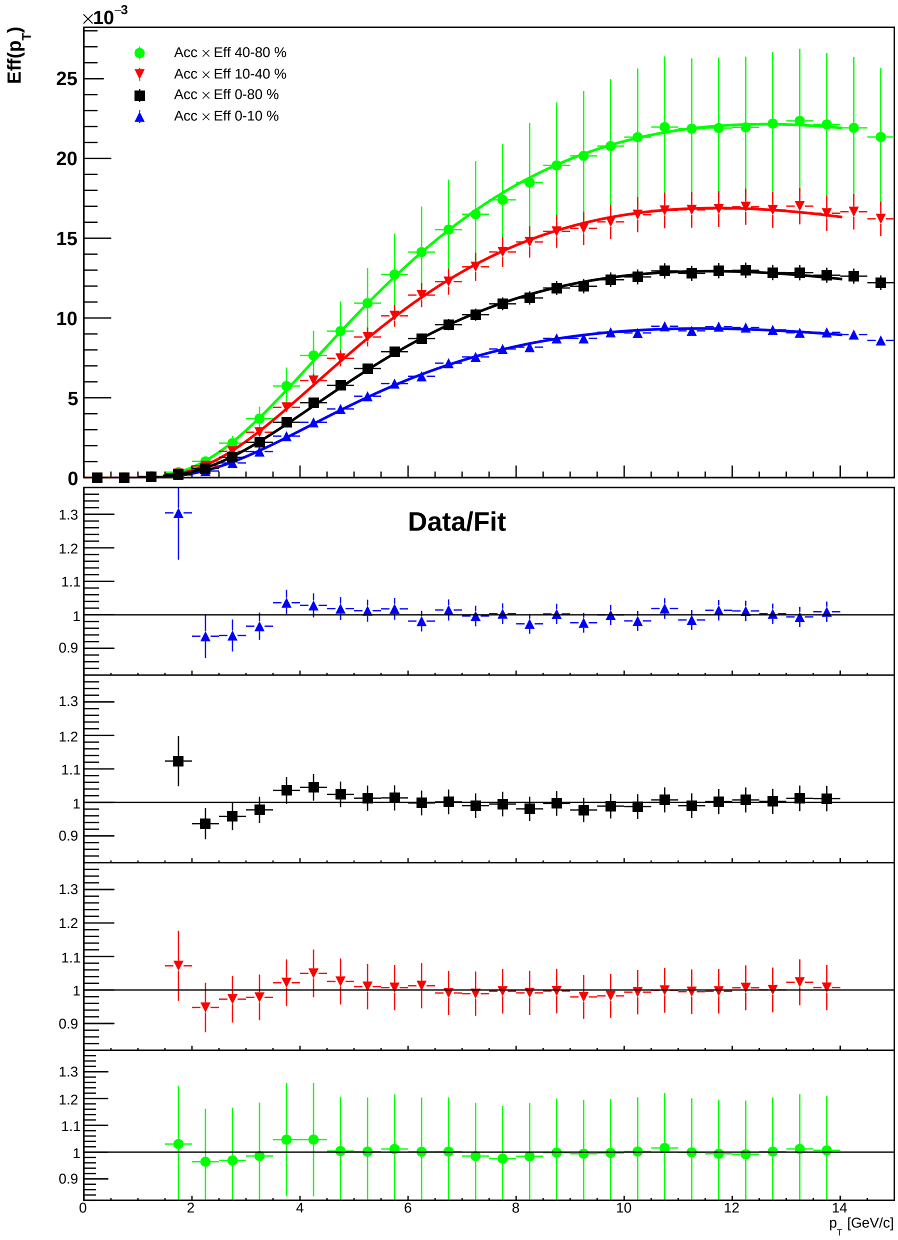

Figure 4.16: Fitted simulation points of detector acceptance×efficiency $Eff(p_T)$ for centrality bins 0-10 % (blue), 0-80 % (black), 10-40 % (red) and 40-80 % (top) and data/fit comparison (bottom). Simulation done by J. Kvapil [3], fit parameters are summarized in Tab. 4.7.

4.4.4 Corrected Yield

After applying all the corrections mentioned in subsections above, it was possible to obtain a $D^{\pm}$ meson p_T spectrum and compare it with the results obtained by Jakub Kvapil [3]. The results are consistent within uncertainties with each other, as can be seen in Fig. 4.17, where both results for the 0-80 % centrality bin are shown along with their ratio. This ratio is for most points consistent with unity as was expected as the analysis was conducted for nearly identical data subset. The only exception is the first

Cut	Change
Daughter p_T	$500 \rightarrow 550$ MeV/c
Daughter DCA from PV	pions $100 \rightarrow 90$ μm
	kaons $80 \rightarrow 72$ μm
Daughter pair DCA	$80 \rightarrow 88$ μm
Vertex triangle side	$200 \rightarrow 220$ μm
TPC Hits	$20 \rightarrow 15$
Binning	$50 \rightarrow 40$
Fit range	$1.78 - 1.99 \rightarrow 1.83 - 1.92$

Table 4.8: Planned cut, binning and fit range variations to determine the raw yield systematic error.

point ($p_T = 1 - 2$ GeV/c). However, since the $Eff(p_T)$ calculation shown in subsec. 4.4.2 is not correct in this range, the position of this point (for all centralities where available) should not be alarming. The results for the most central collisions (0-10 %) can be seen in Fig. 4.18, showing slight difference between expected and actual results. The invariant yield seems lower, but no strong conclusions should be made because of rather large errors.

The $D^{\pm}$ spectrum for the mid-peripheral (10-40 %) centrality range shows great agreement with results from [3] with the ratio being consistent with unity within the uncertainties for all p_T bins as can be seen in Fig. 4.19. As for the peripheral collisions - centralities between 40-80 % - the ratio of the both measurements differs by a factor of about 2 for the lowest p_T bin, but then converges towards unity with higher transverse momentum. As mentioned before, the position of the first point should not be considered significant, because the $Eff(p_T)$ calculation in this region is not correct.

There are several reasons for the differences observed when comparing the two results. The first one is the non-identical data subset used. In [3] there was a larger sample of 858 million events to 781 million events used for this thesis. The cause of this discrepancy is not known yet, but will be investigated further in near future. The analysis presented in [3] shows inconsistency in used pointing angle cut (both $\cos\theta < 0.996$ and $\cos\theta < 0.998$ are mentioned in the work). Another difference is that this work uses the latest measured value of the decay channel branching ratio (8.98 %), while [3] uses older value of 9.13 %. This gives an instant systematic deviation of about 2 %. Another change implemented in this thesis was the process of p_T points correction. In [3], the points were moved along the x-axis only and the yield (y-axis position) was not recalculated with the new value of p_T. It seems correct to recalculate the yield, since applying formula 4.3 with wrong p_T values results in wrong invariant yield results. It might also be worth investigating the differences between the fits for the $Eff(p_T)$ simulation. It is also important to note that the systematic errors are not final and will be recalculated in the near future.

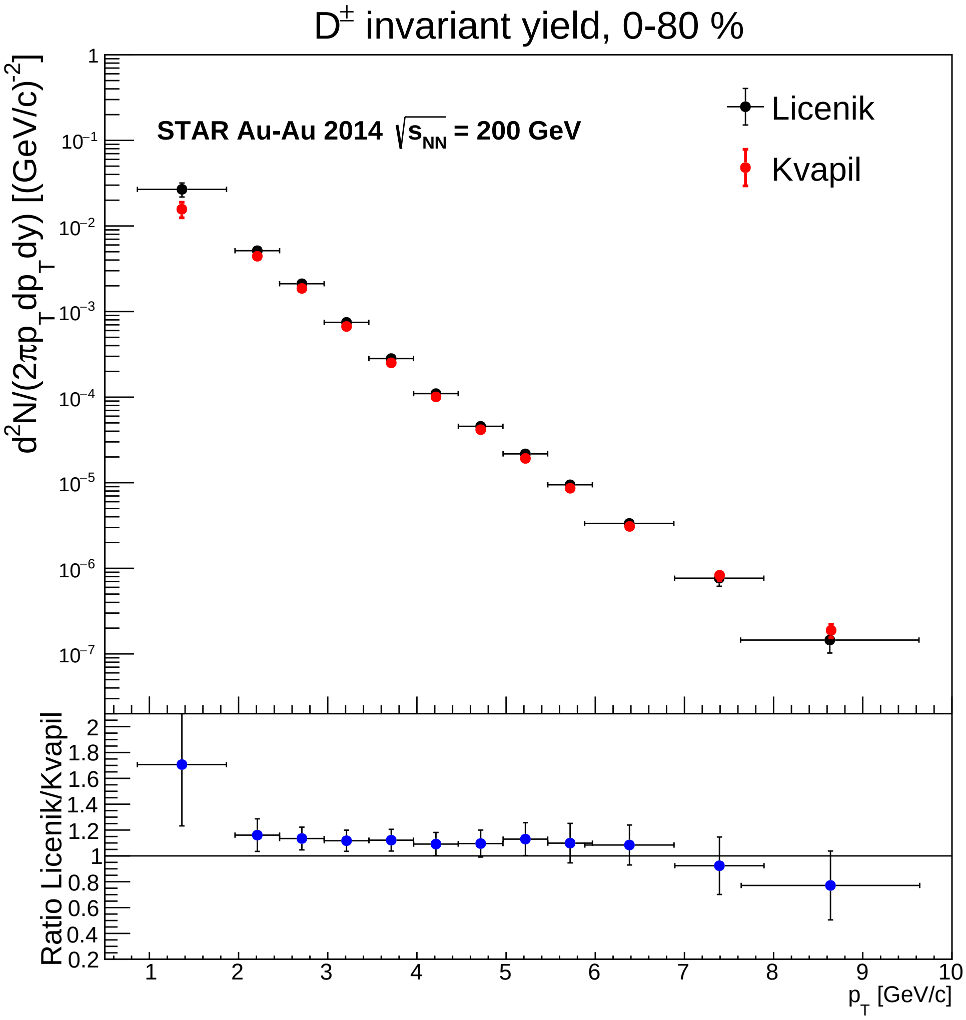

Figure 4.17: The $D^{\pm}$ p_T spectrum (invariant yield) obtained in this thesis (black points) and compared with results from [3] (red points), along with the ratio of these two results (blue points) for centrality bin 0-80 %. The vertical errorbars contain both systematic and statistical errors while the horizontal errorbars show correctly only the width of the corresponding p_T bin, not the actual endpoints of the bin.

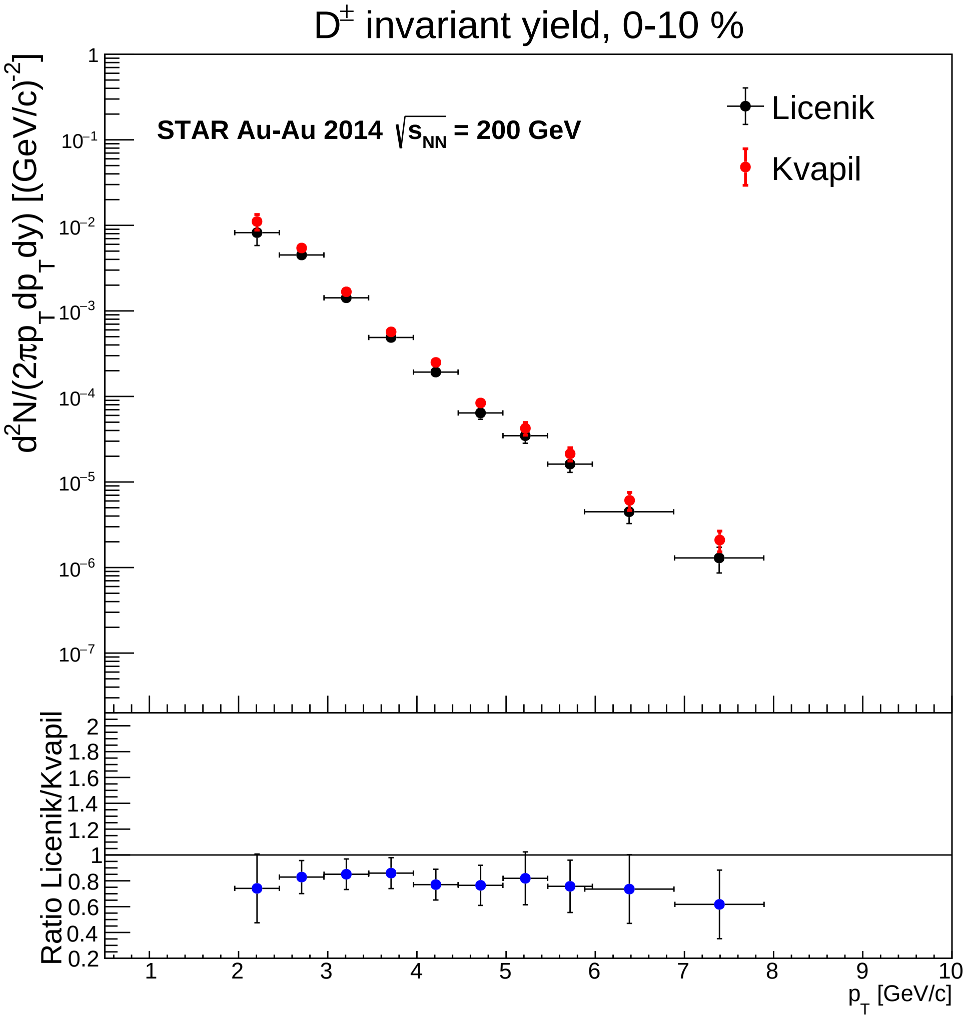

Figure 4.18: The $D^{\pm}$ p_T spectrum (invariant yield) obtained in this thesis (black points) and compared with results from [3] (red points), along with the ratio of these two results (blue points) for centrality bin 0-10 %. The vertical errorbars contain both systematic and statistical errors while the horizontal errorbars show correctly only the width of the corresponding p_T bin, not the actual endpoints of the bin.

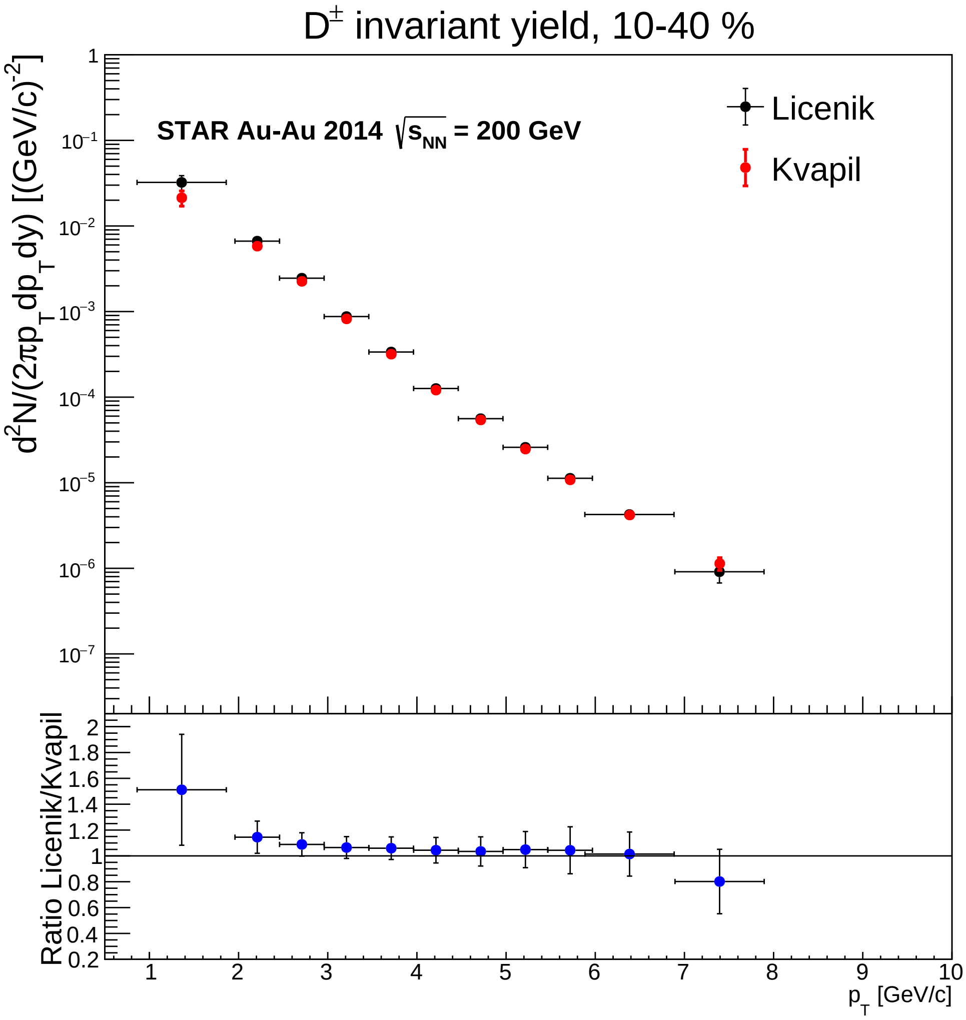

Figure 4.19: The $D^{\pm}$ p_T spectrum (invariant yield) obtained in this thesis (black points) and compared with results from [3] (red points), along with the ratio of these two results (blue points) for centrality bin 10-40 %. The vertical errorbars contain both systematic and statistical errors while the horizontal errorbars show correctly only the width of the corresponding p_T bin, not the actual endpoints of the bin.

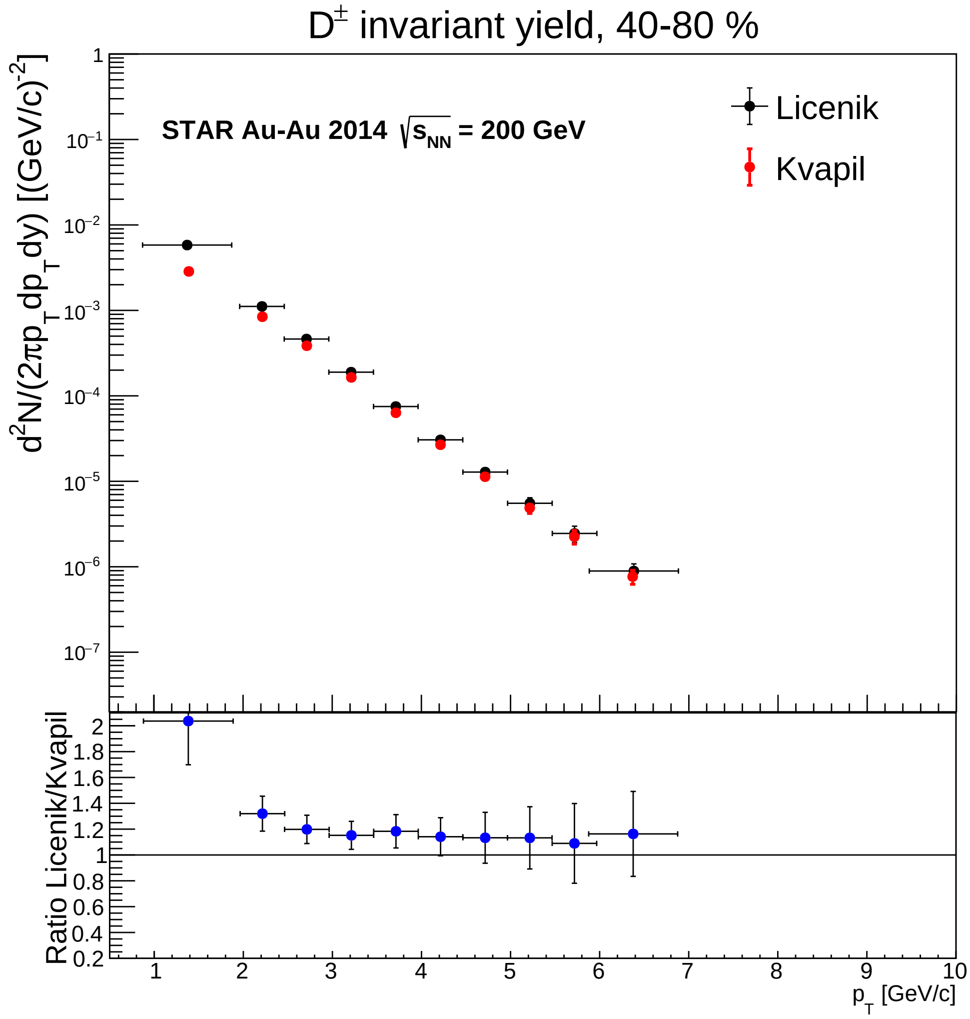

Figure 4.20: The $D^{\pm}$ p_T spectrum (invariant yield) obtained in this thesis (black points) and compared with results from [3] (red points), along with the ratio of these two results (blue points) for centrality bin 40-80 %. The vertical errorbars contain both systematic and statistical errors while the horizontal errorbars show correctly only the width of the corresponding p_T bin, not the actual endpoints of the bin.

Summary & Outlook

The purpose of this work was to study the production of the charmed mesons - especially the $D^{\pm}$ meson - in heavy ion collisions. Charmed particles are formed exclusively during the earliest part of the collision and therefore serve as an excellent probe in the strongly interacting medium - QGP - created during the next stage of the collision evolution, because they experience the entire evolution of the system. The results from the STAR and ALICE collaborations show significant suppression of the $D^{\pm}$ meson production in central nucleus-nucleus collisions at higher p_T. The analysis started in this thesis has been conducted on the 2014 Au-Au data at $\sqrt{s_{NN}} = 200$ GeV collected by the STAR experiment. This analysis followed the work started by J. Kvapil in 2016 with the main goal to improve the significance of the extracted signal and to improve some of the analysis techniques, including the calculations of the systematic errors. The $D^{\pm}$ raw yield was successfully extracted from the data by subtracting the wrong-sign combinations from the correct-sign combinations of $K\pi\pi$ triplets within the $1.0 < p_T < 10$ GeV/c range. By applying several correction techniques, it was possible to reconstruct the $D^{\pm}$ invariant yield p_T spectrum and compare to results from [3]. The results show good agreement overall, with differences caused by using slightly different data subset and cuts, different approach towards p_T points correction and different results from the $Eff(p_T)$ simulation fit. At this point, there is still a room for improvement of the signal significance (the planned use of TMVA for cut optimization should help significantly), while the p_T spectrum correction and the detector acceptance$\times$efficiency calculation was improved. The thorough study and calculation of the systematic errors remains work in progress at this point.

References

[1] C. Patrignani et al. (Particle Data Group), Chin. Phys. C, 40, 100001 (2016) and 2017 update

[2] J. Kvapil, "$D^{\pm}$ meson production in Au+Au collisions at $\sqrt{s_{NN}} = 200$ GeV measured by the STAR experiment", Quark Matter 2017, Chicago, 2/5-11/2017

[3] J. Kvapil, "Charged charm mesons in Au+Au collisions", Master's Thesis, Czech Technical University in Prague, 2016

[4] A. Toia, "Participants and spectators at the heavy-ion fireball", University of Padua/INFN, CERN Courier, 4/26/2013, [online, cit. 2/25/16], `http://cerncourier.com/cws/article/cern/53089`

[5] "More Details on the ALICE V0 Detector", CERN, [online, cit. 3/11/16], `http://alipub-dev.web.cern.ch/detectors/more-details-alice-v0-detector`

[6] M. Miller *et al.*, "Glauber Modeling in High Energy Nuclear Collisions", arXiv:nucl-ex/0701025

[7] R. Russo "Measurement of D^+ meson production in p-Pb collisions with the ALICE detector", PhD Thesis, University of Turin, 2015, arXiv:1511.04380 [nucl-ex]

[8] T.K. Nayak, "Heavy Ions: Results from the Large Hadron Collider", arXiv:1201.4264 [nucl-ex]

[9] J. Adams *et al.*, "Experimental and Theoretical Challenges in the Search for the Quark Gluon Plasma: The STAR Collaboration's Critical Assessment of the Evidence from RHIC Collisions ", STAR Collaboration, arXiv:nucl-ex/0501009

[10] BRAHMS Collaboration, Nucl. Phys. A Vol. 757, Issues 1-2 , 8 August 2005, 1-27

[11] PHOBOS Collaboration, Nucl. Phys. A Vol. 757, Issues 1-2 , 8 August 2005, 28-101

[12] PHENIX Collaboration, Nucl. Phys. A Vol. 757, Issues 1-2 , 8 August 2005, 184-283

[13] M. Gyulassy, "The QGP Discovered at RHIC", arXiv:nucl-th/0403032v1

[14] M. Peskin *et al.*, "An Introduction to Quantum Field Theory", 1995, p. 552

[15] T. Dorigo "New CMS Results", 10/27/2014, [online, cit. 3/8/16], `http://www.science20.com/a_quantum_diaries_survivor/new_cms_results-147752`

[16] Z. Fodor, S.D. Katz, "The Phase Diagram of Quantum Chromodynamics", arXiv:0908.3341v1 [hep-ph]

[17] U. Heinz, M. Jacob, "Evidence for a New State of Matter: An Assessment of the Results from the CERN Lead Beam Programme", arXiv:nucl-th/0002042v1

[18] R.J. Reed, "Υ production at $\sqrt{s_{NN}} = 200$ GeV in p+p and Au+Au collisions at STAR", PhD Thesis, UC Davis, 2011

[19] D. d'Enterria, B. Betz, "High-p_T Hadron Suppression and Jet Quenching", Lect. Notes Phys. 785, 285–339 (2010), DOI 10.1007/978-3-642-02286-9 9

[20] M. J. Tannenbaum, "How do quarks and gluons lose energy in the QGP?", arXiv:1404.6232v1 [nucl-ex]

[21] B. Z. Kopeilovich *et al.*, "Cronin Effect in Hadron Production off Nuclei", arXiv:hep-ph/0201010v2

[22] E. M. Levin *et al.*, "Baryon Anomaly in Heavy-Ion Collisions and Colour Correlations in QGP", Nucl. Phys. A, Vol. 904–905, 2013, ISSN 0375-9474

[23] D. d'Enterria, "Jet Quenching", CERN, arXiv:0902.2011v2 [nucl-ex]

[24] T. Matsui, H. Satz, "J/ψ Suppression by Quark-gluon Plasma Formation", Phys. Let. B, vol. 178, no. 4, 10/9/1986

[25] B. Trzeciak, "J/ψ measurements in the STAR experiment", STAR collaboration, arXiv:1412.7345v1 [hep-ex]

[26] A. Andronic *et al.*, "Heavy-flavour and Quarkonium Production in the LHC Era: From Proton-proton to Heavy-ion Collisions", arXiv:1506.03981v1 [nucl-ex]

[27] A. Saini, S. Bhardwaj, "Elliptic Flow in Heavy Ion Collisions", 2014, JNPP, DOI: 10.5923/j.jnpp.20140406.02

[28] B.I. Abelev *et al.*, "Mass, Quark-number, and $\sqrt{s_{NN}}$ Dependence of the Second and Fourth Flow Harmonics in Ultra-relativistic Nucleus-nucleus Collisions", arXiv:nucl-ex/0701010

[29] "Higher harmonic flow coefficients of identified hadrons in Pb-Pb collisions at $\sqrt{s_{NN}} = 2.76$ TeV", the ALICE collaboration, arXiv:1606.06057v2 [nucl-ex]

[30] "Measurement of D^0 azimuthal anisotropy at mid-rapidity in Au+Au collisions at $\sqrt{s_{NN}} = 200$ GeV", STAR Collaboration, arXiv:1701.06060v3

[31] "Reaching for the Horizon - The 2015 Long Range Plan for Nuclear Science", The 2015 Nuclear Science Advisory Committee, US Department of Energy, 10/20/2015 `https://science.energy.gov/np/nsac/`

[32] R.A. Lacey *et al.*, "Has the QCD Critical Point Been Signaled by Observations at RHIC?", arXiv:nucl-ex/0609025v5

[33] R.A. Lacey, "Indications for a critical end point in the phase diagram for hot and dense nuclear matter", Quark Matter 2015, Kobe, 9/28/2015

[34] L. Kumar, "STAR Results from the RHIC Beam Energy Scan-I", STAR collaboration, arXiv:1211.1350v1 [nucl-ex]

[35] "Measurement of D-meson production at mid-rapidity in pp collisions at $\sqrt{s} = 7$ TeV", ALICE collaboration, arXiv:1702.00766v1 [hep-ex]

[36] "Transverse momentum dependence of D-meson production in Pb–Pb collisions at $\sqrt{s_{NN}} = 2.76$ TeV", ALICE collaboration, arXiv:1509.06888v2 [nucl-ex]

[37] "Measurement of $D^{*\pm}$, $D^{\pm}$ and $D^{\pm s}$ meson production cross sections in pp collisions at $\sqrt{s} = 7$ TeV with the ATLAS detector", arXiv:1512.02913v2 [hep-ex]

[38] "Measurements of prompt charm production cross-sections in *pp* collisions at $\sqrt{s} =$ 13 TeV", LHCb collaboration, arXiv:1510.01707v6 [hep-ex]

[39] G. Robert-Demolaize *et al.*, "RHIC Performance for FY2014 Heavy Ion Run", Proceedings of IPAC2014, Dresden, Germany

[40] "RHIC - Brookhaven National Laboratory", [online, cit. 12/29/17], `https://www.bnl.gov/rhic/`

[41] H. Hahn *et al.*, "The RHIC design overview", Nucl. Instrum. Meth., vol. A499, pp. 245–263, 2003

[42] K. Walsh, "Accelerating Particles Accelerates Science — With Big Benefits for Society", 3/13/2013, [online cit. 4/16/16], `https://www.bnl.gov/rhic/news2/news.asp?a=3758&t=today` Quark Matter 2015, Kobe, 9/26/2015

[43] A. Accardi *et al.*, "Electron Ion Collider: The Next QCD Frontier", arXiv:1212.1701v3 [nucl-ex]

[44] "The STAR Experiment", [online, cit. 4/19/16], `https://drupal.star.bnl.gov/STAR`

[45] M. Anderson *et al.*, "The STAR Time Projection Chamber: A Unique Tool for Studying High Multiplicity Events at RHIC", Nucl. Instrum. Meth., vol. A499, pp. 659–678, 2003

[46] K. Kajimoto, "A large area time of flight detector for the STAR experiment at RHIC", PhD Thesis, University of Texas at Austin, 2009, `http://hdl.handle.net/2152/7860`

[47] M. Beddo *et al.*, "The STAR Barrel Electromagnetic Calorimeter", Nucl. Instrum. Meth., vol. A499, pp. 725-739, 2003

[48] W.J. Llope *et al.*, "The STAR Vertex Position Detector", arXiv:1403.6855 [physics.ins-det]

[49] L. Yarris, "Heavy Flavor Tracker for STAR", 2/18/2014, [online, cit. 5/10/16], `http://newscenter.lbl.gov/2014/02/18/heavy-flavor-tracker-for-star/`

[50] J. Schambach *et al.*, "The STAR Heavy Flavor Tracker (HFT)", 9/2014, 10.3204/DESY-PROC-2014-04/83, C14-08-24, p.659-664

[51] T.C. Huang *et al.*, "Muon Identification with Muon Telescope Detector at the STAR Experiment", arXiv:1601.02910v3 [physics.ins-det]

[52] M. Lisa *et al.*, "An Event Plane Detector for STAR", [online, cit. 1/9/18] `https://drupal.star.bnl.gov/STAR/system/files/Construction_Proposal_0.pdf`

[53] O.D. Tsai *et al.*, 2015, J. Phys.: Conf. Ser. 587 012053

[54] B.I. Abelev *et al.*, "Hadronic resonance production in d+Au collisions at $\sqrt{s_{NN}} =$ 200 GeV at RHIC", arXiv:0801.0450v2 [nucl-ex]

Appendices

Appendix A

Invariant Mass Distributions

The invariant mass distributions for $K\pi\pi$ triplets in 4 centrality and 12 transverse momentum bins are shown in figures A.1 - A.12. These distributions were obtained during the process of raw yield extraction described in sec. 4.3. The correct-sign distributions are fitted with a sum of a Gaussian and a first order polynomial function. The wrong-sign combinations are shown already scaled with the correct-sign-to-background ratio. The signal distributions are fitted with a Gaussian function and contain information about calculated raw yield and the peak significance. Peaks with significance lower than 3 were considered insignificant. The peaks are clearly visible in vast majority of the bins, showing high precision of the reconstruction.

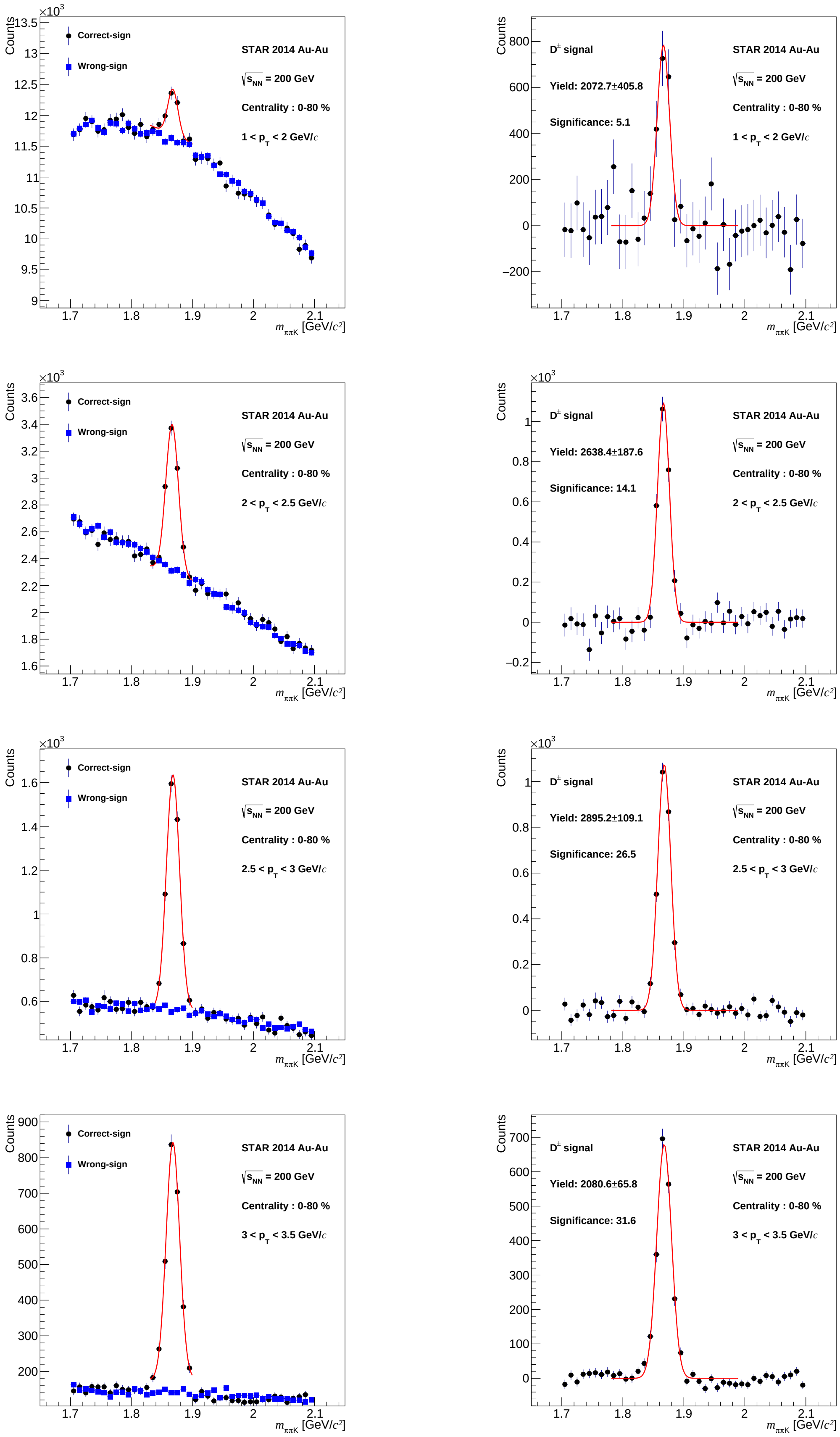

Figure A.1: Invariant mass distribution of $K\pi\pi$ triplets before (left panel) and after (right panel) background subtraction for the 0-80 % centrality range and p_T bins: 1-2, 2-2.5, 2.5-3 and 3-3.5 GeV$/c$.

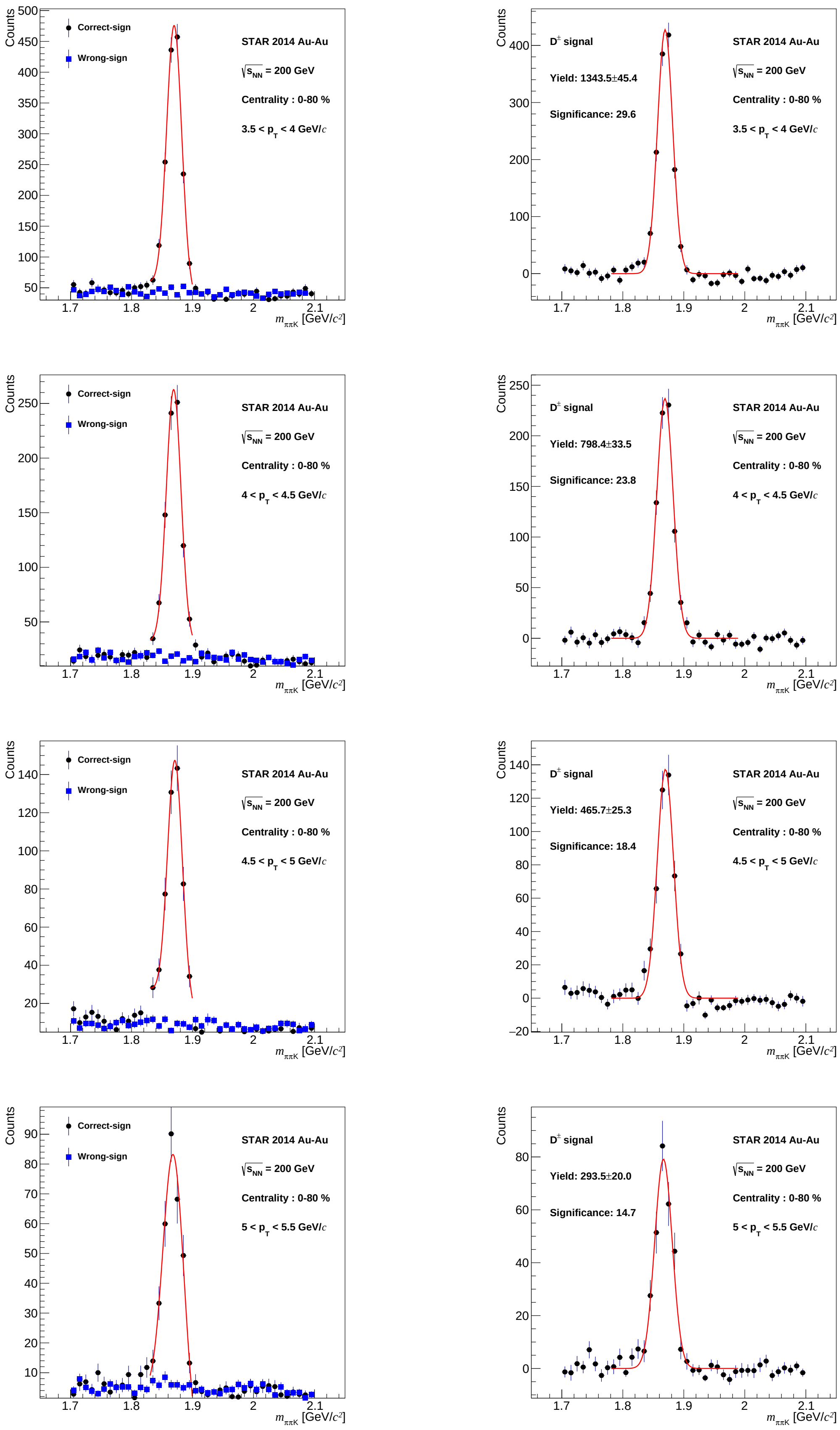

Figure A.2: Invariant mass distribution of $K\pi\pi$ triplets before (left panel) and after (right panel) background subtraction for the 0-80 % centrality range and p_T bins: 3.5-4, 4-4.5, 4.5-5 and 5-5.5 GeV/c.

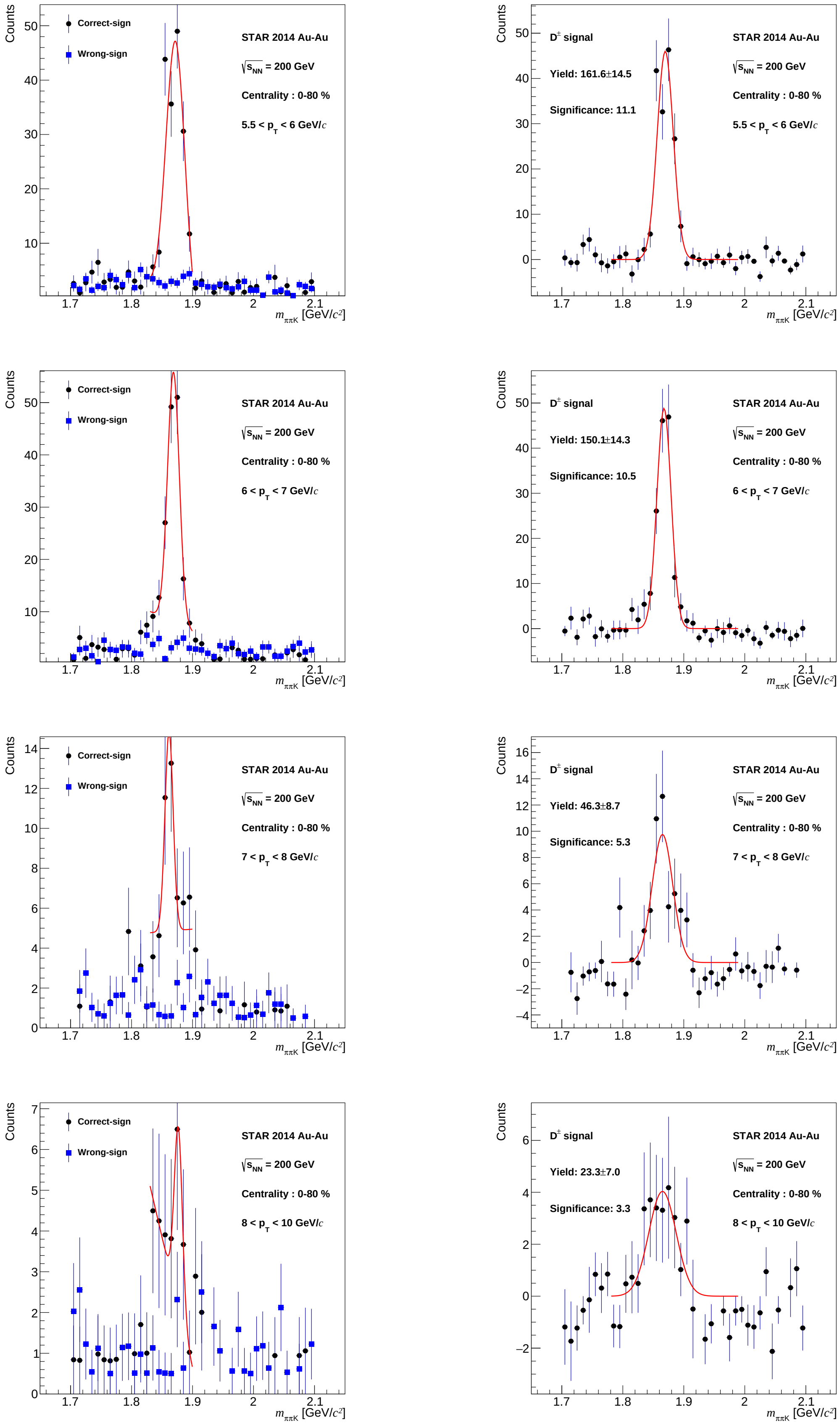

Figure A.3: Invariant mass distribution of $K\pi\pi$ triplets before (left panel) and after (right panel) background subtraction for the 0-80 % centrality range and p_T bins: 5.5-6, 6-7, 7-8 and 8-10 GeV/c.

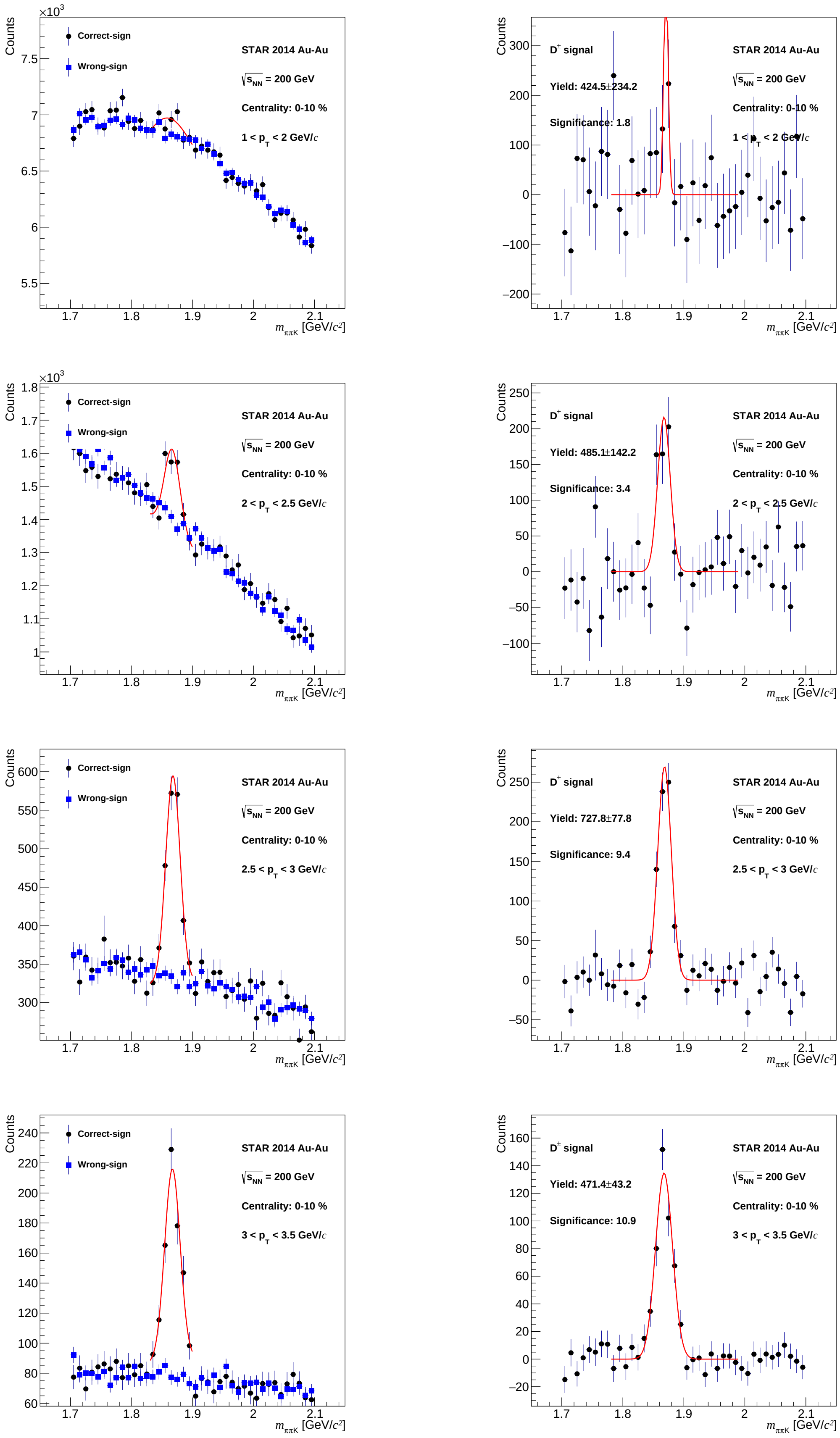

Figure A.4: Invariant mass distribution of $K\pi\pi$ triplets before (left panel) and after (right panel) background subtraction for the 0-10 % centrality range and p_T bins: 1-2, 2-2.5, 2.5-3 and 3-3.5 GeV/c.

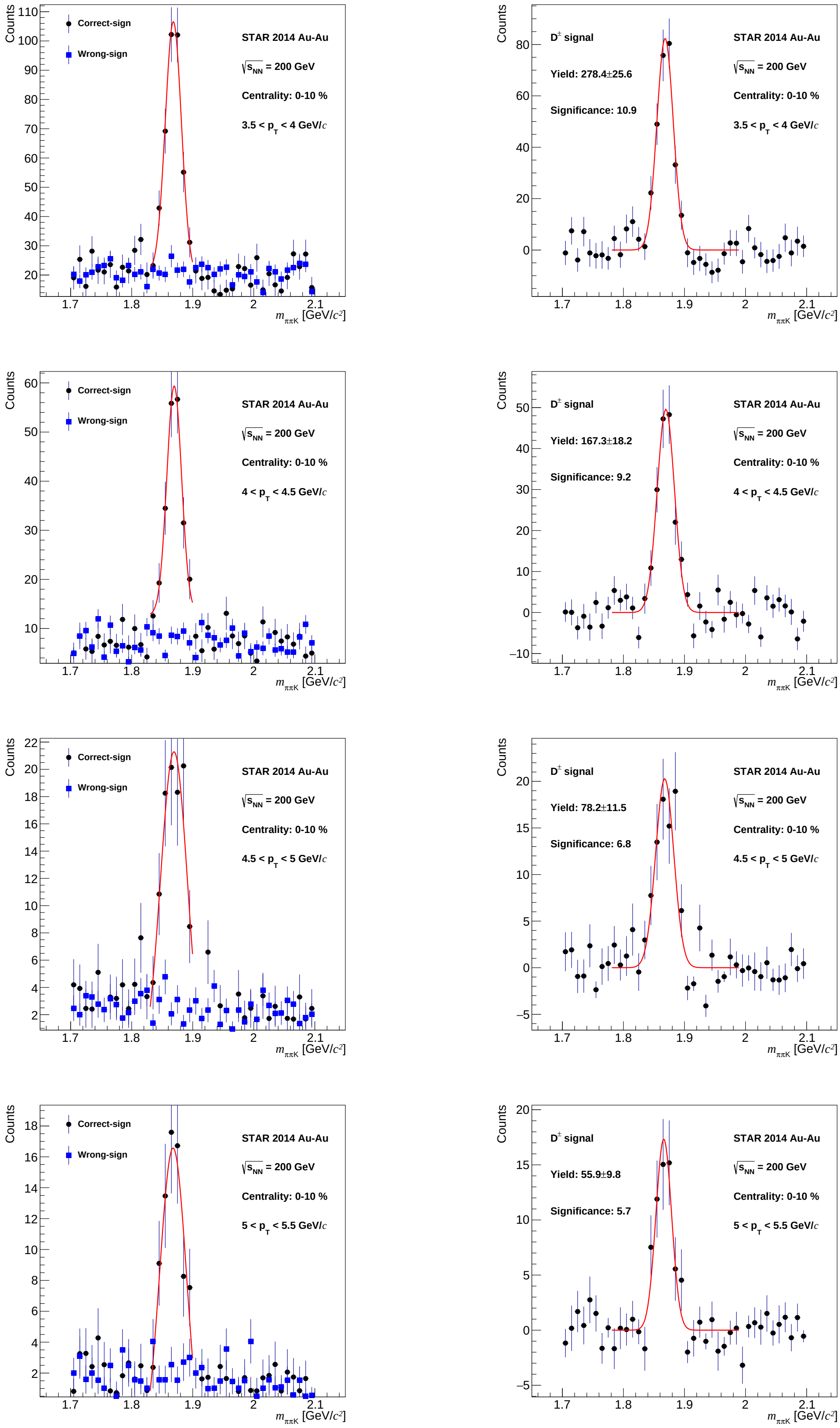

Figure A.5: Invariant mass distribution of $K\pi\pi$ triplets before (left panel) and after (right panel) background subtraction for the 0-10 % centrality range and p_T bins: 3.5-4, 4-4.5, 4.5-5 and 5-5.5 GeV/c.

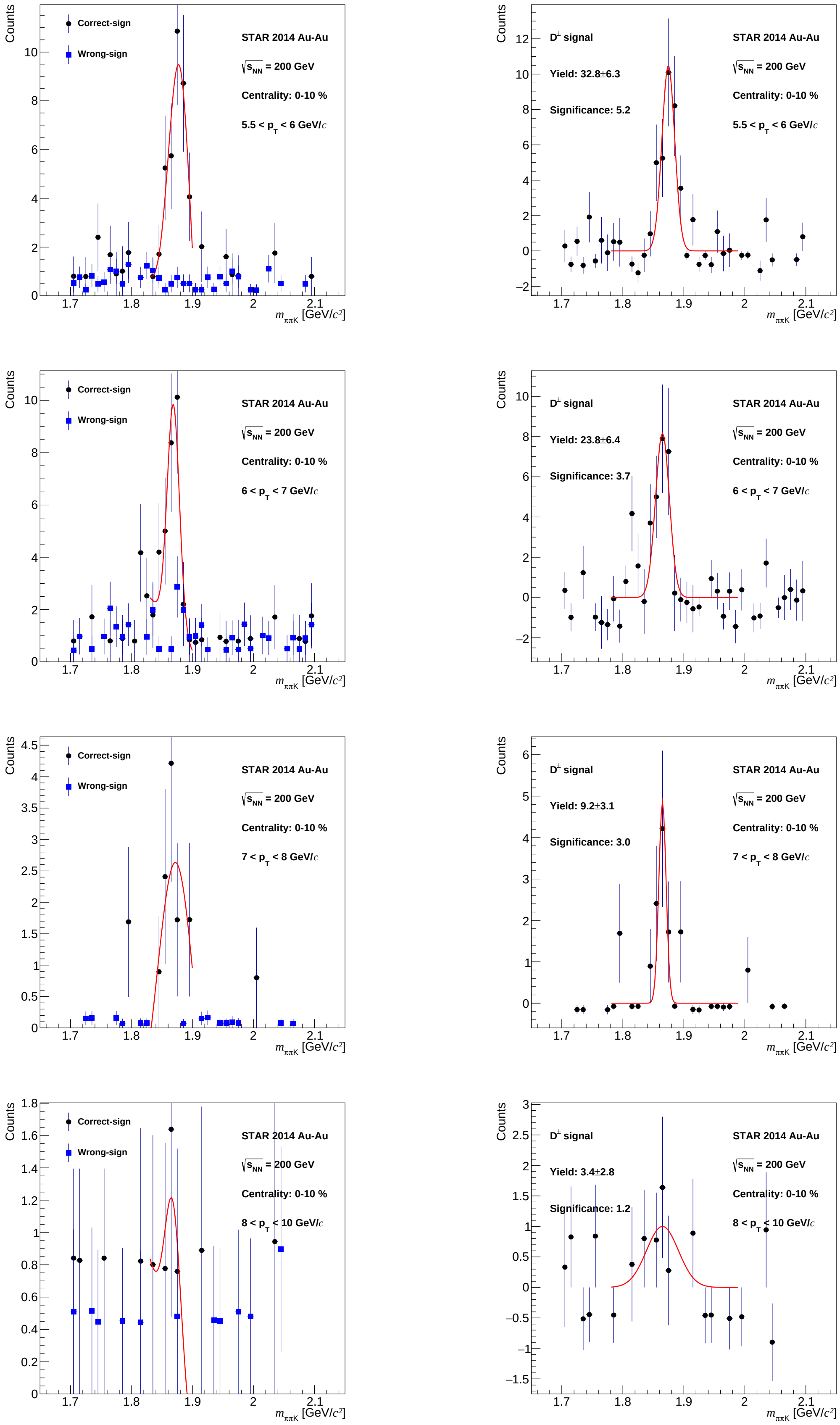

Figure A.6: Invariant mass distribution of $K\pi\pi$ triplets before (left panel) and after (right panel) background subtraction for the 0-10 % centrality range and p_T bins: 5.5-6, 6-7, 7-8 and 8-10 GeV/c.

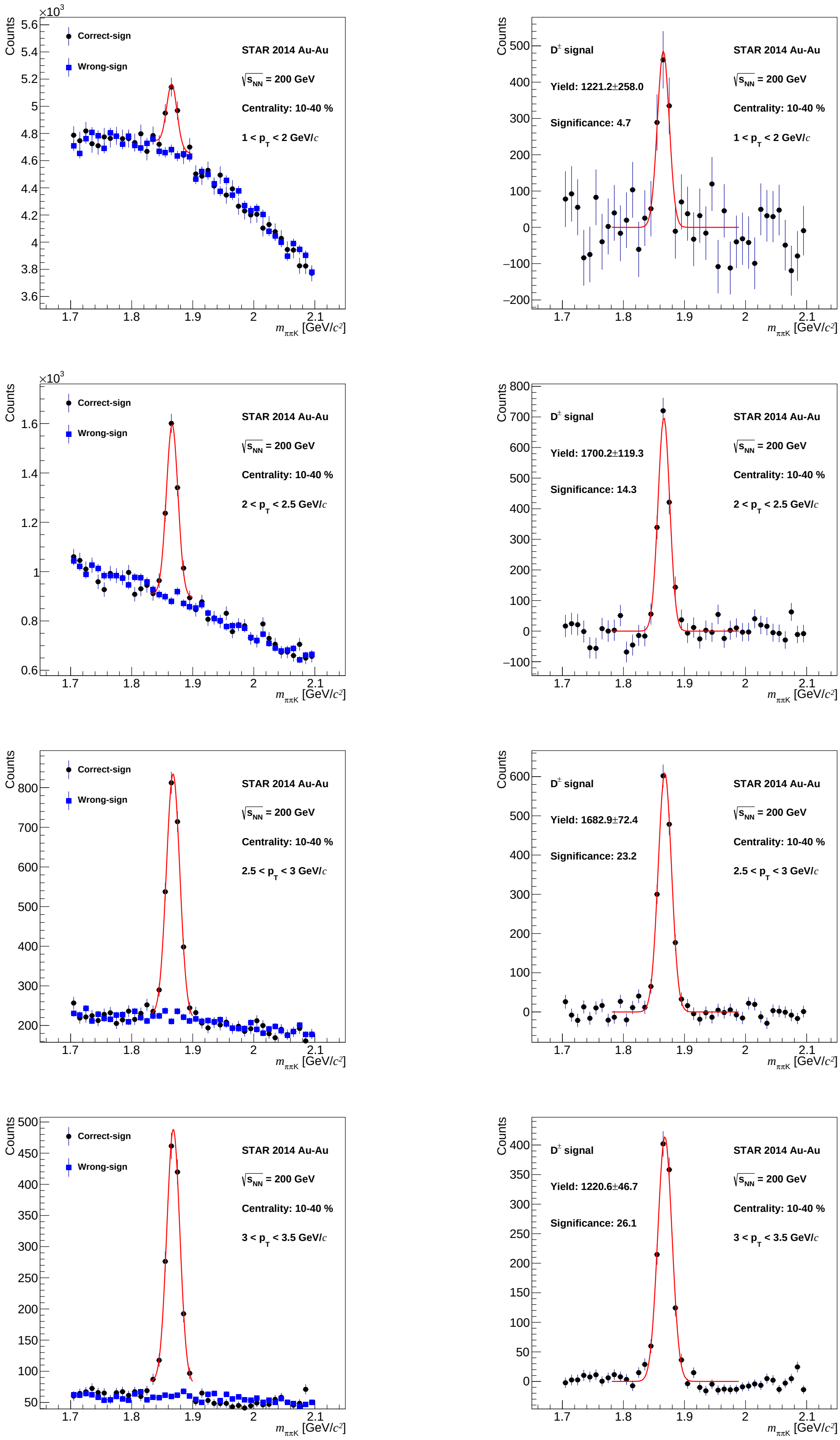

Figure A.7: Invariant mass distribution of $K\pi\pi$ triplets before (left panel) and after (right panel) background subtraction for the 10-40 % centrality range and p_T bins: 1-2, 2-2.5, 2.5-3 and 3-3.5 GeV/c.

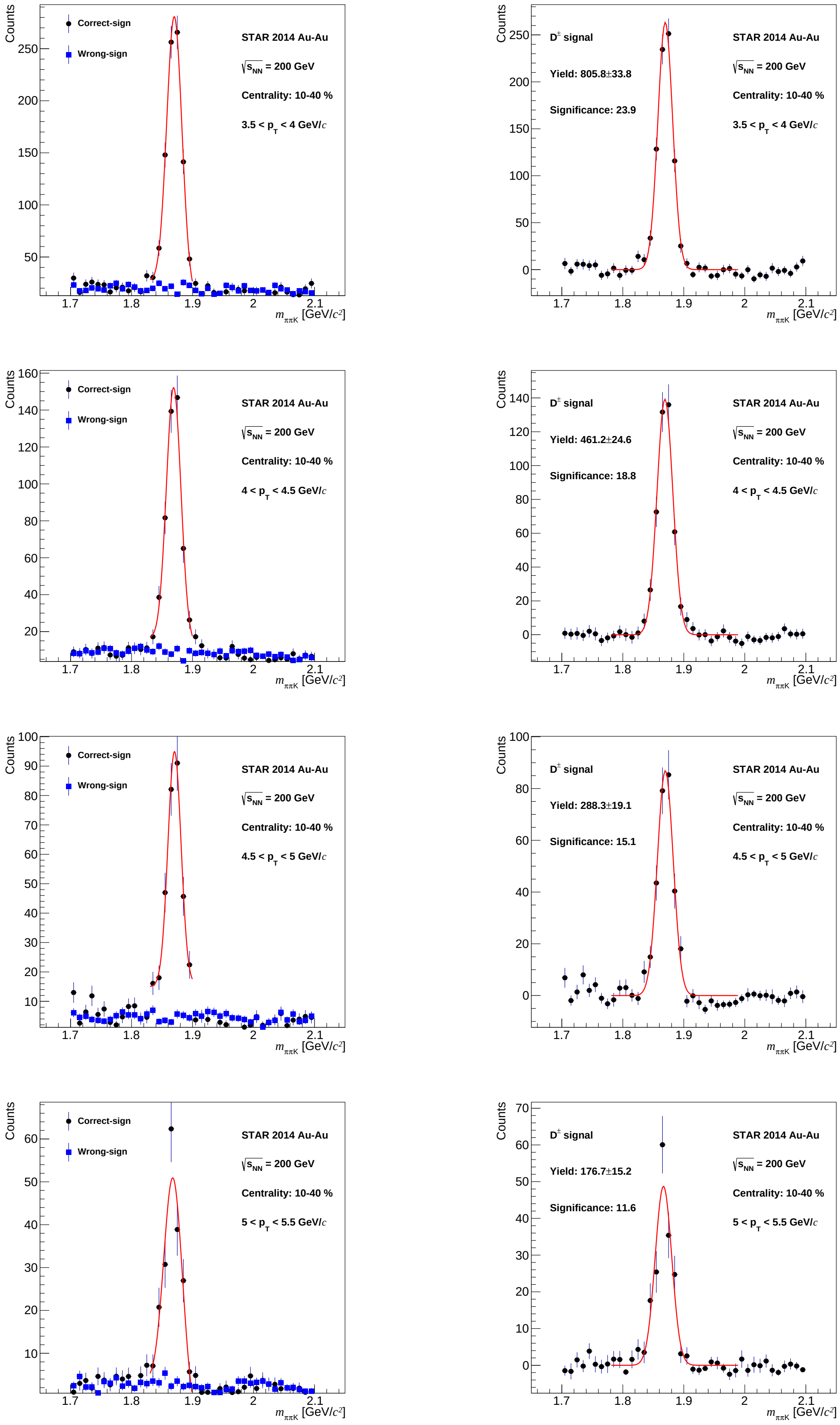

Figure A.8: Invariant mass distribution of $K\pi\pi$ triplets before (left panel) and after (right panel) background subtraction for the 10-40 % centrality range and p_T bins: 3.5-4, 4-4.5, 4.5-5 and 5-5.5 GeV/c.

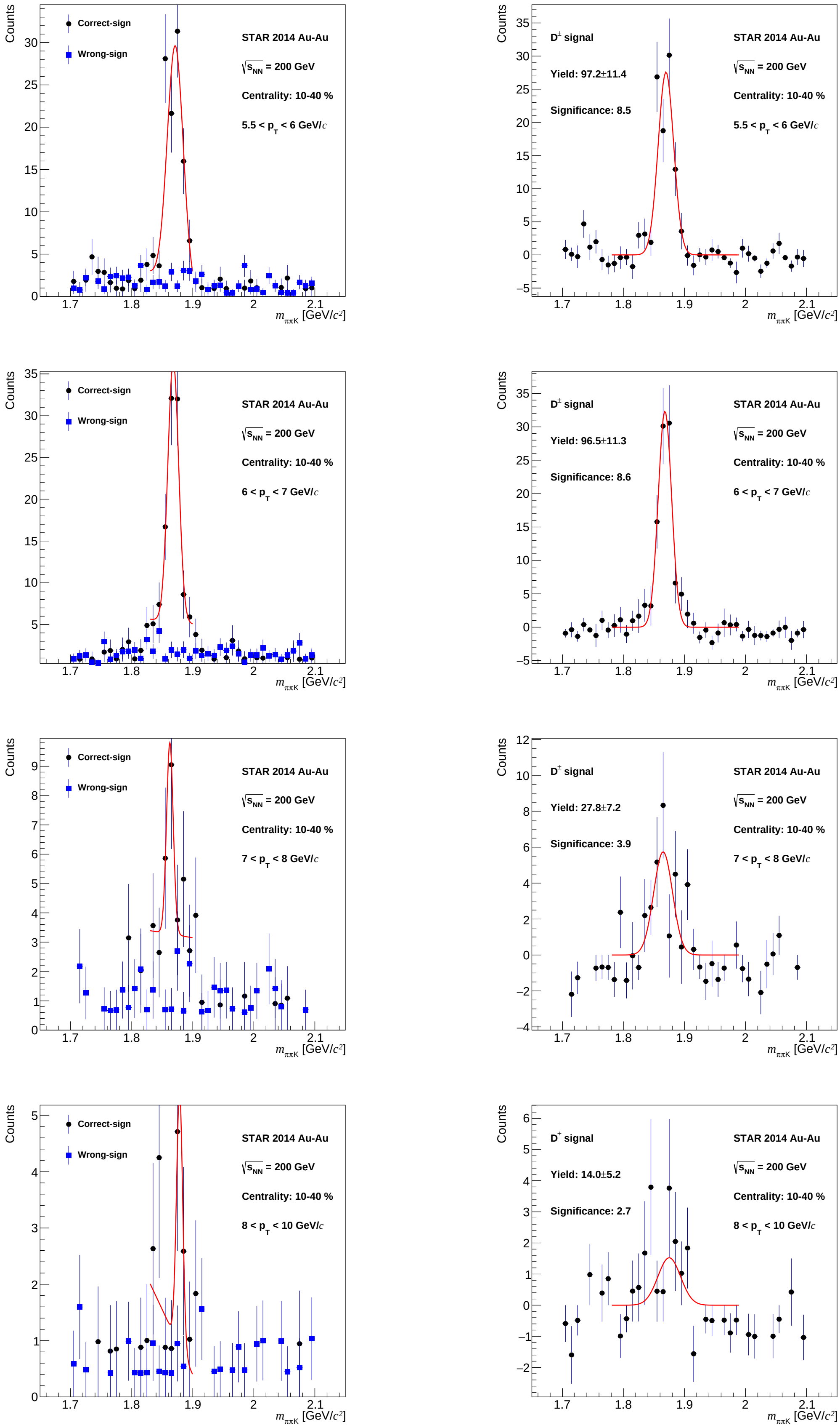

Figure A.9: Invariant mass distribution of $K\pi\pi$ triplets before (left panel) and after (right panel) background subtraction for the 10-40 % centrality range and p_T bins: 5.5-6, 6-7, 7-8 and 8-10 GeV/c.

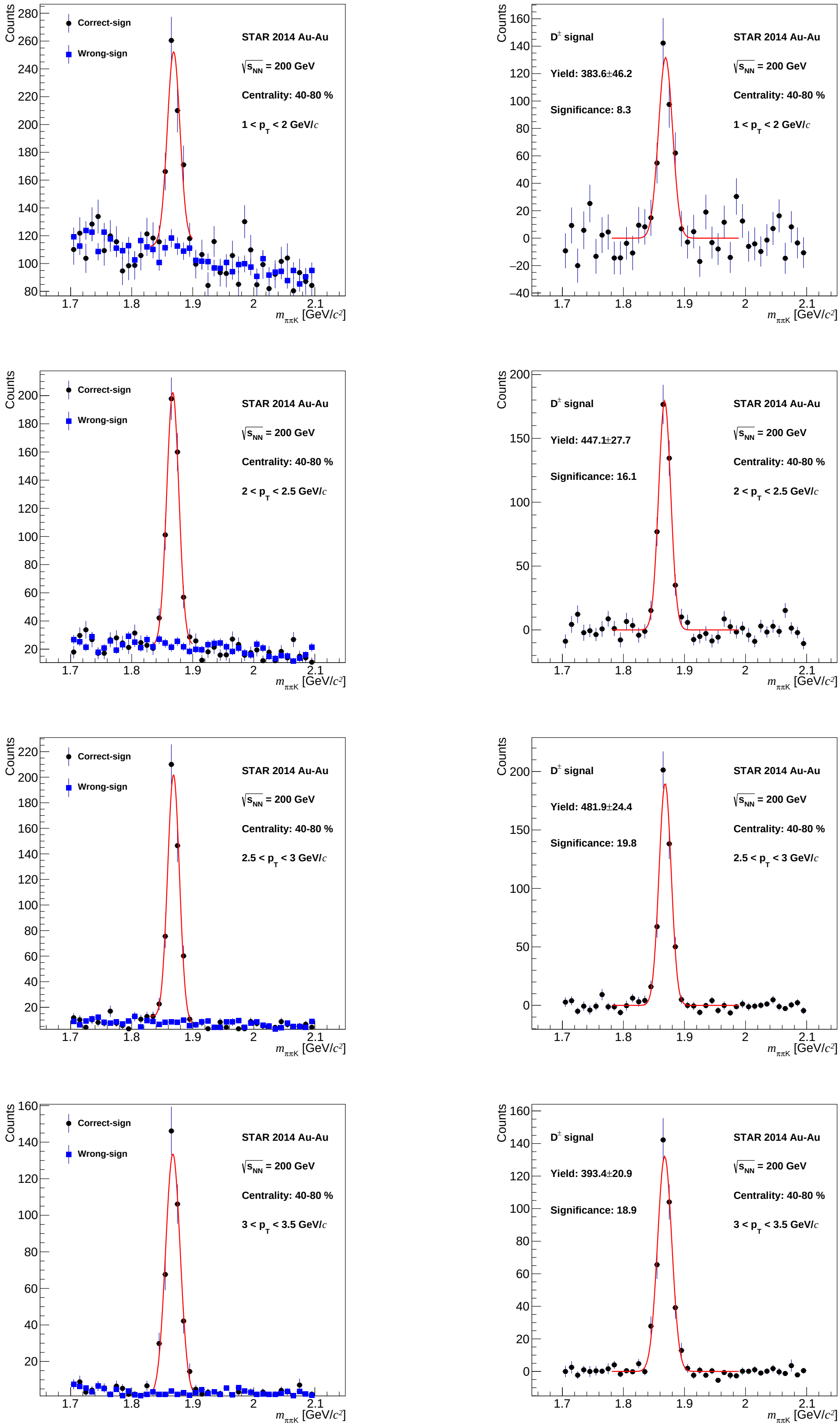

Figure A.10: Invariant mass distribution of $K\pi\pi$ triplets before (left panel) and after (right panel) background subtraction for the 40-80 % centrality range and p_T bins: 1-2, 2-2.5, 2.5-3 and 3-3.5 GeV$/c$.

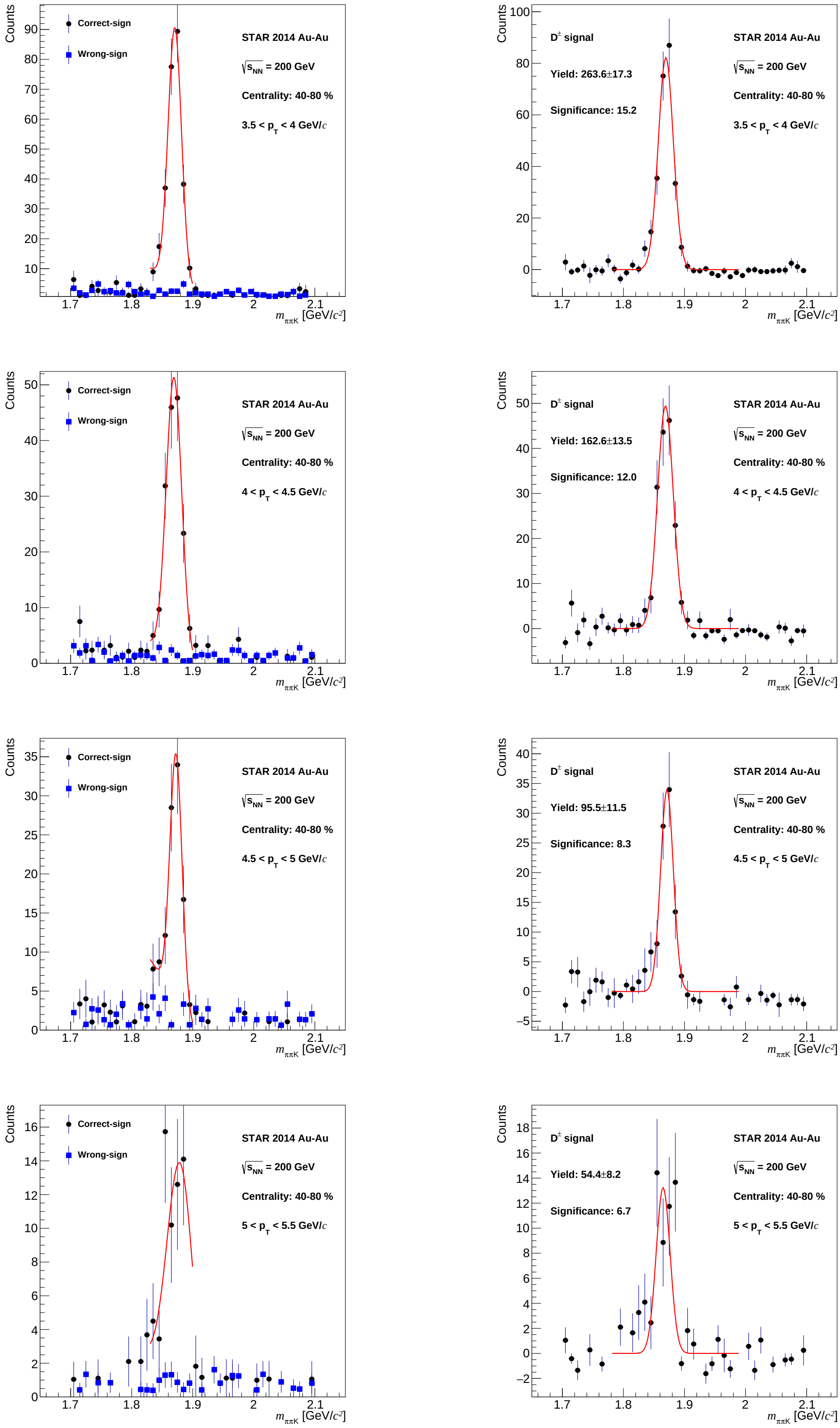

Figure A.11: Invariant mass distribution of $K\pi\pi$ triplets before (left panel) and after (right panel) background subtraction for the 40-80 % centrality range and p_T bins: 3.5-4, 4-4.5, 4.5-5 and 5-5.5 GeV$/c$.

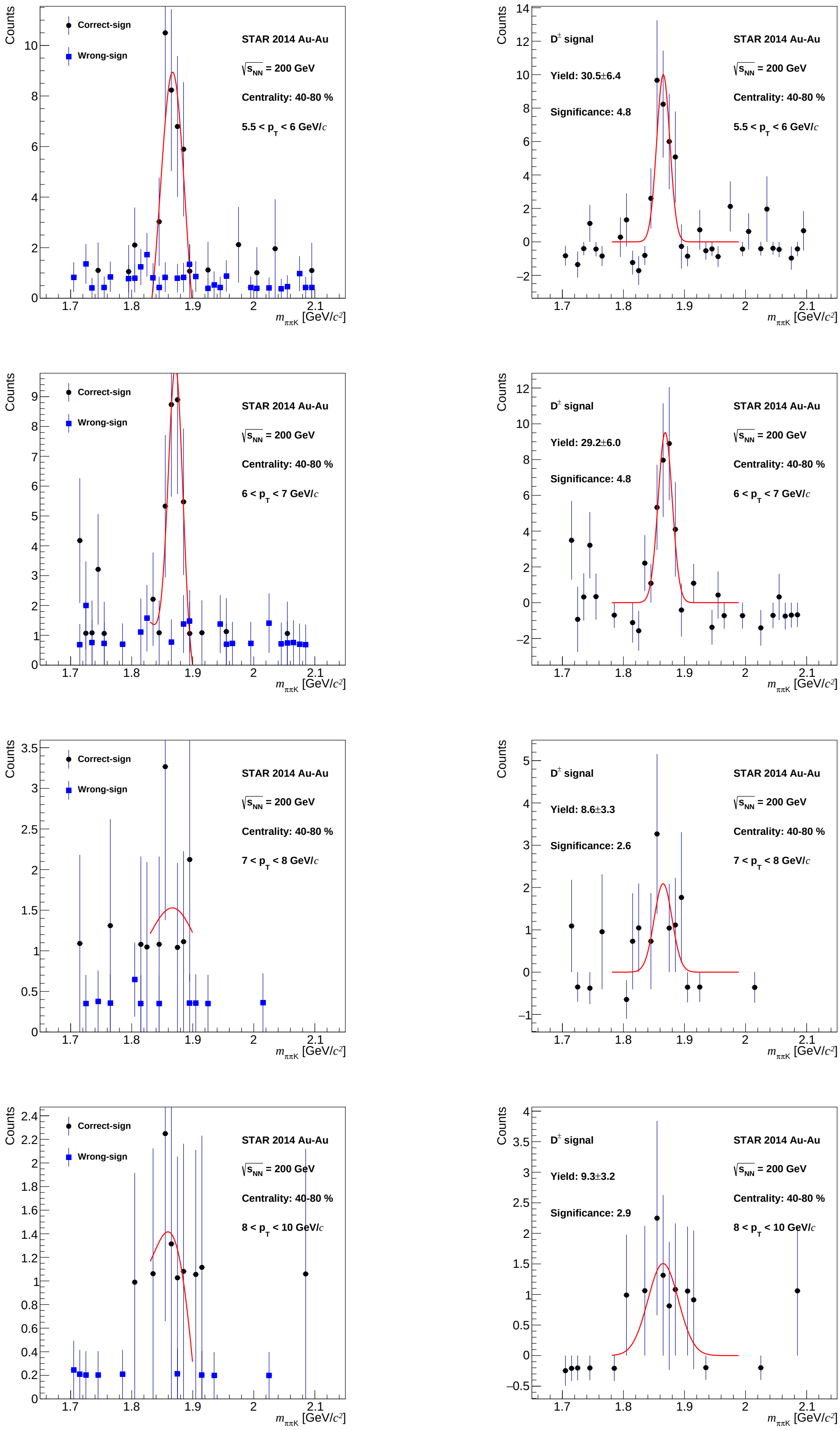

Figure A.12: Invariant mass distribution of $K\pi\pi$ triplets before (left panel) and after (right panel) background subtraction for the 40-80 % centrality range and p_T bins: 5.5-6, 6-7, 7-8 and 8-10 GeV/c.